

CR-172037

THE UNIVERSITY OF TEXAS AT AUSTIN

CONVECTIVE HEATING IN AND
AROUND GAPS IN LAMINAR AND
TRANSITIONAL BOUNDARY LAYERS

John J. Bertin

P. Jan Burley

Timothy E. Hayden



Aerospace Engineering Report 79004

This work was supported by
the Johnson Space Center (NASA)
through Contract NAS 9-13680

November 1979

Department of Aerospace Engineering and Engineering Mechanics

(NASA-CR-172037) CONVECTIVE HEATING IN AND
AROUND GAPS IN LAMINAR AND TRANSITIONAL
BOUNDARY LAYERS (Texas Univ.) 125 p

N88-70106

Unclas
00/34 0082559

CONVECTIVE HEATING IN AND AROUND GAPS IN LAMINAR
AND TRANSITIONAL BOUNDARY LAYERS*

by

John J. Bertin, P. Jan Burley, and Timothy E. Hayden

Aerospace Engineering Report 79004

*This work was supported by the Johnson Space Center (NASA) through
Contract NAS 9-13680

Department of Aerospace Engineering
and Engineering Mechanics

The University of Texas at Austin

November 1979

ACKNOWLEDGEMENTS

This research was supported by the Johnson Space Center (NASA) through contract NAS 9-13680. The authors acknowledge the considerable efforts of Dr. W.D. Goodrich in providing technical assistance and guidance to the effort. The authors would also like to thank Ms. Bettye Lofton for cheerfully typing the numerous drafts of the manuscript.

TABLE OF CONTENTS

Page

INTRODUCTION	
NOMENCLATURE	
DISCUSSION OF RESULTS	1
Data for Configuration 1(C1)	1
Test condition variations	2
Flow model variations	3
Transition	4
Data for Configuration 2(C2)	7
Open cavity/closed cavity	8
Basic heat-transfer distributions	9
Correlations	16
Data for Configuration 3(C3)	19
Data for Configuration 4(C4)	21
Basic heat-transfer measurements along the length of the longitudinal slot	23
Basic heat-transfer measurements downstream of the T gap	24
The Modified C4 Configuration	31
Data for Configuration 5(C5)	33
CONCLUDING REMARKS	37
REFERENCES	39
TABLES	
FIGURES	

INTRODUCTION

The presence of gas, slots, and/or steps in the surface may significantly perturb a supersonic boundary layer. The perturbations may increase the boundary-layer thickness with a reduction in the overall heating, may cause viscous shock interactions with locally high heating rates affecting only a small fraction of the surface, or may increase the turbulence resulting in premature transition and affecting the heating rates over large surface areas. The qualitative and the quantitative effects on the flow field due to these sudden changes in the surface slope depend on its geometry, on its dimensions relative to the boundary layer thickness, and on the characteristics of the boundary layer.

NOMENCLATURE

d	depth of the gap or height of the recompression surface
L	total length of the flat plate
M_e	Mach number at the edge of the boundary layer
\dot{q}	local heat-transfer rate
\dot{q}_{fp}	local heat-transfer rate at the same station, averaged for the three y-stations (used as denominator in heating-rate ratios)
$\dot{q}_{fp,1}$	local heat-transfer rate at the same x-station and y-coordinate (used as denominator in heating-rate ratios)
\dot{q}_{pk}	peak heating rate in the vicinity of a gap or slot
$\dot{q}_{pk,i}$	peak heating rate measured on the impingement surface of a gap
\dot{q}_{utp}	heating rate measured at the upper tangency point
Re_x	local Reynolds number based on the streamwise distance from the leading edge of the plate
Re_θ	Reynolds number based on the local momentum thickness
$Re_{\infty,L}$	free-stream Reynolds number based on the total length of the plate
T_t	stagnation (or total) temperature
w	width of the gap
x	distance from the leading edge of the plate (see Fig. 2)
x_s	x-distance to the transverse gap (configurations C2 and C4)
x_0	x-distance to the beginning of the longitudinal slot (configuration C4)
y	distance from the plane of symmetry (see Fig. 2)

- z^* z-coordinate of the sonic point
- z magnitude of distance from the horizontal surface of the flat-plate holder (negative values are not used in this report)
- δ^* displacement thickness
- ϕ ratio of the theoretical heating rate for turbulent flow divided by the theoretical heating rate for the actual flow conditions over a smooth surface.

Subscript

- tr evaluated at the transition point

DISCUSSION OF RESULTS

Heat-transfer distributions were measured for five different configurations. The various configurations represent different gap geometries which were obtained by placing instrumented inserts into the structural carrier-plate that is shown in Fig. 1. The carrier plate is a 2-inch thick, 27-inch wide, 60-inch long flat, stainless-steel plate with a sharp, 5° leading edge. The heat-transfer data were obtained in the 3.5-Foot Hypersonic Wind Tunnel at the Ames Research Center (NASA). The free-stream Mach number was 5.10 and the angle of attack was zero for the entire run schedule. The variables of the test program included the free-stream Reynolds number and the gap configuration (e.g., width, depth, step height, number and orientation). For additional information about the test program, the reader is referred to ref. 1.

Data for Configuration 1(C1)

A smooth, flat-plate, heat-transfer insert was placed in the structural carrier-plate to form Configuration 1(C1). As shown in Fig. 2, there were three rows of thermocouples that provided heat-transfer data for axial locations in the range 35.52 cm (13.98 in) $\leq x \leq$ 129.59 cm (51.02 in) along the centerline of the plate ($y = 0.0$) and ± 20.536 cm (8.085 in) on either side of it. The y-coordinate is measured from the plane of symmetry, as shown in Fig. 2.

Test condition variations. - The quantitative effect of the presence of a particular gap configuration will be defined by comparing the perturbed value of the local heat transfer to the corresponding flat-plate value measured at the same nominal flow conditions. However, the exact flow conditions vary from run to run. Furthermore, since the data reduction method of ref. 1 utilized the total pressure in the stagnation chamber and the T_t values based on the three model-mounted, total-temperature probes (see Fig. 1), "spanwise" differences exist in the exact flow conditions for a given run condition. The effects of the run-to-run variations and of the spanwise variations are indicated by the theoretical heat-transfer distributions presented in Fig. 3. Theoretical solutions for the nominal, lowest Reynolds number condition represent all three of those for the C1, flat-plate, configuration, i.e., Run 38, and one of those for the C2, single-transverse-slot, configuration, i.e., Run 6. The spanwise differences are indicated by the AA, BB, and CC notation in Table 1 and in Figs. 3 and 4. Theoretical solutions for the highest Reynolds number represent all three of those for the C1 configuration, i.e., Run 41, and one of those for the C2 configuration, i.e., Run 9. The theoretical solutions were computed using the real-gas correlations for the thermodynamic properties and for the transport properties (see ref. 2) in the University's nonsimilar boundary-layer code, NSBL (ref. 3). The theoretical solutions indicate that the differences in the local heat-transfer rates due to the variations in the test conditions are small.

The heat-transfer distributions measured for the lowest Reynolds number condition, i.e., Run 38, and for the highest Reynolds number condition, i.e., Run 41, are included in Fig. 3. It is clear that the experimental variations in the heat-transfer rates measured during a given run are as great or greater than would be attributed to the variations in the flow conditions.

Flow model variations. - The effect of the assumed flow model on the theoretical, flat-plate, heat-transfer distributions is illustrated in Fig. 4. Theoretical solutions were computed for all four nominal test conditions using three different flow models.

- (1) NSBL, Perfect-gas. - These solutions were computed using the perfect-gas relations for the thermodynamic properties in the University's nonsimilar boundary layer code, NSBL (ref. 3).
- (2) NSBL, Real-gas. - These solutions were computed using the real-gas correlations for the thermodynamic properties and for the transport properties (see ref. 2) in the University's nonsimilar boundary layer code, NSBL.
- (3) BLIMP, Perfect-gas. - These solutions were computed using the perfect-gas relations in the University's copy of the BLIMP code (Ref. 4). Although the University's NSBL code is currently being modified to model transitional and turbulent boundary layers, only the BLIMP code can provide such solutions at this time. Therefore, in order to have theoretical solutions that can be compared with the transitional data, a transition criterion

(determined from the experimental heat-transfer distributions) of $(Re_{\theta}/M_e)_{tr} = 222.55$ was specified when computing the BLIMP solution.

Note that the BLIMP code and the NSBL code yield essentially identical solutions in the laminar region. The theoretical heating rates computed using the real-gas correlations are approximately ten per cent greater than those computed using the perfect-gas model. It is interesting to note that, except for the lowest Reynolds number (Fig. 4a), the perfect-gas solutions provide better correlations with the experimental distributions than do the real-gas solutions. The principal author had experienced similar problems applying the real-gas thermodynamic subroutine to relatively low-temperature-problems, where the air actually behaves as a perfect gas.

Note also that the transitional heat-transfer rates are not generally correlated when a single transition criterion, i.e., $(Re_{\theta}/M_e)_{tr} = 222.55$, is used for this flat-plate flow. Although the theoretical solution for the transitional heat-transfer is in good agreement with the data for $Re_{\infty,L} = 5.90 \times 10^6$, such is not the case for $Re_{\infty,L} = 8.11 \times 10^6$. In this latter case, the actual transition location is downstream of that predicted using the single criterion.

Transition. - The discrepancies described in the previous paragraph are attributed to the unit Reynolds number effect on transition. The transition locations determined using the heat-transfer distributions presented in Figs. 4b through 4d are summarized in Table 2. For each

of the three flow conditions, transition occurs nearest the leading edge in the plane for which $y = -0.135L$ and last in the plane for which $y = +0.135L$. The values of the transition parameters calculated using the nominal transition locations and the flow properties calculated using either the perfect-gas model or the real-gas model are presented in Table 2b and in Fig. 5. Even though the unit Reynolds number from Run 41 is 1.37 times that for Run 40, the transition location for Run 41 is 0.95 that for Run 40. Thus, $Re_{x,tr}$ increases significantly as the unit Reynolds number is increased. Many other investigators have observed that the transition Reynolds number increases with the unit Reynolds number, e.g., refs. 5, 6, 7, and 8. Several authors have stated that the unit Reynolds number effect could be explained by aerodynamic noise radiated from the turbulent wind-tunnel boundary layer. However, transition data for free-flight tests (ref. 8) also exhibit the unit Reynolds number effect. Such free-flight data do not clarify the question of whether the unit Reynolds number effect is indeed due to noise, since the mechanical noise of launch and of the machinery at a ballistic range may affect the results.

Power law correlations were developed by several authors to quantify the unit Reynolds number effect:

$$Re_{x,tr} \propto (Re/m)^n$$

where the exponent n may depend on the Mach number. If one uses the transition parameter suggested by McDonnell-Douglas (see ref. 9) for

the Shuttle:

$$\left[\frac{Re_\theta / M_e}{(Re/m)^{0.2}} \right]_{tr}$$

one obtains values from 10.30 to 11.19 for the test conditions of Table 2, independent of the flow model.

Three parameters that can be used to illustrate the size of the gap relative to the characteristic dimensions of the approach boundary layer are presented in Fig. 6. The displacement thickness, the momentum thickness, and the sonic point calculated at $x = 0.6L$ (0.9144 m) are presented as a function of the local Reynolds number at that point. This x -location is chosen since many of the transverse slots are located at this station. Three symbols are used to identify the flow model, while the flag notation is used to indicate the effects of the run-to-run variations and of the spanwise variations on the computed values. Note that when the boundary layer is laminar, the effects of the flow model and of the variations in the flow conditions are small.

The data presented in Figs. 4c, 4d, and 5 indicate that transition occurs upstream of this location when Re_x exceeds 3.10×10^6 . Although transition occurs upstream of this location when $Re_x = 3.54 \times 10^6$, the transitional values of the boundary-layer parameters (BLIMP, Perfect-gas) are virtually the same as the laminar values (NSBL, Perfect-gas). However, when $Re_x = 4.86 \times 10^6$, the transitional values are significantly different than the laminar values. Although the turbulence model used

in the University's version of the BLIMP code is relatively simple, the increase in δ^* and in θ in the transitional boundary layer is qualitatively similar to that obtained using more sophisticated turbulence models, e.g., ref. 10. Note how quickly the sonic point moves toward the wall as the Reynolds number increases.

Data for Configuration 2(C2)

An insert containing a single transverse gap was placed in the structural carrier plate to form Configuration 2 (C2). As shown in Fig. 7, the separation (upstream) step was at an x of 91.44 cm (0.60L). Referring to Fig. 4, the reader can see that the streamwise location of the gap was such that the unperturbed boundary layer was laminar at the two lower Reynolds-number conditions and was transitional at the two higher Reynolds-number conditions.

Since the width of the gap could be varied, heat-transfer distributions were measured for values of w equal to 0.127 cm (0.050 in), 0.254 cm (0.100 in) and 0.508 cm (0.200 in). Detailed sketches are presented in Figs. 7b through 7d to illustrate both the gap geometry and the thermocouple locations in the vicinity of the gap. Note that, although the location of the recompression (downstream) step is fixed (for illustrative convenience), in reality the upstream step was fixed. See Fig. 7a.

The insert was built so that the gap depth varied across (spanwise) the model, with instrumentation modules located at the centerline of each of three different gap-depth regions. As indicated by the

section views: for $y = +0.135L$ (section AA), $d = 1.016$ cm (0.400 in); for $y = 0.000L$ (section BB), $d = 2.032$ cm (0.800 in); and for $y = -0.135L$ (section CC), $d = 4.064$ cm (1.600 in).

The corner radius was 0.152 cm (0.0620 in) for all variations for this configuration.

Open cavity/closed cavity. - As discussed by Charwat et al (refs. 11 and 12) supersonic flow over a cut-out (or cavity) in the surface can produce either of two distinct, stable configurations. When the length-to-height ratio of the cut-out, or the width-to-depth ratio (w/d) in the present nomenclature, is sufficiently large, the flow reattaches to the cavity floor and the cavity is "closed". If the length of the notch decreases below a critical value, the flow bridges the gap. This is called flow with an "open" cavity. For short notches, where the length of the cavity is less than one-half the critical length, the pressure rise associated with the deceleration of the inner portion of the shear layer tends to propagate upstream and to thicken the shear layer. As a result the characteristics of the boundary-layer/free-stream interaction govern the pressure field.

The length-to-height ratio (w/d) of the gap geometries for C2 are presented in Table 3a. The maximum value of w/d , which is that for the 0.508 cm gap with the most shallow cavity (that at section AA), is only 0.500. Data presented by Charwat et al (ref. 11) indicate that the critical closure length for a two-dimensional notch in a turbulent boundary layer is approximately ten times the depth of the cavity for cavities where the separation step and the recompression step are of equal height. Thus, the cavities should be open for all of the C2 variations.

It should be noted that the present cavities are much shorter even than the nominal length that is required for the flow which separates from an isolated, rearward-facing step to impinge on the wall. Data presented by Charwat et al (ref. 11) indicates that a two-dimensional flow impinges on the wall approximately $7d$ downstream of the step if the boundary layer is laminar and approximately $5d$ downstream for a turbulent boundary layer. The geometry of the wake is approximately constant over the mid-supersonic Mach-number range, since the decrease in the base pressure is related to the length/height ratio by the Prandtl-Meyer expansion relations. The extremely small gap widths of Configuration 2 could allow the gap-induced perturbations to propagate upstream.

Basic heat-transfer distributions. - The heat-transfer measurements for $0.575L \leq x \leq 0.700L$ for C1 and for C2 are compared in Fig. 8 for two flow conditions for which the approach boundary layer was laminar. Recall that, for all gap widths, the vertical face of the separation step was at $x = 0.60L$ (91.44 cm). Thus, these data illustrate the effect of the gap on the upstream heat-transfer distribution as well as that for a distance downstream of the gap of approximately one shuttle-tile length. Data are presented only for $y = 0.000L$ (i.e., the BB section of Fig. 7c), for which the depth of the gap was 2.032 cm (0.800 in).

The heat-transfer rate for the C2 configuration increases slightly as the flow approaches the gap, decreases rapidly around the corner of the separation step, increases rapidly around the corner of the recompression step (reaching a maximum at the tangency point), and follows

(at slightly lower magnitudes) the heat-transfer distribution for an undisturbed laminar boundary-layer. Note that the maximum heating for these particular runs, i.e., runs 54-60, never exceeded the local value measured on the flat-plate configuration at the corresponding nominal test conditions. This is not altogether surprising since other investigators (e.g., refs. 13 and 14) have found that the laminar heating rates in the vicinity of a very short gap are only slightly different (both higher and lower) than the flat plate values. However, as will be discussed subsequently, the peak local heating rates measured during runs 6-16 exceeded (slightly) the flat-plate values at these same nominal test conditions. As noted in ref. 1, runs 1-37 were made during the OH2A phase of the program, while runs 38-81 were accomplished during OH2B. During the interim, insert 2 was modified to accommodate different thermocouple locations. For several test conditions, the heating rates measured for a given test condition during OH2A were significantly greater than those obtained during OH2B. The source of this discrepancy is not known.

Note that the local peak heating on the recompression step occurs at the tangency point of the upper (flat) surface. Thus, the peak heating does not occur where the impinging flow "stagnates" on the "recompression face". The quotes are used because the corner radius affects the character of the impinging flow for these short cavities. The local heating peak is attributed to the fact that large velocity gradients in the flow which has bridged the gap affect the gradients in the boundary layer developing on the recompression step. The increased heating on the upstream surface indicates that the pressure rise created by the impingement process propagates upstream through the relatively thick subsonic portion of

the shear layer. The resultant adverse pressure gradient thickens the boundary layer prior to separation, deflects the external flow, and causes the local increase in the heat-transfer rate.

There is no significant effect either of the gap width (w) or the Reynolds number evident in these particular measurements. However, impingement heating-rate measurements reported by Avery (ref. 14) did not significantly exceed the flat-plate values until the gap width was 0.3 cm in a laminar boundary layer where δ^* was 0.57 cm. Thus, the data indicate that as long as the gap width is below some critical value, locally high heating rates can be avoided. The critical gap width is a function of the boundary layer character and thickness.

The heat-transfer distributions from $0.60L \leq x \leq 0.70L$ are compared for C1 and C2 in Figure 9 over the complete Reynolds-number range using data from the OH2A phase of the test program. The streamwise distributions are presented starting from the (lower) tangency point in the cavity. Again, data are presented only for $y = 0.000L$.

Consider first the lowest Reynolds number measurements of Fig. 9a. Recall that this was the only flow condition for which the flat-plate measurements were significantly greater than the NSBL, perfect-gas theory (see Fig. 4a). The heat transfer data of Fig. 9a indicate that the peak values did not occur on the upstream-facing surface of the corner radius. They occurred either at the thermocouple located at the (upper) tangency point for the plate surface (for $w = 0.254$ cm and $w = 0.508$ cm) or at the first thermocouple downstream of the upper tangency point (for $w = 0.127$ cm). See Fig. 7c for the thermocouple locations. Except at these thermocouples near the upper tangency point, the heating rates

measured in the vicinity of the gap were equal to or less than the corresponding flat-plate values. Because the boundary layer was laminar and relatively thick (see Tables 3b and 3c), the adverse pressure gradient generated as the flow encountered the recompression step propagated upstream through the subsonic portion of the viscous layer, thickened the approach boundary layer, and actually reduced the local heat-transfer rate to most of the surface. Dunavant and Throckmorton (ref 13) reported no appreciable increase in the heating where the boundary layer bridged the gap. Bohon et al (ref. 15) reported no significant spikes or hot spots for a "stacked configuration" of tiles, i.e., one in which there is no longitudinal channel intersecting (perpendicular to) the gap. Note that for these flow conditions, the peak heating in the impingement region is greatest for the widest gap.

For $Re_{\infty,L} = 4.01 \times 10^6$ (Fig. 9b), the peak heating in the impingement region is only slightly greater than the flat-plate values. This conclusion is consistent with that based on the lower-Reynolds-number data. However, contrary to low-Reynolds-number observations, there is no effect of the gap width evident in these data at these flow conditions. The streamwise variation of the heat-transfer rates measured downstream of the gap suggest the onset of transition. However, since the deviation from laminar theory is not large and since data are not available from further downstream, one cannot quantify the effect.

The heat-transfer distributions for the two higher-Reynolds-number cases are presented in Figs. 9c and 9d. As indicated by the filled symbols, the flat-plate boundary layer was itself transitional for these two flow conditions. With the exception of the data for the shortest gap for

$Re_{\infty,L} = 5.90 \times 10^6$, the heating rates exceed the flat-plate values at all points. Because only the lower portion of the shear layer reattaches to the downstream step, the "stagnation" heating on the recompression face is not the maximum value measured in this region. Instead the maximum heating occurs near the tangency point of the upper surface where the relatively high (velocity and temperature) gradients in the reattaching shear layer (which provides the "edge" conditions for the developing boundary layer) affect that boundary layer. Thus, engineering correlations which model the stagnation-point heat transfer for an impinging jet, e.g., ref. 16, would not be expected to accurately predict the peak heating in the vicinity of the gap. At these high Reynolds numbers, the heating rates downstream of the gap are higher than the corresponding flat-plate values. Although the experimental values do not exceed the fully turbulent values, the instrumentation does not extend far enough downstream to be certain that the experimental heating rates would not significantly exceed the theoretical turbulent values. However, boundary-layer solutions generated for Run 41,BB using the BLIMP code with several different assumptions for the transition location indicate that the theoretical, turbulent, flat-plate heating rates are independent of the transition location at points sufficiently downstream of the transition location. Since the upstream boundary layer is transitional for these two Reynolds numbers, the subsonic portion of the boundary layer decreases rapidly with Reynolds number (refer to Table 3c). Thus, the ability of the recompression step to alter the upstream flow and, thereby, to spread out the recompression process is reduced. The ratio of the gap-perturbed heating rate increases rapidly as the Reynolds number increases (or as the sonic point moves near the wall).

Except for one set of data, the peak value of the "impingement heating rate" increases with increasing gap width for both Reynolds numbers. That the impingement heating increases as the gap width increases has been reported in refs. 14, 16, and 17 for a laminar boundary layer and in refs. 14 and 15 for a turbulent boundary layer. However, as discussed previously, not until the gap width (actually, the streamwise length of the gap) exceeds some critical value (which is a function of the flow characteristics) do the local heating rates become relatively high.

It was noted in the previous paragraphs that two sets of data produced results contrary to the typical trends. One set is that for the shortest gap ($w = 0.127$ cm) for $Re_{\infty,L} = 5.90 \times 10^6$. It should be noted that, although there are only a few data points from the $y = 0.000L$ plane in Fig. 9c, the heating-rate distributions from the $y = \pm 0.135L$ planes were similar. The heating downstream of the gap closely follows the laminar theory for this test condition. Thus, this heat-transfer distribution is similar to those obtained at the two lower Reynolds numbers (Fig. 9a and 9b). However, since the flat-plate boundary layer was transitional, it is surprising that the gap-perturbed flow appears laminar. A possible explanation is that the basic flow is borderline stable and in one run transition began in this region and in another the boundary layer remained laminar. The theoretical characteristics calculated for this transitional boundary layer were little different from those calculated for a laminar boundary layer. Thus, since the oncoming boundary layer was relatively thick and the subsonic region relatively large, the short gap had little effect on the flow. For the two longer gaps, the flow perturbations were sufficiently strong to promote transition.

The second set of anomalous data are those for the longest gap ($w = 0.508$ cm) for $Re_{\infty,L} = 8.11 \times 10^6$, which are presented in Fig. 9d. The reason why these heating rates appear to be relatively low is not understood. Again, the heating rates measured in the $y = \pm 0.135L$ planes exhibit the same characteristics as the data from the $y = 0.000L$ plane.

When discussing the trends exhibited by the data, it was noted that although the results were presented only for the $y = 0.000L$ plane, the distributions for the $y = \pm 0.135L$ planes were similar. This is illustrated in the heat-transfer distributions presented in Fig. 10 for a single, transverse gap, 0.254 cm wide. Data are presented for all three spanwise locations. The differences between the three heating rates measured at a given x -location are significant and usually increase with increasing Reynolds number. Recall that the depth of the notch differed for the three sections. For a given Reynolds number, the perturbed heating rates are usually greatest for the thermocouples of section AA and least for those of section CC. Although there are numerous exceptions to this trend of increased heat flux with increased values for the ratio w/d , it is consistent with the analysis of Nestler (ref.16). Note that the magnitudes of the differences depend on the Reynolds number, the gap width, the streamwise location, and experimental accuracy.

As has been discussed, the peak value of the impingement heating rate (usually) increases with gap width, once the gap width exceeds a critical value. Furthermore, the critical value is a function of the flow characteristics. This is summarized in the data presented in Fig.11. For the two lower Reynolds-number flows, the heating is relatively unaffected by

presence of the gap for all three widths treated. When $Re_{\infty,L} = 5.90 \times 10^6$, the maximum values of the impingement heating rate (for three spanwise locations) for the short gap, i.e., $w = 0.127$ cm, are essentially equal to the flat-plate value. Recall that the heat-transfer rates measured downstream of the gap follow the laminar theory even though the measured flat plate values indicate the onset of transition. For this Reynolds number, the maximum values of the impingement heating rates are significantly above the measured flat-plate values, and (with the exception of the data for section AA), they increase with gap width. When $Re_{\infty,L} = 8.11 \times 10^6$ (the highest Reynolds number of the present test program), the maximum value of the heating rate in the impingement region exceeds the flat-plate values for all gap widths from the OH2A tests and, with the exception of the data for the widest gap for all three sections, increases with gap width. Note that as discussed before, the heating rates obtained during the OH2B phase of the program are relatively low (for an unknown reason).

Correlations. - As discussed, the gap-induced increases in the local heating rates clearly depend on the Reynolds number, but they also depend on the gap width (although there is no clear functional relationship) and on the gap depth. This is illustrated by the data presented in Fig. 12.

When the upstream boundary layer is laminar, there is (at most) a slight increase in the heating near the gap, while the heating downstream of the gap was generally lower than the corresponding flat-plate values. However, at the higher Reynolds numbers, i.e., $Re_{\infty,L} \geq 5.90 \times 10^6$, the undisturbed boundary layer was transitional and significantly higher heating rates were measured in the vicinity of the gap. Two mechanisms produced these

locally high heating rates: (1) large gradients in the reattaching shear layer which affected the development of the boundary layer as it formed on the reattachment step and (2) the promotion of transition which affected the heating rates at downstream points.

Since the peak impingement heating rates near the gap were essentially unchanged from the flat-plate values as long as the boundary layer was laminar, the Reynolds number effect could be correlated by:

$$\frac{\dot{q}_{pk,i}}{\dot{q}_{fp}} = 1.0 + A(Re_x - Re_{x,tr})^a$$

As long as the local Reynolds number (Re_x) is less than the transition criteria ($Re_{x,tr}$), the second term should be equal to zero. Thus, for $Re_x \leq Re_{x,tr}$,

$$\frac{\dot{q}_{pk,i}}{\dot{q}_{fp}} = 1.0$$

Note that this correlation neglects the effects of the gap geometry which are present whether the boundary layer is laminar or turbulent. Although these effects are not negligible provided the gap is sufficiently wide, they were not large nor were they consistent enough to be correlated for the present flow conditions.

To select a value for the exponent a , which would be valid both at the wind-tunnel conditions and at flight conditions, it is necessary to identify the phenomena associated with the heating increase. The theoretical values of δ^* and of θ increase slightly with Reynolds number for

the transitional flows. Thus, they do not appear to be the appropriate correlation parameters. Note, however, that in the transitional regime, the z-coordinate of the sonic point decreases rapidly as the Reynolds number increases. As indicated by the solutions presented in Fig. 13,

$$\frac{z^*}{x} \propto \frac{1}{(Re_x)^{3.5}}$$

As the sonic point moves toward the wall, there is a corresponding increase in the velocity and the temperature gradients near the wall. Since the peak heating rates in the impingement region are attributed to the large gradients in the reattaching shear layer, let us assume the value of a to be 3.5. Using the transition data presented in Table 1 (and accounting for the unit Reynolds number effect), the transition Reynolds number at the C2 gap is 3.10×10^6 . The correlation:

$$\frac{\dot{q}_{pk,i}}{\dot{q}_{fp}} = 1.0 + 1.785 \times 10^{-22} (Re_x - 3.10 \times 10^6)^{3.5} = \left\{ \text{Reynolds Number} \right\}$$

is compared with the data in Fig. 12a. Although the variations in the parameter $\dot{q}_{pk,i}/\dot{q}_{fp}$ at a given Reynolds number are associated (at least in part) with the gap dimensions, no consistent correlation is evident in these data.

A correlation accounting for the heating perturbation due to the gap could be:

$$\frac{\dot{q}_{pk,i}}{\dot{q}_{fp}} = 1.0 \left\{ \text{Geom} \right\} \left\{ \text{Reynolds Number} \right\}$$

where the factor accounting for the geometry, $\left\{ \text{Geom} \right\}$, might be:

$$\text{Geom} = 1.0 + B \left[\left(\frac{W}{d} \right) - \left(\frac{W}{d} \right)_{\text{crit}} \right]^b$$

As with the Reynolds number, it is assumed that there is no significant gap-geometry effect until the length-to-height ratio exceeds a critical value (which is a function of the Reynolds number).

Data for Configuration 3(C3)

An insert containing multiple, transverse gaps was placed in the structural carrier plate to form Configuration 3(C3). As shown in Fig. 14, the gaps, which were 0.254 cm wide, were 15.24 cm apart. Referring to Fig. 4, the reader can see that, over the range of flow condition, the flat-plate boundary layer was laminar for all of the gap locations but that of the most downstream gap. And only at the two higher Reynolds numbers was the unperturbed boundary layer transitional in that region.

The experimental heat-transfer distributions for Configuration 3 are presented in Fig. 15. The gap locations and the flat-plate transition location for each Reynolds number are illustrated in these figures. When studying the heat-transfer distributions, the reader should note that, with the exception of the thermocouples located near $x = 0.6L$, they are on the flat surface parallel to the free stream.

At the lowest Reynolds number ($Re_{\infty, L} = 2.57 \times 10^6$), the C3 measurements closely follow the laminar theory. Recall that, for this one flow

condition, the flat-plate data are significantly above the laminar theory. Thus, the presence of the multiple transverse gaps causes a general reduction in the surface heating for this low Reynolds-number flow. For $x \geq 0.4L$, the roughness-induced perturbations produce an erose heating distribution. The distribution for $Re_{\infty,L} = 4.01 \times 10^6$ (Fig. 15b) is similar to that measured at the lower Reynolds number. Note that the heat-transfer rates measured in the region $0.6L < x \leq 0.7L$ are essentially equal to the theoretical values for a laminar flat-plate boundary layer. Since transition of the flat plate was observed at $0.75L$, these data indicate that the presence of the multiple, transverse gaps did not dramatically affect the transition location.

For the two higher Reynolds-number flows, the gap-induced perturbations to the flow cause larger variations in the heat transfer in the laminar region and cause transition to occur slightly earlier than for the flat-plate boundary layer. Furthermore, as evident in Fig. 15d, the streamwise increase in heating in the transitional region is much greater for these C3 measurements than that which occurred for the "natural" transition on the flat-plate configuration. Thus, it seems that tripping the boundary layer causes the transition process to proceed much more rapidly. Despite the rapid streamwise increase in the local heating rates, they do not exceed the values for a turbulent, flat-plate boundary layer (see Fig. 9d) over the limited length for which data are available.

Thus, over the entire Reynolds number range, the C3 heat-transfer rates were lower than the corresponding flat-plate values as long as the boundary-layer remained laminar. This is consistent with the results of previous investigators. Charwat (ref. 18) cites supersonic data for a series of notches with w/d between 1 and 2 which are spaced one cavity

length apart. The notched surface "shielded" the body somewhat, so that the total heat flux was about 70 to 80% of the heat flux to an equal length of a smooth-surfaced body. Charwat notes that the downstream heating will usually be decreased unless the cavity induces transition. For the present tests, the multiple transverse gaps, which were relatively narrow (0.254 cm) moved the onset of transition only slightly upstream. Recall that the flow is supersonic ($M_e = 5.10$) and $T_w \approx 0.25 T_t$.

Data for Configuration 4 (C4)

An insert containing three parallel, longitudinal gaps (or slots) which intersect a single, transverse gap was placed in the structural carrier plate to form Configuration 4(C4). As shown in Fig. 16, the longitudinal slots were either 1.016 cm deep (which is at $y = + 0.135L$), 2.032 cm deep (which is at $y = 0.000L$), or 4.064 cm deep (which is at $y = -0.135L$). Note that thermocouples are located in-depth at one section (i.e., one x-location), DD, of the shallow slot, at two sections, AA and BB, of the slot located along the centerline, and at one section, CC, of the deepest slot.

The transverse gap is essentially that for C2. Recall that the transverse gap insert was built so that its depth varied across the model (spanwise), with instrumented modules located at the centerline of each of the three different gap-depth regions. Thus, at a given y-station, the depth of the transverse gap is equal to that of the intersecting, longitudinal slot. Thermocouples located on the recompression face of the transverse gap (see sections AA and BB in Fig. 7) provide the heat-transfer distribution downstream of the T-type intersection. All of the gaps (and slots) were 0.254 cm wide.

Locally high heating rates were measured at various thermocouples for Configuration 4. They were due to two distinctively different mechanisms. Locally high heating rates occur on the (upstream-facing) recompression surface at the "T" formed by the intersection of the longitudinal slot and the transverse gap. The data of Dunavant and Throckmorton (ref. 13) failed to show a region of intense heating on the upstream face at the gap intersection for turbulent flows. Note that the $(x_s - x_0)$ for their model was 1.49. The measurements of Avery (ref. 14) indicate that the impingement-region heating rates increase with increasing w , being a maximum of 2.2 times the flat-plate value for laminar flow and 4.5 times the flat-plate value for a turbulent boundary layer. Avery noted that the length of the longitudinal slot was an important parameter even though he did not have sufficient data to define the dependence. For the configurations of ref. 14, $(x_s - x_0)$ was 2.40 to 4.80. Johnson (ref. 19) reported the local heating increased by over an order of magnitude in the impingement region. The heating-rate ratio was reduced dramatically when the thickness of the turbulent boundary layer was increased by an order of magnitude. The $(x_s - x_0)$ ratio was 8.0 for the models of ref. 19. Comparing the results of these investigators, it is clear that the heating increase in the impingement region increases dramatically with $(x_s - x_0)$. The phenomenon appears to be similar to that for a two-dimensional notch where the characteristics of the flow-field perturbations depend on whether the notch is "open" or "closed". Thus, the magnitude of the heating increase in the impingement region of a T depends on many parameters, including: δ^* , w , $(x_s - x_0)$, and the Reynolds number.

Basic heat-transfer measurements along the length of the longitudinal slot.

Locally high heating rates were also measured along the length of the longitudinal slot. Because the flow spills into the slot, the boundary layer on the flat surface thins with a corresponding increase in the local heating. This latter mechanism is illustrated in the data presented in Figs. 17 and 18.

Presented in Fig. 17 are the heating rates recorded by the three thermocouples which are nearest the flat surface for the four stations along the longitudinal slot (refer to Fig. 16). Included for comparison are the perfect-gas solutions for a laminar, flat-plate boundary layer as computed using the University's NSBL code. Heating rates were measured at all four stations for three of the Reynolds-number conditions. These measurements are represented by the open symbols of Fig. 17. A second set of runs were made for three of the Reynolds-number conditions (two of them being common to those of the first set of runs) in which data were obtained at section BB only. These measurements are represented by the filled symbols. Thus, the measurements presented in Fig. 17 indicate the effect of the unit Reynolds number, of the distance from the beginning of the slot, and of the depth of the slot. Recall that the width of the slot was 0.254 cm for all C4 runs.

At all three Reynolds numbers, the heating rates measured at the two sections located at $x = 0.4L$ are higher for the deeper slot. Note also that for the shallow slot ($d = 1.016$ cm), the heating is always greatest at the thermocouple at the upper tangency point (i.e., on the flat surface). However, for the deeper slot

($d = 4.064$ cm), the heating is greatest at the thermocouple on the radius. These observations are consistent with the assumption that the increased heating results because the boundary layer thins as the flow spills into the slot. The level of heating tends to increase with distance from the beginning of the slot.

The ratio of the C4 heating rates to the experimental flat-plate value at the same x -location are presented as a function of $Re_{(x-x_0)}$ in Fig. 18. The peak value (\dot{q}_{pk}) is the numerator of Fig. 18a, while the heating rate measured at the upper tangency point (\dot{q}_{utp}) is the numerator for Fig. 18b. The ratio $\dot{q}_{pk}/\dot{q}_{fp}$ correlates reasonably well as a function of $Re_{(x-x_0)}$, increasing "linearly" with the Reynolds number until it is approximately constant, just less than 3.0. Note that the ratio is smallest for the slot with the smallest d (i.e., the most shallow section, section DD). Thus, some of the scatter in the correlation could be reduced by accounting for the (nonlinear) effect of d .

Basic heat-transfer measurements downstream of the T gap.

The streamwise heat-transfer distributions downstream of the T gap are presented in Figs. 19 and 20. The actual heating rates are presented in Fig. 19, while the values of the ratio \dot{q}/\dot{q}_{fp} are presented in Fig. 20. The measurements are from the $y = 0.000L$ plane, which is downstream of the 2.032 cm deep slot, and from the $y = +0.135L$ plane, which is downstream of the 1.016 cm deep slot. Thus, these heating-rates represent the measurements from the thermocouple locations shown in Figs. 7b and 7c, starting with the thermocouple at the lower tangency point in the gap and proceeding downstream onto the plate.

Note that the $(x_s - x_0)$ ratios for the longitudinal slots are 30 and 60, respectively. Thus, the relative lengths of the longitudinal portion (termed the slot in the present report) of the T gaps in the present study are significantly greater than those of the previous investigations. The heat-transfer is markedly greater downstream of the deeper slot, being an order of magnitude greater than the flat-plate values. Note that these peak values for the ratio \dot{q}/\dot{q}_{fp} are significantly greater than those of the previous investigations where $(x_s - x_0)$ was 5.0, or less. However, since the heating rates are greatest downstream of the deeper slot (which has the lower $(x_s - x_0)$ ratio of the two), these data indicate that the depth itself is a significant parameter once $(x_s - x_0)$ is sufficiently large. The heating remains significantly greater than the corresponding flat-plate values well downstream of the corner.

Included for comparison are the heating-rates measured downstream of the single, transverse gap (C2), which were discussed earlier, e.g., Fig. 9. The heating rates downstream of the T gap (C4) are much greater than those measured downstream of the single, transverse gap both for the shallow slot and for the deeper slot. Note that, at the highest Reynolds number, the heating rates to the flat surface downstream of the T gap exceed the theoretical values for a flat-plate boundary layer which is turbulent from the leading edge.

Rapid variations in the heating rate which occur over very short distances on the corner radius of the recompression surface are evident in the streamwise heat-transfer distributions presented in Figs. 19 and 20. The variations in heat transfer on the recompression surface are more clearly illustrated in Fig. 21, where the heating-rate ratio is presented as a function of the vertical distance from the surface

relative to the depth of the gap. These heating rates represent the measurements from the thermocouple locations shown in Figs. 7b and 7c, starting with the thermocouple at the upper tangency point and proceeding down toward the floor. The local heating rate on the recompression surface has been divided by $\dot{q}_{fp,1}$ which is the experimental flat-plate value for $x = 0.6L$ and for the same y . Note that the peak values and the variations in the heating-rate ratio increase with the Reynolds number and with d . At the highest Reynolds number, the heat-transfer rate at the bottom of the deeper T-gap is $0.62 \dot{q}_{fp,1}$.

The isometric heating-rate contours presented by Avery (ref. 14) indicate that, for laminar flow in a relatively narrow gap ($w = 0.18$ cm), the flow in the T gap is primarily two dimensional and the longitudinal slot flow has a negligible effect on the heating rates. For laminar flow for a gap width of 0.41 cm and for turbulent flow for both gap widths, the isometric heating-rate contours of Avery indicate that the flow in the T gap is three-dimensional.

The vertical heat-transfer distribution obtained at the lowest Reynolds number for the more shallow slot (Fig. 21a) increases monotonically from $0.02 \dot{q}_{fp,1}$ at the floor ($z = 1.0d$), reaching a maximum of $2.10 \dot{q}_{fp,1}$ at $z = 0.05d$. However, the vertical heat-transfer distributions obtained at the higher Reynolds numbers indicate a more complex, three-dimensional flow-field at the intersection of the longitudinal slot and the transverse gap. Multiple local maxima occur in the vertical distributions, e.g., local peaks occur at z 's of $0.025d$, $0.369d$, and $0.600d$ of the deeper slot for $Re_{\infty,L} = 4.01 \times 10^6$ (Fig. 21b). Because of the long length of the longitudinal slot, the flow attaches to the

floor and the recompression surface serves as a forward facing step. The side-wall boundary layers and the cross-flow into transverse gap contribute to the three-dimensional character of the viscous interactions at the higher Reynolds numbers.

It has been noted that two sets of runs were made using the C4 with different instrumentation hook-ups. The run schedule was such that heat-transfer distributions were obtained on the recompression surface for the two lower Reynolds-number conditions. Thus, data are available which indicate the run-to-run variations in the heating rates. Presented in Fig. 22 are such data, i.e., the vertical heat-transfer distributions along with the recompression surface for $Re_{\infty,L} = 4.01 \times 10^6$. There are considerable differences between the two sets of data from the more shallow section (Fig. 22a). The multiple peaks with a maximum heating rate of $4.82 \dot{q}_{fp,1}$ for the data from Run 27 suggest a complex flow with strong, viscous interactions. The heating rates from the "limited instrumentation run", Run 30, are relatively constant and relatively low, $\dot{q} = 1.6 \dot{q}_{fp,1}$, over the upper one-half of the step. Significant localized differences also occur in the distributions obtained for the deeper section, i.e., $d = 2.032$ cm (Fig. 22b). Note that the heating rate increases monotonically from the floor to $z = 0.235d$ for Run 30, whereas two local maxima appear in this region for the heating-rate distribution from Run 27. Although significant differences between the two distributions also occur nearer the surface, the magnitudes of the heating rates from the two runs are roughly the same. Furthermore, recall that the (few) heating rates measured along the longitudinal

portion of this configuration (for which $d = 2.032$ cm) were in excellent agreement for these two runs (Fig. 17b). Thus, it appears that the flow-fields for the two runs were similar and that subtle, but substantial, run-to-run variations in the impingement flow-field produce significant variations in the heating.

Correlations. - Based on the discussion of the basic data presented thus far, one would not expect the correlations developed using data from investigations where the $(x_s - x_0)$ of the longitudinal slot was relatively small to work with the data from the present program. This lack of correlation is illustrated in Fig. 23.

Dunavant and Throckmorton (ref. 13) hypothesized "that as the streamwise gap length increases, the flow within the gap approaches a fully developed channel flow, and the rate at which this occurs is dependent upon the shear layer stress or the external boundary-layer thickness." The heating increase at the gap intersection for a thick, turbulent boundary layer was correlated in terms of the parameter:

$$\left[\frac{\delta^*}{x_s - x_0} \right] \left[\frac{z}{w} \right]$$

Bohon et al (ref. 15) added to the data base and modified the correlation parameter to the form:

$$\left[\frac{\delta^*}{w} \right]^2 \left[\frac{z}{x_s - x_0} \right]$$

To include laminar data in the correlation, Avery (ref. 14) modified the parameter by including a ratio ϕ^6 , where ϕ is the ratio of the theoretical heating rate for a turbulent flow divided by the theoretical heating rate for the actual flow conditions over a smooth surface.

Thus, the correlation parameter used by Avery was:

$$\left[\frac{\delta^*}{w} \right]^2 \left[\frac{z}{x_s - x_0} \right] \phi^6$$

The heating-rate ratios $(\dot{q}/\dot{q}_{fp,1})$ for the recompression surface as measured in the present program are presented as a function of the Bohon et al parameter and of the Avery parameter in Figs. 23a and 23b, respectively. Note that the parameter used in Fig. 23a can be rewritten

$$\left[\frac{\delta^*}{w} \right]^2 \left[\frac{z}{x_s - x_0} \right] = \left[\frac{\delta^*}{w} \right]^2 \left[\frac{z}{d} \right] \left[\frac{d}{x_s - x_0} \right]$$

The value of $(x_s - x_0)$ for the slot which was 2.032 cm deep (the data for which are the filled symbols) is twice that for the slot which was 1.016 cm deep (open symbols). Noting that the filled symbols are shifted to the right of the open symbols by approximately a factor of two, it is clear that a parameter such as:

$$\left[\frac{\delta^*}{w} \right]^2 \left[\frac{z}{d} \right]$$

would be better for the present configurations. However, this modified parameter does not uniquely correlate all the data, since the maximum values of $\dot{q}/\dot{q}_{fp,1}$ for the deeper slot (filled symbols), which occur for the lower values of

$$\left[\frac{\delta^*}{w} \right]^2 \left[\frac{z}{x_s - x_0} \right]$$

would still be greater for a given value of

$$\left[\frac{\delta^*}{w} \right]^2 \left[\frac{z}{d} \right]$$

at the lower end of the scale. Based on the comparison between the present data and those of other investigators, it appears that $(x_s - x_0)$ is an important parameter until it becomes sufficiently large. Then its numerical value does not matter and d (or d/δ^*) becomes more important.

For the present report, the ratio ϕ represents the ratio of the theoretical heat-transfer for a turbulent boundary layer where transition was assumed to occur at the leading edge divided by the flat-plate heating rate measured at the actual flow conditions. Note that virtually all of the data from the present tests are considerably above the correlation of ref. 14.

Using a regression analysis for the data, the following correlation was developed for laminar flow (ref. 14):

$$\frac{\dot{q}}{\dot{q}_{fp}} = 17,000 \left[\frac{\delta^*}{w} \right]^{-1.12} (Re_{x_s})^{-0.53} (Re_{(x_s - x_0)})^{-0.07}$$

For the flow conditions of the present test program, w , x_s , and $(x_s - x_0)$ were constant and

$$\delta^* \propto \frac{1}{(\text{unit Reynolds number})^{0.5}}$$

Thus, the laminar correlation would be relatively insensitive to Reynolds number over the range of test conditions in the present program and would be independent of the depth of the gap. This is definitely not the case, as has been discussed and as is evident in Fig. 24. The maximum heating rate measured on the recompression surface (divided by $\dot{q}_{fp,1}$) is presented as a function of the local Reynolds number based on the length of the longitudinal gap, $Re_{(x_s - x_0)}$. Furthermore, the heating is much higher for the compression surface downstream of the deeper gap. The heating-rate ratios for the highest Reynolds number fall well below these "linear" correlations.

The local flat-plate heating rates used in the denominator of Fig. 24 are presented in Fig. 25. Note that the measured heating rates are in good agreement with the theoretical laminar values computed using the perfect-gas relations in the NSBL code for the three lowest Reynolds numbers (including the Reynolds number just beyond transition). The data for the highest Reynolds number (where the flow is transitional) are well above the theoretical, laminar value. If the transitional character of the flat-plate flow does not govern the flow in these relatively long T-gaps, then $\dot{q}_{fp,1}$ would not be a suitable factor in developing a correlation for the peak heating. This may explain (at least partially) why the ratio of $\dot{q}_{pk,i}/\dot{q}_{fp,1}$ appears to be low at the highest Reynolds number.

The modified C4 configuration. - It has been noted that the heating-rate ratios for the recompression surface are a function of the gap depth and of the Reynolds number. These trends were also observed in the heat-transfer distributions which were obtained for a modified C4 configuration. For the modified C4 configuration, the recompression surface downstream of the three longitudinal slots, i.e., that portion of the insert downstream of $x = 0.6L$ (see Fig. 16) was raised 0.1588 cm (0.0625 in) above its normal position. Thus, although the geometry of the longitudinal slots was unchanged, the height of the recompression step (d) was 1.175 cm for the $y = +0.135L$ instrumentation (a 15.6% increase above the basic C4 configuration) and was 2.191 cm for the $y = +0.000L$ instrumentation (a 7.8% increase).

The heating rates measured at the thermocouples located along the length of the longitudinal slot, sections AA through DD of Fig. 16 (which

are not presented in this report), were unaffected by the changes in the height of the recompression surface. This is as expected, since the geometry of the slots were unchanged and the effect a step at the T intersection should not be felt at these upstream thermocouples.

Heat-transfer distributions are presented in Figs. 26 through 29 as a function of the distance below the horizontal surface (z/d) for the upstream-facing recompression surface and as a function of the streamwise distance (x/L) for the horizontal surface starting immediately downstream of the T-type intersection. Data are presented for the two lowest Reynolds numbers of the test program. Changing the height of the recompression step had a marked effect on the heating-rate ratios for the thermocouples in the $y = +0.135L$ plane for $Re_{\infty,L} = 4.01 \times 10^6$ (see Fig. 28). Note that the relative increase in the step height was greatest for this y section and that this is the higher Reynolds number. The differences between the heating-rate ratios for the modified C4 configuration and those for the basic C4 are relatively small for the other three conditions. Thus, the trends exhibited by these data are consistent with the trends for the basic C4. However, quantitative correlations for the very large increases in the heating-rate ratios exhibited by the modified C4 data presented in Fig. 28 were not attempted. Recall the comments made earlier that subtle, but substantial, run-to-run variations in the impingement flow-field produce significant variations in the heating.

Data for Configuration 5(C5)

An insert containing diagonal, intersecting gaps (or slots) was placed in the structural carrier plate to form Configuration 5(C5). The slots, which are 0.254 cm wide and 2.032 cm deep, are perpendicular to each other. As illustrated in Fig. 30, the slots were aligned such that one was inclined 30° to the free-stream flow and the other 60° to the flow.

Thermocouples were located on the flat surface, upstream and downstream of the gaps, and in the gaps themselves in planes parallel to the free-stream flow. The thermocouple locations for these sections are presented in Fig. 30. The thermocouple locations are such that heating-rate distributions are obtained (1) in the vicinity of the 30° -skewed gap where the boundary layer is always laminar (section AA), (2) in the vicinity of the 60° -skewed gap where the boundary layer is perturbed by the first gap and the unperturbed boundary layer is transitional at the higher Reynolds numbers (section BB), (3) near the intersection of the gaps (section DD), and (4) at other sections along the 60° -skewed gap. For one set of runs (i.e., Runs 46-49), heat-transfer rates were measured using the thermocouples from sections AA, CC, DD, EE, and FF. For the other set of runs (i.e., Runs 50-53), the heat transfer distributions were obtained for sections AA, BB, DD, and FF.

The heat-transfer-rate distributions are presented in Figs. 31 through 34 for Reynolds numbers based on the total plate length ($Re_{\infty,L}$) of 2.57×10^6 , 4.01×10^6 , 5.90×10^6 , and 8.11×10^6 respectively. Data are presented for each of the two instrumentation set-ups. The

x-location of the vertical recompression surface for each of the instrumented sections are also shown. Included for comparison are the heat-transfer-rate measurements for the flat-plate configuration (C1) at the same flow conditions, which are represented by the filled symbols.

As can be seen by comparing the data presented in Fig. 31a with those of Fig. 31b, significant run-to-run variations occurred. However, the differences between the heating rates at a particular thermocouple, which are of the order of 25%, do not change the conclusions regarding the effect of the gaps. As can be seen in Fig. 31, the heat-transfer rates are only slightly affected by the presence of the gaps at the lowest Reynolds number, i.e., 2.57×10^6 . Locally high heating rates were measured at the thermocouples at, and just downstream of, the upper tangency point of the "recompression" surface. This is true for all sections, even the one at the intersection of the gaps (i.e., section DD, the data for which are represented by \diamond). These trends are similar to those observed for the single, transverse-gap (C2) in the lowest Reynolds-number stream. The corresponding C2 data were presented in Figs. 8 and 9. Thus, the gaps of the C5 configuration which are swept either 30° to 60° to the flow, have roughly the same effect on the heating rates as does the transverse gap of C2. In a study of the aerodynamic heating to corrugation-stiffened structures in thick, turbulent boundary-layers, Brandon et al (ref. 20) found that, although the highest peak heating occurred when the corrugations were perpendicular to the flow, it was not much less when the corrugations were inclined to the free-stream by as little as 15° .

Note that the heat-transfer rates measured at the thermocouples just upstream of the separation surface decrease continuously as the flow proceeds toward the gap and are consistently below the flat-plate values. Thus, the C5 measurements from this region differ from the C2 results where the heat-transfer increased slightly as the flow approached the gap and then decreased rapidly around the corner of the separation step (see Fig. 8 and the discussion of the data presented therein). The heating increase for the upstream surface of the C2 was attributed to the pressure rise created by the impingement process propagating through the relatively thick subsonic portion of the shear layer. Unless the thermocouples for the C5 are spaced such that all the local peaks were missed (which seems unlikely), the C5 data indicate that the cross flow associated with a skewed gap provided an alternative path for the oncoming flow and minimized the upstream effects of the impingement process.

The heating-rate distributions obtained at a Reynolds number of 4.01×10^6 are presented in Fig. 32. The flat-plate heat-transfer rates, which are presented for reference, indicate that the unperturbed boundary-layer was laminar for the entire region. Again, locally high heating rates are measured for the thermocouples at and just downstream of the upper tangency point of the recompression surface. This trend is similar to that observed at the lower Reynolds number. Note also that the heating rates measured by those thermocouples of section BB downstream of the gap are significantly above the flat-plate values at all points. The relative increase is even more significant since the C5 data for this run are usually lower than the corresponding flat-plate values. (This reflects the run-to-run variations discussed earlier.)

Note that the BB section not only contains the most-downstream thermocouples, but it is downstream of the AA section gap. Thus, the data indicate the two diagonal gaps promote transition at this Reynolds number. Recall that, for this Reynolds number, the flat-plate transition location was at $0.75L$.

That these relatively narrow, oblique gaps promote the transition is also indicated by the heat-transfer rates measured at $Re_{\infty,L} = 5.90 \times 10^6$ and 8.11×10^6 . Heating rate data from the CC section (Figs. 33a and 34a) and from the BB, the DD, and the FF sections (Figs. 33b and 34b) indicate the premature onset of transition.

CONCLUDING REMARKS

Heat-transfer distributions were measured in the vicinity of gap inserts located in a flat-plate structural carrier. The data were obtained in the 3.5-Foot Hypersonic Wind Tunnel at the Ames Research Center at a Mach number of 5.1 over a Reynolds number range of 2.57×10^6 to 8.11×10^6 . Because of significant differences in the configuration geometries, the correlations developed by previous investigators did not work with the present data. Furthermore, because of the experimental uncertainties, it was not possible to develop general correlations incorporating local boundary-layer parameters using only the present data. However, for the range of conditions studied several trends were clearly evident.

1. The narrow transverse gaps of the present configurations had relatively little effect on the laminar boundary layer. This is true for the multiple-gap configuration (C3) as well as for the single-gap configuration (C2). The local heating increases were relatively small and the transition location changed only slightly.

When the boundary-layer was transitional, locally high heating rates were measured near the upper tangency point of the recompression surface once the gap width exceeded a minimum value. The perturbed heating increased as z^* decreased and as w/d increased, i.e., when $(\frac{x_s}{z^*})(\frac{w}{d})^{0.2}$ is greater than 500 (approximately). However, none of the measured heat-transfer rates exceeded the values calculated for a fully turbulent boundary layer. The local heating increases become more severe for configurations having both a gap and vertically-misaligned adjacent surfaces.

2. For the C4 configuration whose intersecting gaps are aligned either parallel or perpendicular to the free-stream locally high heating rates were measured along the length of the longitudinal slot and at the recom-

pression surface at the "T" formed by the intersection of the longitudinal slot and the transverse gap. The heating-rate ratio at points along the longitudinal slot increased with the unit Reynolds number, with the distance from the separation step ($x-x_0$), and with the depth of the slot.

The extremely high heating rates were measured on the recompression surface downstream of the T-gap. The heating rates increased with the z-dimension of the recompression step, d. Furthermore, at the highest Reynolds number, the heating rates to the flat surface downstream of the T-gap exceeded the theoretical values for the flat-plate boundary layer which is turbulent from the leading edge.

3. For the configuration with intersecting gaps, where the gaps are swept either 30° or 60° , i.e., the C5 configuration, the heating rates were only slightly affected by the presence of the gaps. The swept gaps did promote transition at the higher Reynolds number.

REFERENCES

1. T.F. Foster, W.K. Lockman, and W.J. Grifall, "Thermal Protection System Gap Heating Rates of the Rockwell International Flat Plate Heat Transfer Model (OH2A/OH2B)", NASA CR-134,077, Nov. 1973, Data Management Services, Chrysler Corporation Space Division.
2. J.J. Bertin, D.R. Neal, and D.D. Stalmach, "The Effect of the Transport Property Models on the Shuttle Boundary Layer", Aerospace Engineering Report 78002, June 1978, The University of Texas at Austin.
3. D.D. Stalmach and J.J. Bertin, "The Analysis of a Nonsimilar Laminar Boundary Layer", Aerospace Engineering Report 78001, Feb. 1978, The University of Texas at Austin.
4. H. Tong, A.C. Buckingham, and H.L. Morse, "Nonequilibrium Chemistry Boundary Layer Integral Matrix Procedure", Aerotherm Final Report No. 73-67, July 1973, The Acurex Corporation.
5. P. F. Brinich and N. Sands, "Effect of Bluntness on Transition for a Cone and Hollow Cylinder at Mach 3.1". TN 3979, May 1957, NACA.
6. P.E. Everhart and H.H. Hamilton, "Experimental Investigation of Boundary-Layer Transition on a Cooled 7.5 Total-Angle Cone at Mach 10". TN D-4188, Oct. 1957, NASA.
7. J.L. Potter and J.D. Whitfield, "Boundary Layer Transition Under Hypersonic Conditions". AGARDograph 97, 1965.
8. J.D. Whitfield and F.A. Iannuzzi, "Experiments on Roughness Effects on Cone Boundary-Layer Transition Up to Mach 16", AIAA Journal, Vol. 7, No. 3, March 1969, pp. 465-470.
9. R.V. Masek and J.A. Forney, "An Analysis of Predicted Space Shuttle Temperatures and Their Impact on Thermal Protection Systems", a paper in TMX-2272, April 1971, NASA.
10. B.K. Hodge and J.C. Adams, "The Calculation of Compressible Transitional, Turbulent, and Relaminarizational Boundary Layers over Smooth and Rough Surfaces Using an Extended Mixing-Length Hypothesis", AEDC-TR-77-96, Feb. 1978, AEDC.

11. A.F. Charwat, J.N. Roos, C.F. Dewey, Jr., and J.A. Hitz, "An Investigation of Separated Flows - Part I: The Pressure Field", Journal of the Aerospace Sciences, Vol. 28, No. 6, June 1961, pp. 457-470.
12. A.F. Charwat, C.F. Dewey, Jr., J.N. Roos, and J.A. Hitz, "An Investigation of Separated Flows - Part II: Flow in the Cavity and Heat Transfer", Journal of the Aerospace Sciences, Vol. 28, No. 7, July 1961, pp. 513-527.
13. J.C. Dunavant and D.A. Throckmorton, "Aerodynamic Heat Transfer to RSI Tile Surfaces and Gap Intersections", Journal of Spacecraft and Rockets, Vol. 11, No. 6, June 1974, pp. 473-440.
14. D.E. Avery, "Aerodynamic Heating in Gaps of Thermal Protection System Tile Arrays in Laminar and Turbulent Boundary Layers", Technical Paper 1187, July 1978, NASA.
15. H.L. Bohon, J.W. Sawyer, L.R. Hunt, and J. Weinstein, "Performance of Thermal Systems in a Mach 7 Environment", Journal of Spacecraft and Rockets, Vol. 12, No. 12, Dec. 1975, pp. 744-749.
16. D. E. Nestler, "An Engineering Analysis of Reattaching Shear Layer Heat Transfer", AIAA Paper 72-717, presented at the 5th Fluid and Plasma Dynamics Conference, Boston, June 1972.
17. R. A. Brewer, A. R. Saydah, D. E. Nestler, and D. E. Florence, "Thermal Performance Evaluation of RSI Panel Gaps for Space Shuttle Orbiter", Journal of Spacecraft and Rockets, Vol. 10, No. 1, Jan. 1973, pp. 23-28.
18. A.F. Charwat, "Supersonic Flows with Imbedded Separated Regions" from Advances in Heat Transfer, Vol. 6, pp. 1 - 132, Academic Press, 1970, New York.
19. C.B. Johnson, "Heat Transfer Data to Cavities Between Simulated RSI Tiles at Mach 8", CR 128, 770, June 1973, NASA.
20. H.J. Brandon, R.V. Masek, and J.C. Dunavant, "Aerodynamic Heating to Corrugation Stiffened Structures in Thick Turbulent Boundary Layers", AIAA Journal, Vol. 13, No. 11, Nov. 1975, pp. 1460-1466.

Table 1. Variations in the exact flow conditions
for a nominal test condition

	p_{t1} (atm)	T_t (°K)	T_w (°K)	$Re_{\infty,L} \times 10^{-6}$ P.G. ¹	R.G. ²	Tab. ³
Run 38,AA	4.58	1127.2	303.5	2.5719	2.3823	2.2110
Run 38,BB	4.58	1127.2	303.5	2.5719	2.3823	2.2110
Run 38,CC	4.58	1148.9	303.5	2.5053	2.3051	2.1412
Run 6, BB	4.46	1159.7	303.5	2.4078	2.2074	2.0518
Run 39,BB	8.06	1231.1	309.8	4.0129	3.9319	3.3515
Run 40,BB	11.43	1198.9	312.7	5.8952	5.3230	4.9693
Run 41,AA	15.29	1175.3	315.3	8.1056	7.3963	6.8760
Run 41,BB	15.29	1175.3	315.3	8.1056	7.3963	6.8760
Run 41,CC	15.29	1202.2	315.3	7.8589	7.0981	6.6165
Run 9, BB	15.30	1170.4	315.3	8.1583	7.4577	6.9310

1. Calculated using p_{t1} , T_t , $p_e = 1.683 \times 10^{-3} p_{t1}$, and the perfect-gas equations.
2. Calculated using p_{t1} , T_t , $p_e = 1.683 \times 10^{-3} p_{t1}$, and the real-gas correlations.
3. Tabulated in ref. 1

Table 2. - Transition for the flat-plate configuration, C1

(a) Transition locations

	$\frac{y}{L}$	$\frac{x_{tr}}{L}$
Run 39,AA	+0.135	0.80
Run 39,BB	0.000	0.74
Run 39,CC	-0.135	0.72
Nominal for Run 39		0.75
Run 40,AA	+0.135	0.59
Run 40,BB	0.000	0.56
Run 40,CC	-0.135	0.50
Nominal for Run 40		0.55
Run 41,AA	+0.135	0.55
Run 41,BB	0.000	0.54
Run 41,CC	-0.135	0.47
Nominal for Run 41		0.52

(b) Transition parameters calculated using the nominal transition locations

	Perfect-gas model			Real-gas model		
	Re/m ($\times 10^{-6}$)	Re _{x,tr} ($\times 10^{-6}$)	$(\frac{Re_{\theta}}{Me})_{tr}$	Re/m ($\times 10^{-6}$)	Re _{x,tr} ($\times 10^{-6}$)	$(\frac{Re_{\theta}}{Me})_{tr}$
Run 39	2.633	3.010	206.22	2.345	2.681	196.60
Run 40	3.868	3.242	213.88	3.493	2.928	204.74
Run 41	5.319	4.215	247.71	4.853	3.846	233.97

Table 3. - The gap geometries for Configuration 2 (C2)

(a) Length-to-height ratio, w/d

	AA	BB	CC
	$y = +0.135L$ $d = 1.016 \text{ cm}$	$y = +0.000L$ $d = 2.032 \text{ cm}$	$y = -0.135L$ $d = 4.064 \text{ cm}$
$w(\text{cm})$	$\frac{w}{d}$	$\frac{w}{d}$	$\frac{w}{d}$
0.127	0.125	0.063	0.031
0.254	0.250	0.125	0.063
0.508	0.500	0.250	0.125

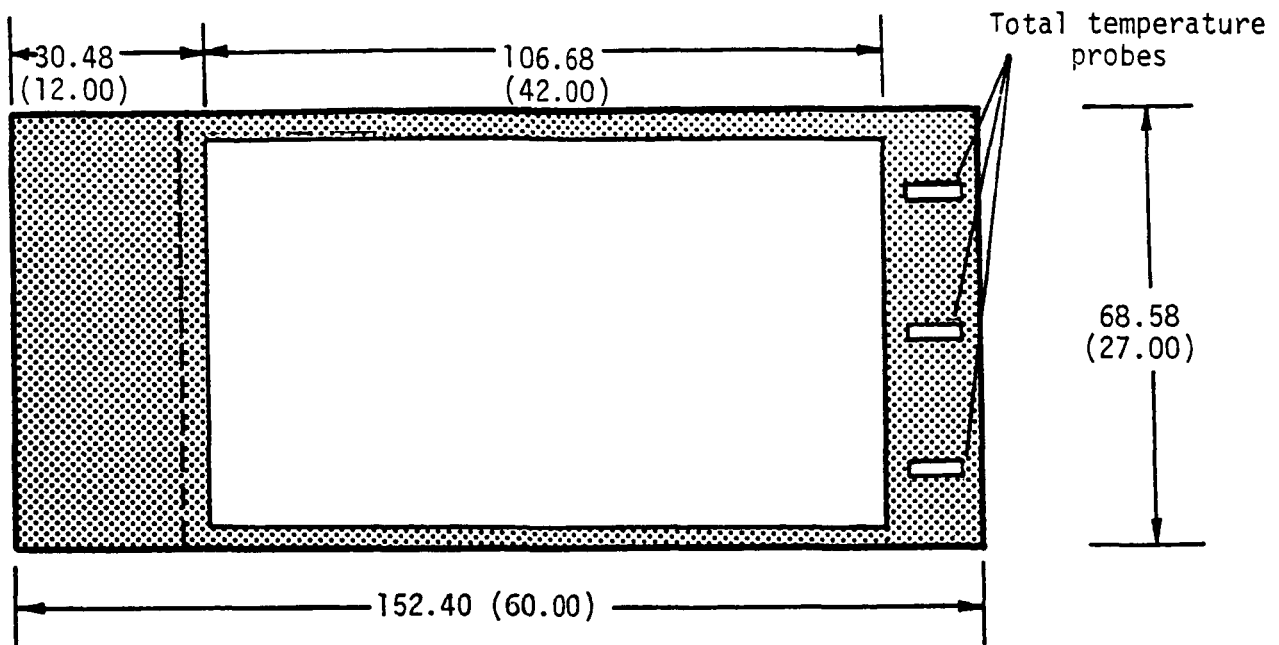
(b) The boundary-layer displacement thickness at
 $x = 0.6L$ relative to the gap width.

Re_x (at $x=91.44 \text{ cm}$)	$w = 0.127 \text{ cm}$ $\frac{\delta^*}{w}$	$w = 0.254 \text{ cm}$ $\frac{\delta^*}{w}$	$w = 0.508 \text{ cm}$ $\frac{\delta^*}{w}$
1.543×10^6	3.218	1.609	0.805
2.408×10^6	2.484	1.242	0.621
3.537×10^6 (lam)	2.088	1.044	0.522
3.537×10^6 (tr)	2.095	1.048	0.524
4.863×10^6 (lam)	1.807	0.904	0.452
4.863×10^6 (tr)	2.153	1.076	0.538

Table 3. - Concluded

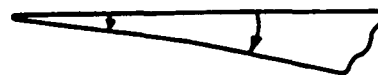
(c) The z-coordinate of the sonic point at $x = 0.6L$
relative to the gap width

Re_x (at $x=91.44$ cm)	$w = 0.127$ cm	$w = 0.254$ cm	$w = 0.508$ cm
	$\frac{z^*}{w}$	$\frac{z^*}{w}$	$\frac{z^*}{w}$
1.543×10^6	1.008	0.504	0.252
2.408×10^6	0.756	0.378	0.189
3.537×10^6 (lam)	0.644	0.322	0.161
3.537×10^6 (tr)	0.652	0.326	0.163
4.863×10^6 (lam)	0.564	0.282	0.141
4.863×10^6 (tr)	0.134	0.067	0.033



10°

Note: Dimensions in cm(in)



5° 10°
Leading edge

Figure 1. - Sketch of structural carrier-plate.

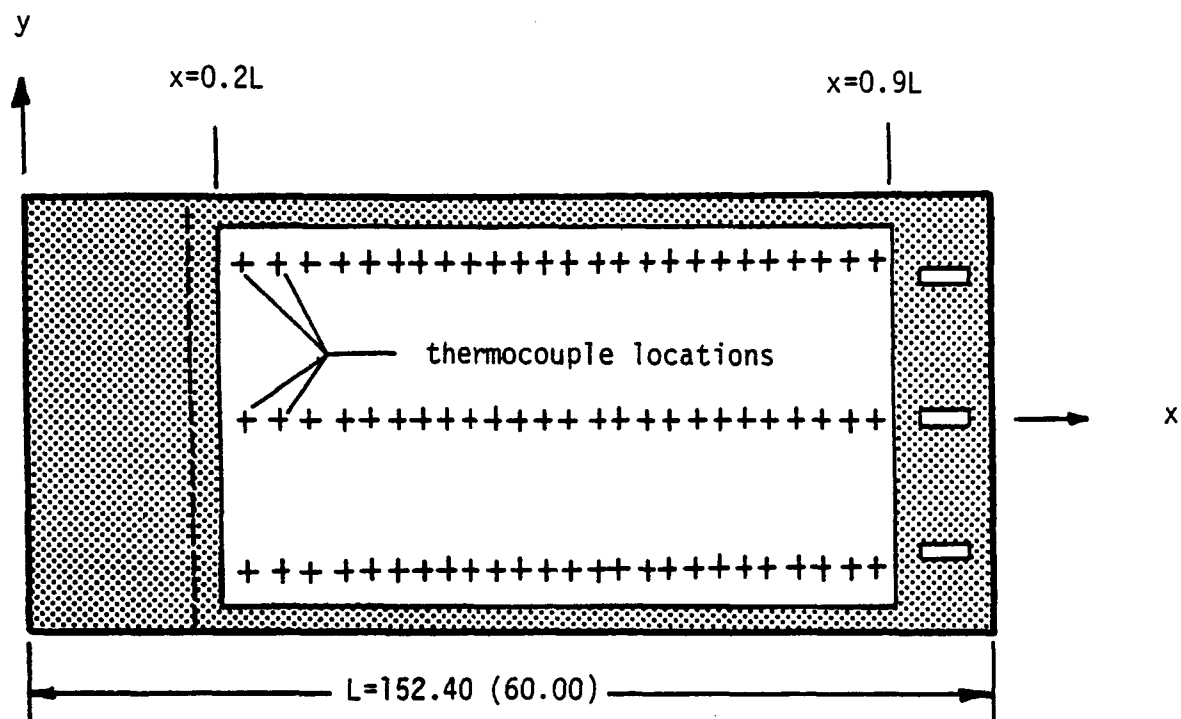
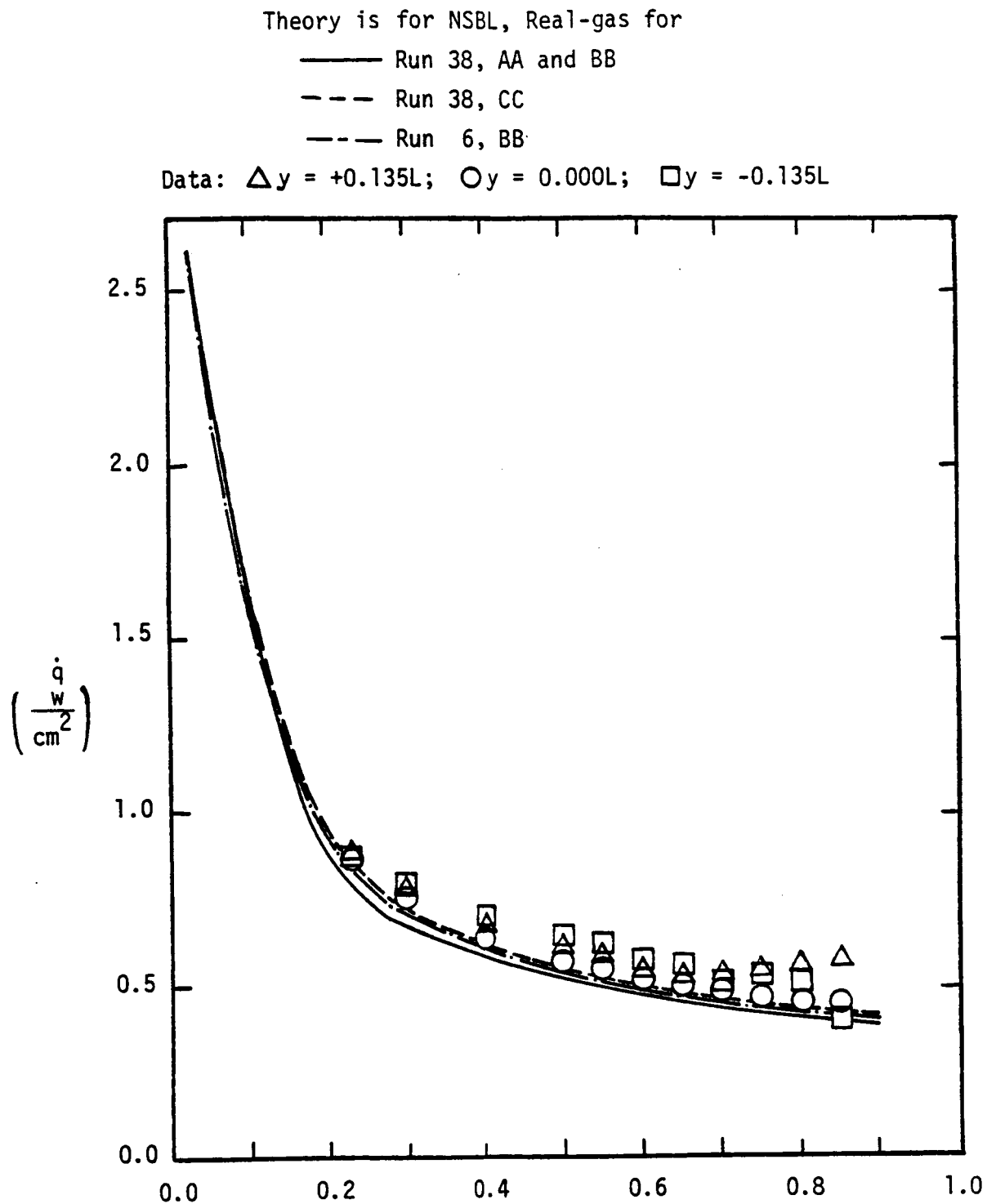


Figure 2. Sketch of flat-plate insert in the structural carrier-plate to form Configuration 1 (C1).



(a) $Re_{\infty,L} = 2.57 \times 10^6$

Figure 3. - The effect of the free-stream conditions on the heat-transfer distribution along the flat plate (Configuration 1)

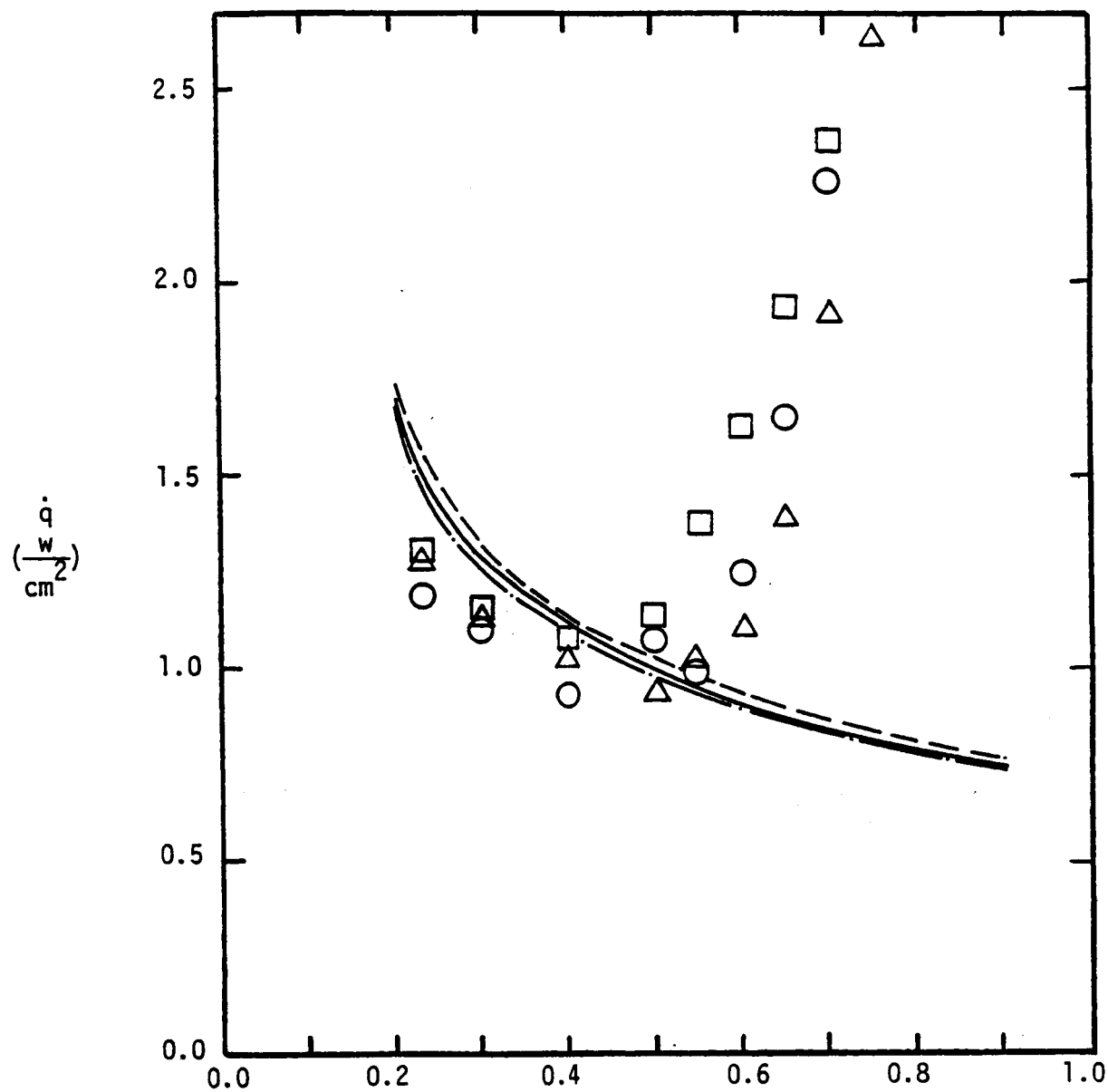
Theory is for NSBL, Real-gas for

— Run 41, AA and BB

--- Run 41, CC

--- Run 9, BB

Data: $\Delta y = +0.135L$; $\circ y = 0.000L$; $\square y = -0.135L$



(b) $Re_{\infty,L} = 8.11 \times 10^6$

Figure 3. - Concluded.

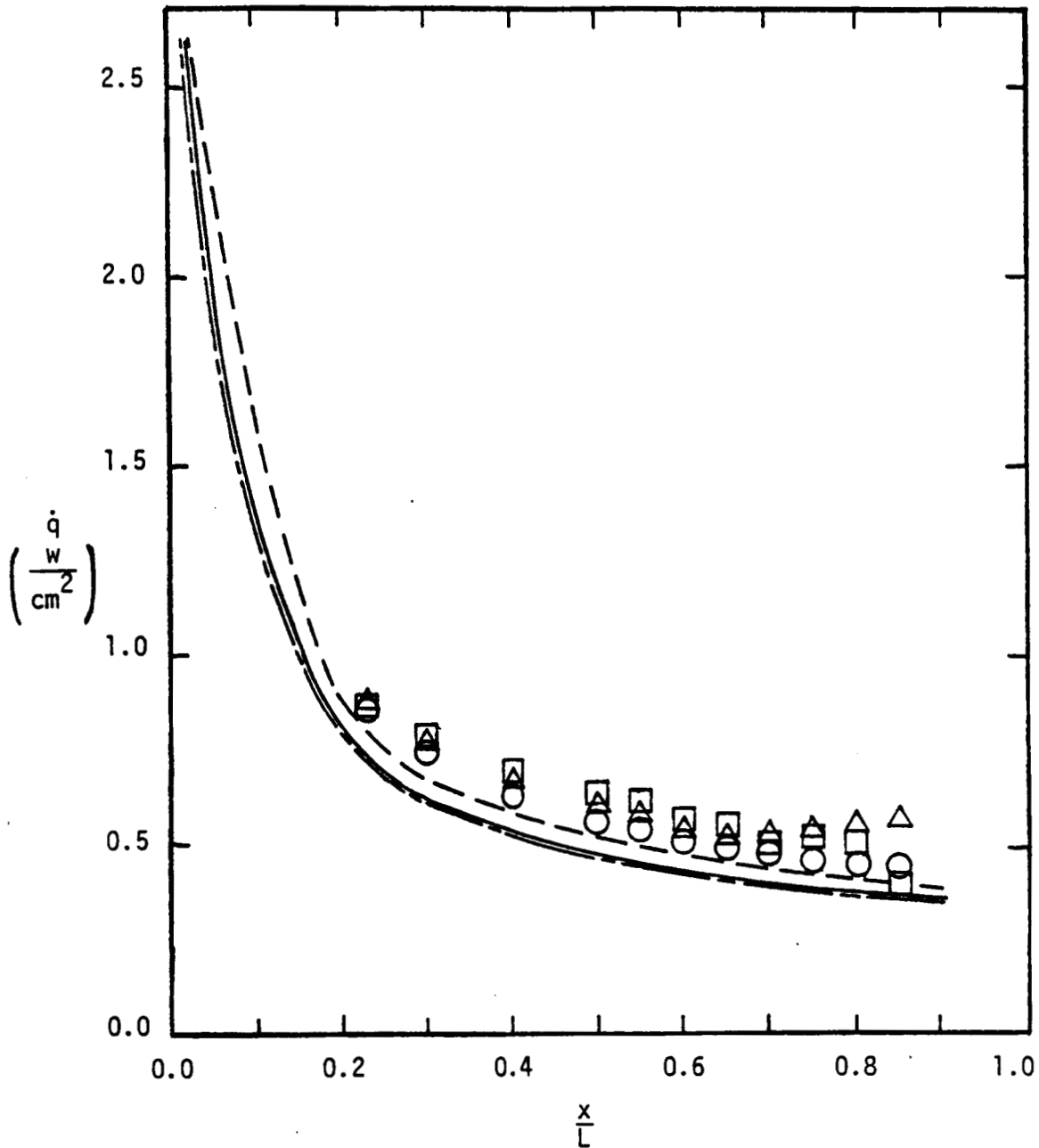
Theory is for Run 38,BB using

— NSBL, Perfect-gas

--- NSBL, Real-gas

--- BLIMP, Perfect-gas

Data: $\Delta y = +0.135L$; $\circ y = 0.000L$; $\square y = -0.135L$



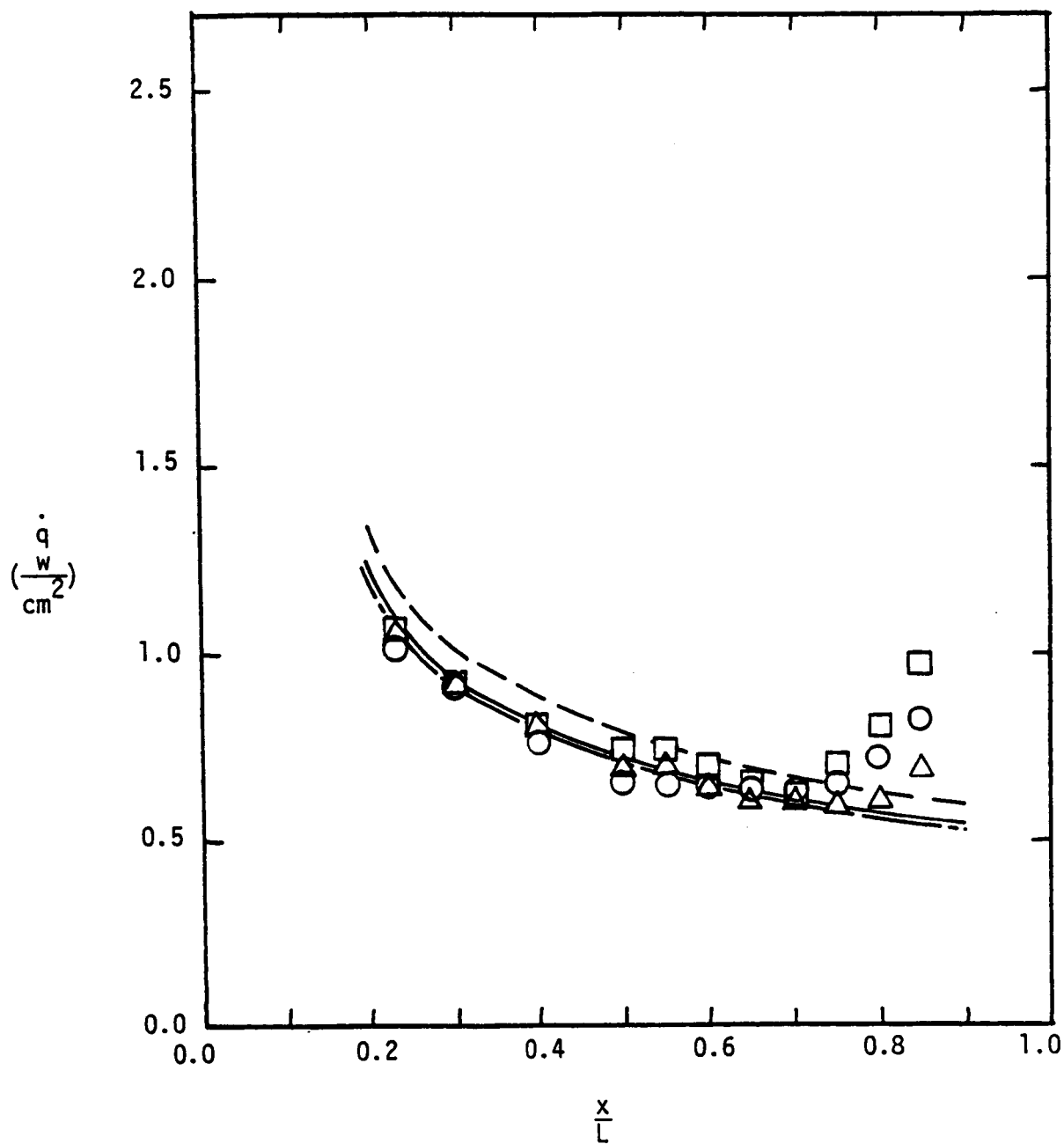
(a) $Re_{\infty,L} = 2.57 \times 10^6$

Figure 4. - The effect of the flow model on the heat-transfer distribution along the flat plate (Configuration 1)

Theory is for Run 39,BB using

— NSBL, Perfect-gas
--- NSBL, Real-gas
--- BLIMP, Perfect-gas

Data: $\Delta y = +0.135L$; $\circ y = 0.000L$; $\square y = -0.135L$



(b) $Re_{\infty,L} = 4.01 \times 10^6$

Figure 4. - Continued.

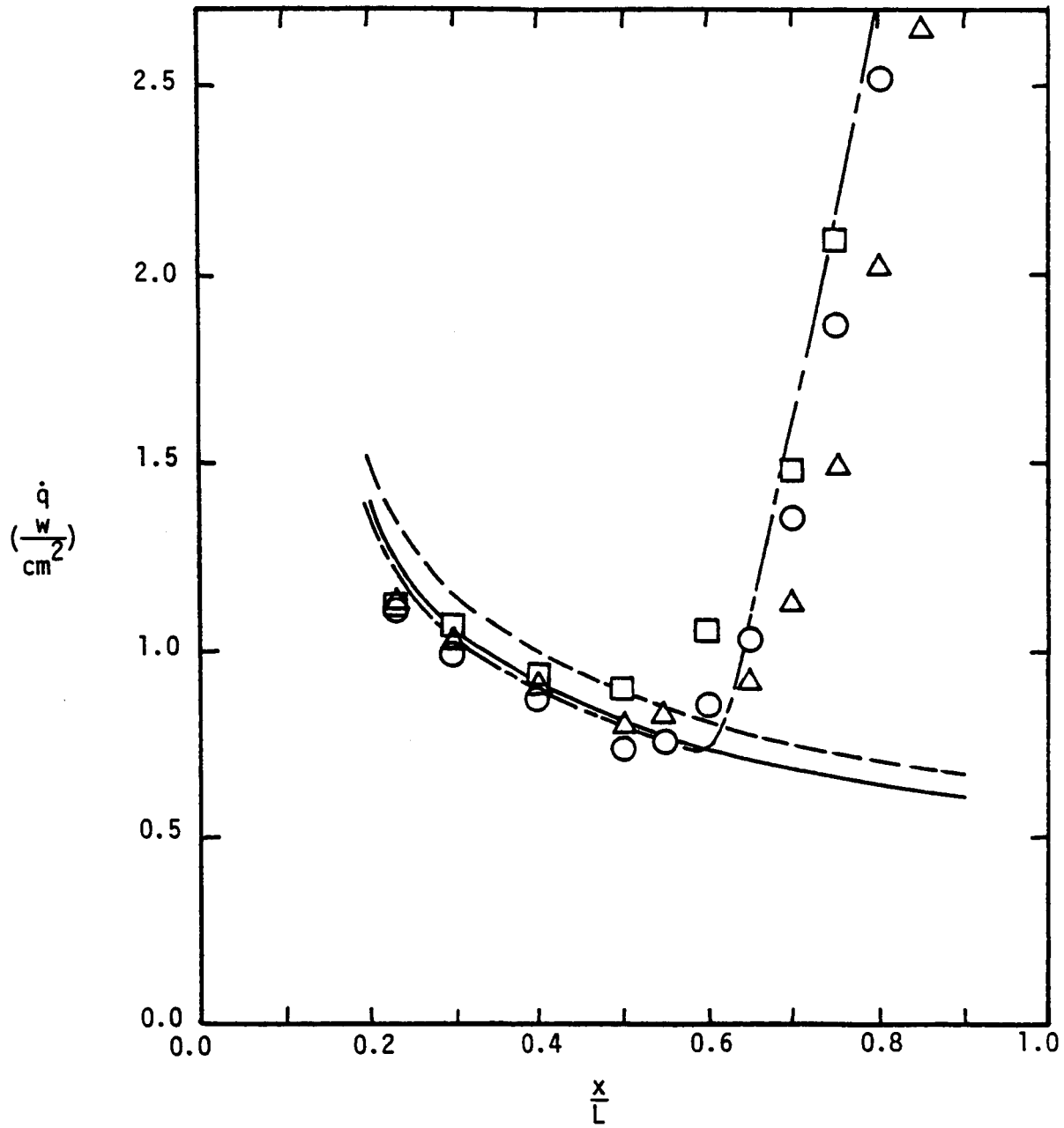
Theory is for Run 40,BB using

— NSBL, Perfect-gas

- - - NSBL, Real-gas

- - - BLIMP, Perfect-gas, $(Re_\theta/M_e)_{tr} = 222.55$

Data: $\Delta y = +0.135L$; $\bigcirc y = 0.000L$; $\square y = -0.135L$



(c) $Re_{\infty,L} = 5.90 \times 10^6$

Figure 4 . - Continued.

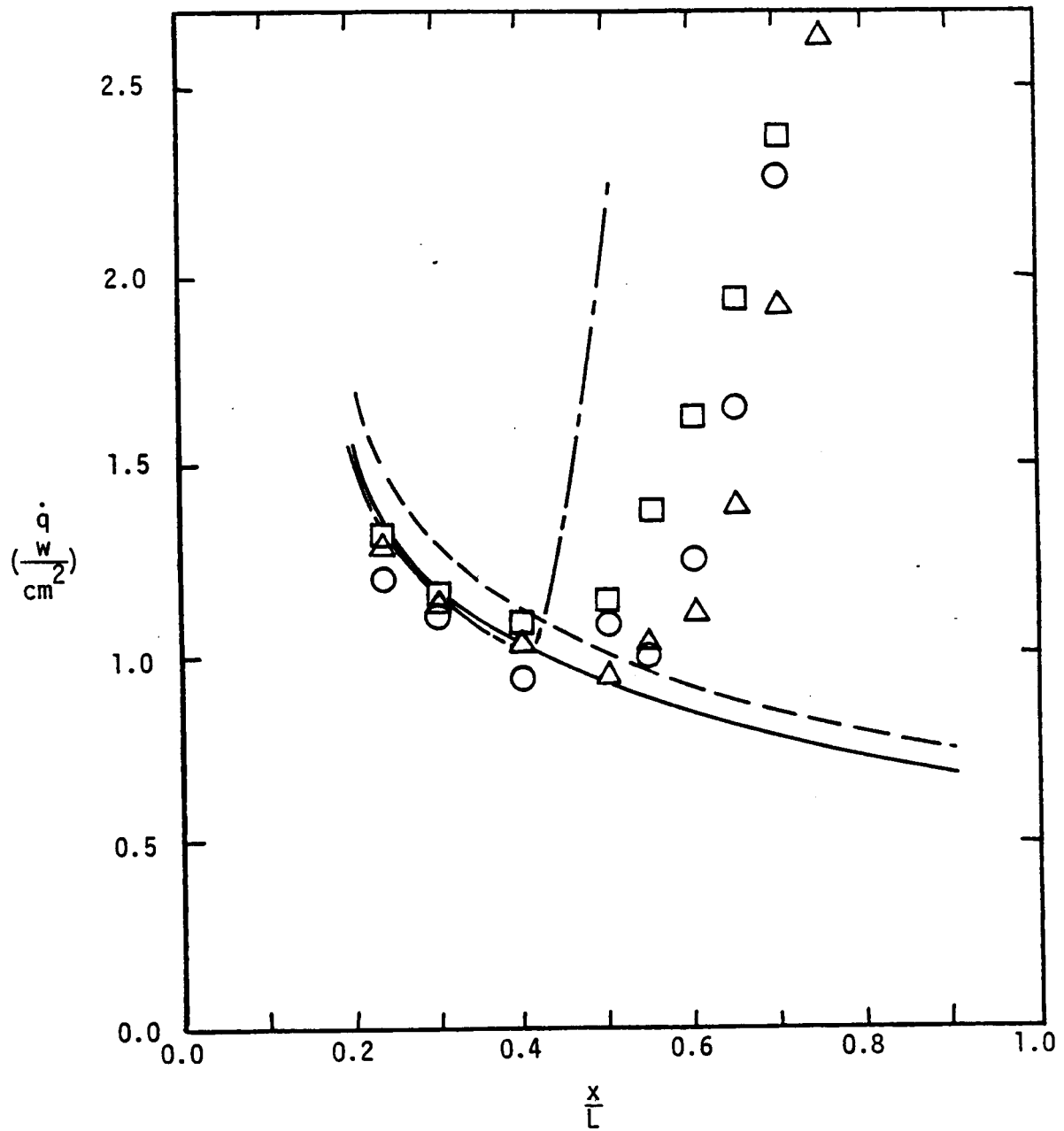
Theory is for Run 41,BB using

— NSBL, Perfect-gas

--- NSBL, Real-gas

- - - BLIMP, Perfect-gas, $(Re_\theta/M_e)_{tr} = 222.55$

Data: $\Delta y = +0.135L$; $\circ y = 0.000L$; $\square y = -0.135L$



(d) $Re_{\infty,L} = 8.11 \times 10^6$

Figure 4. - Concluded

The transition Reynolds numbers calculated using the heat-transfer distribution and

○ Perfect-gas properties

□ Real-gas properties

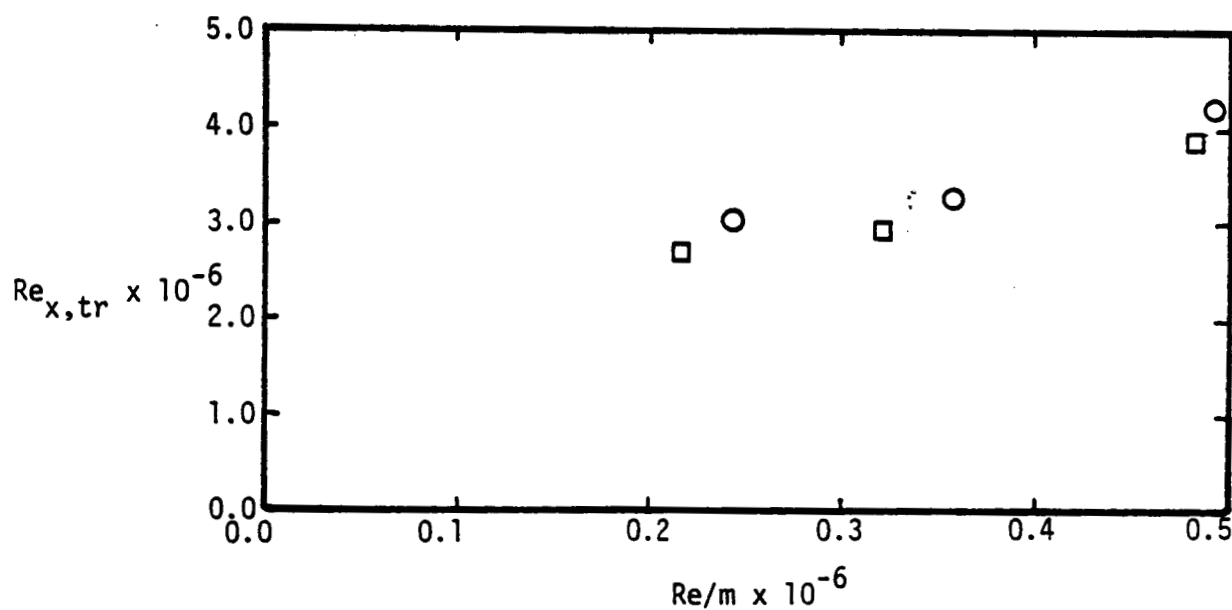
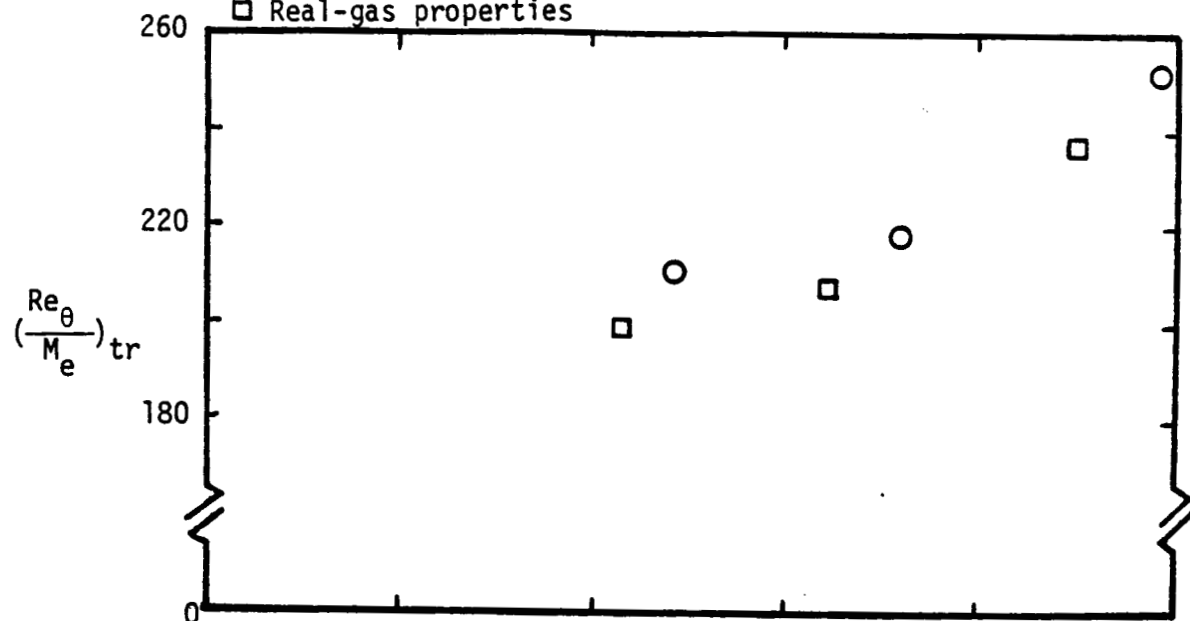


Figure 5. - The transition Reynolds number for the flat plate (C1) as a function of the unit Reynolds number. $M_e = 5.1$

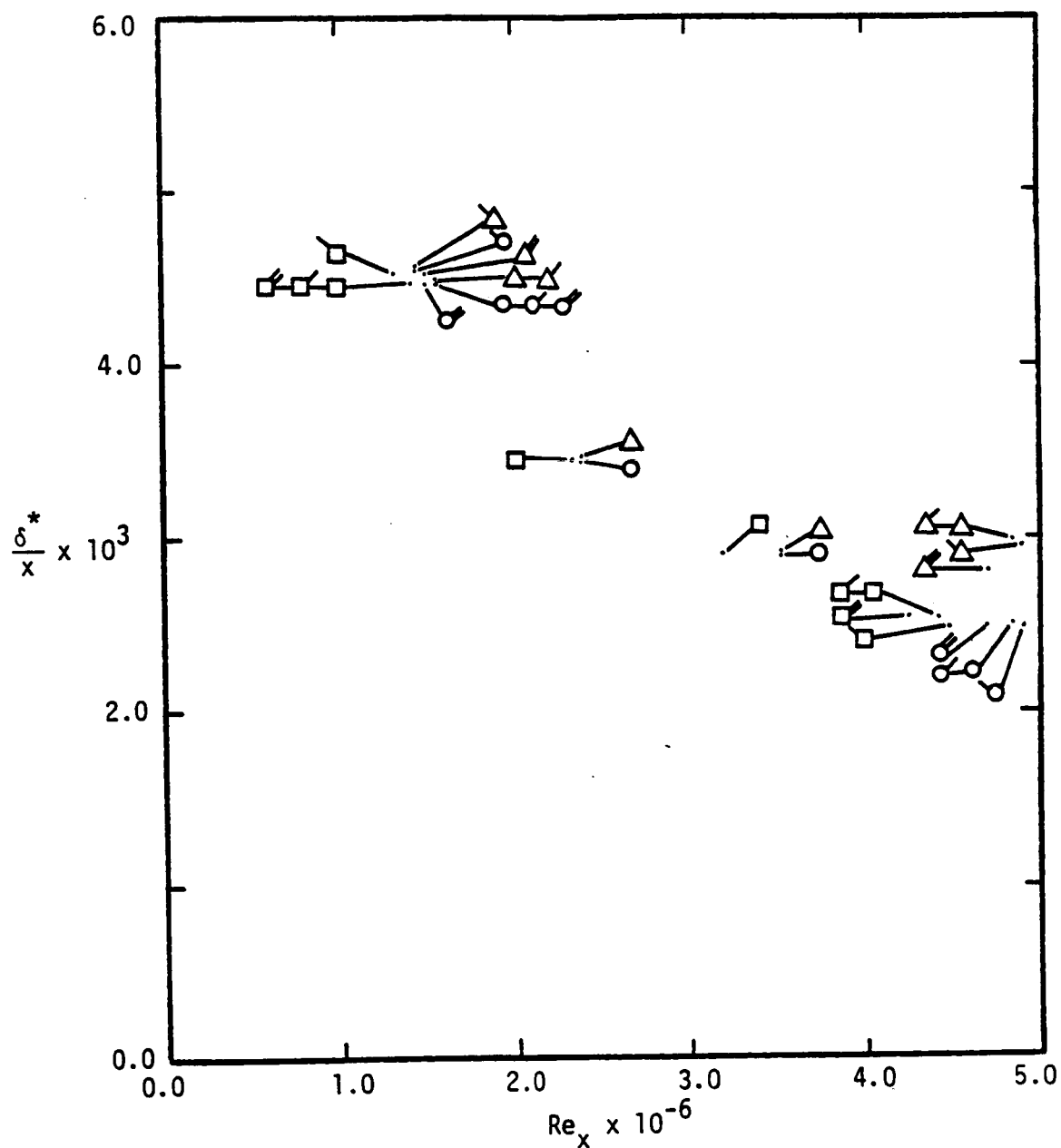
○ NSBL, Perfect-gas

□ NSBL, Real-gas

△ BLIMP, Perfect-gas, $(Re_e/M_e)_{tr} = 222.55$

No flag: $y = 0.000L$; /: $y = 0.135L$; \/: $y = -0.135L$

⋈: Repeat-run flow conditions



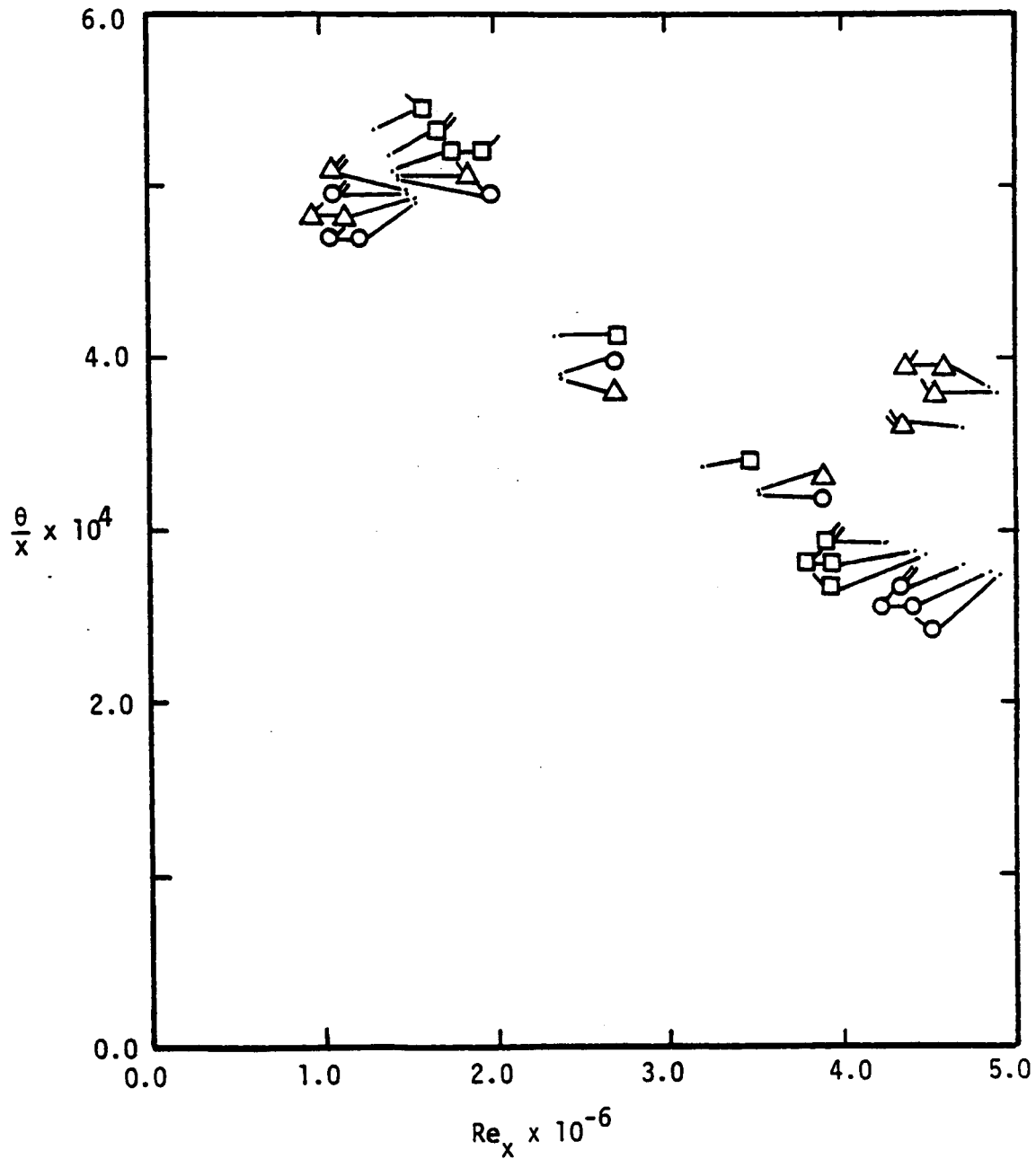
(a) Displacement thickness

Figure 6. - Theoretical values of the correlation parameters evaluated at $x = 0.6L$.

- NSBL, Perfect-gas
- NSBL, Real-gas
- △ BLIMP, Perfect-gas, $(Re_\theta / M_e)_{tr} = 222.55$

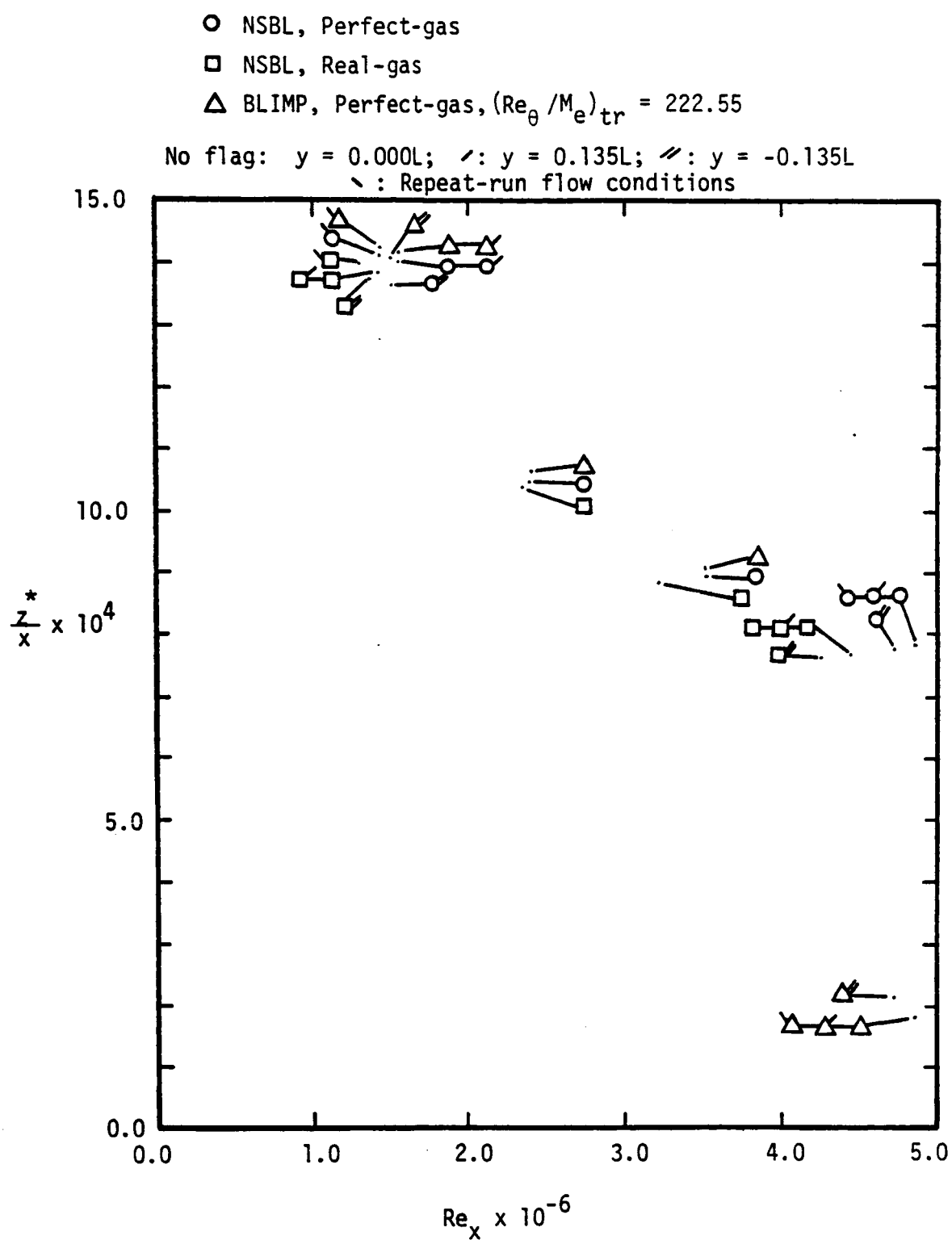
No flag: $y = 0.000L$; /: $y = 0.135L$; //: $y = -0.135L$

\: Repeat-run flow conditions



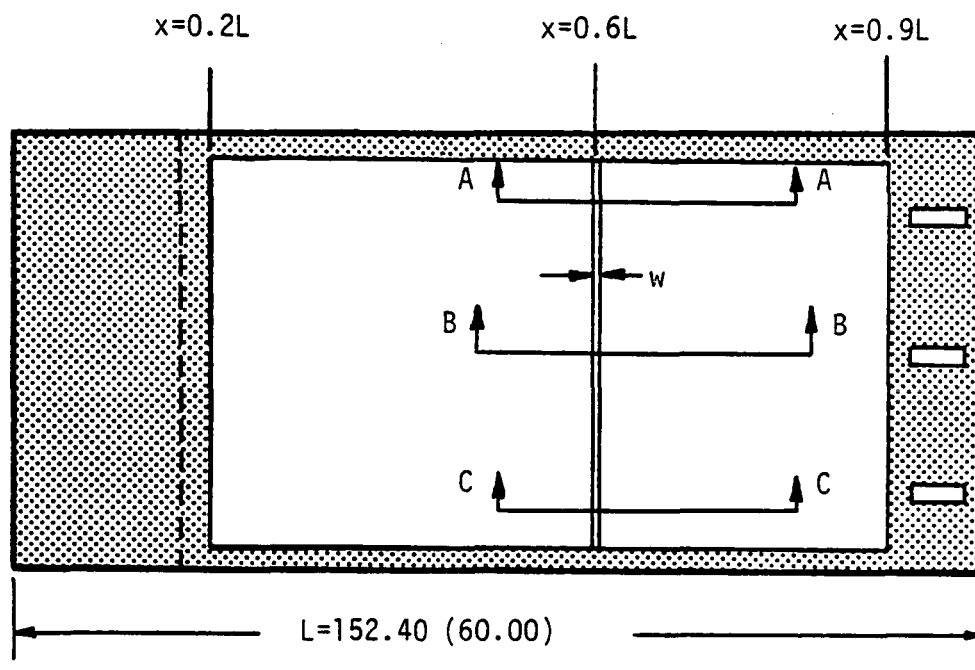
(b) Momentum thickness

Figure 6. - Continued.



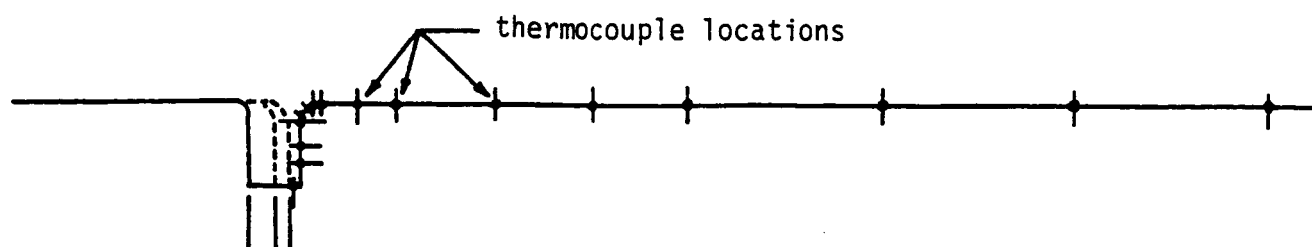
(c) Sonic point

Figure 6.- Concluded.



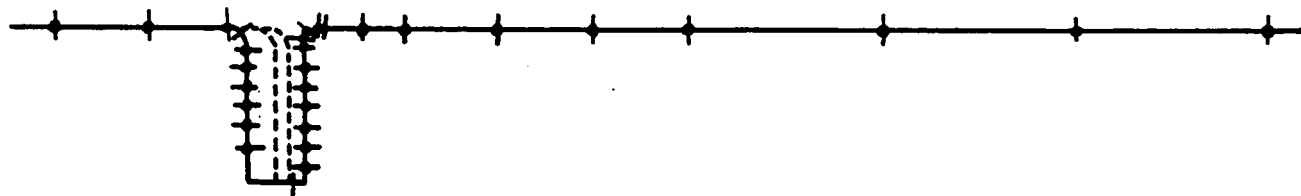
(a) Sketch of entire configuration

Figure 7. Sketch of the single-transverse-gap insert placed in the structural carrier-plate to form Configuration 2 (C2).

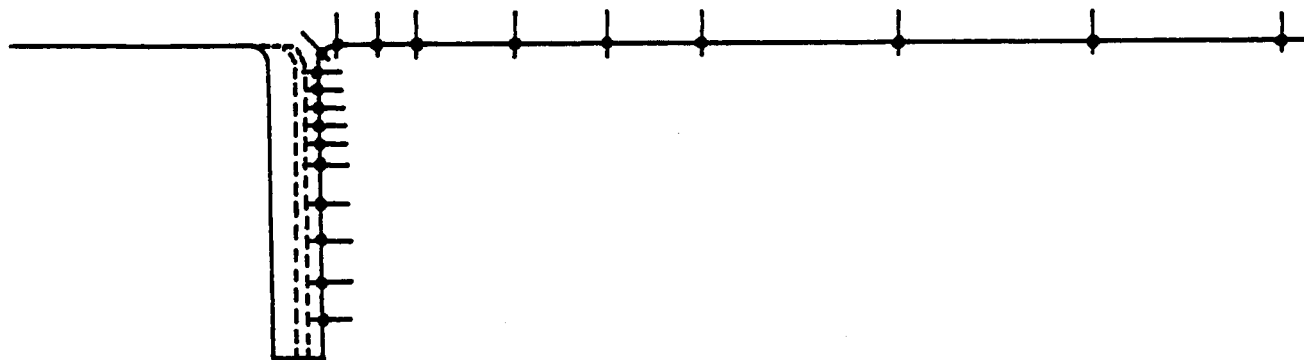


$x = 0.6L$ for the various gap widths

(b) Section AA, $d = 1.016$ cm, $y = +0.135L$



(c) Section BB, $d = 2.032$ cm, $y = 0.000L$



(d) Section CC, $d = 4.064$ cm, $y = -0.135L$

Figure 7. - Concluded

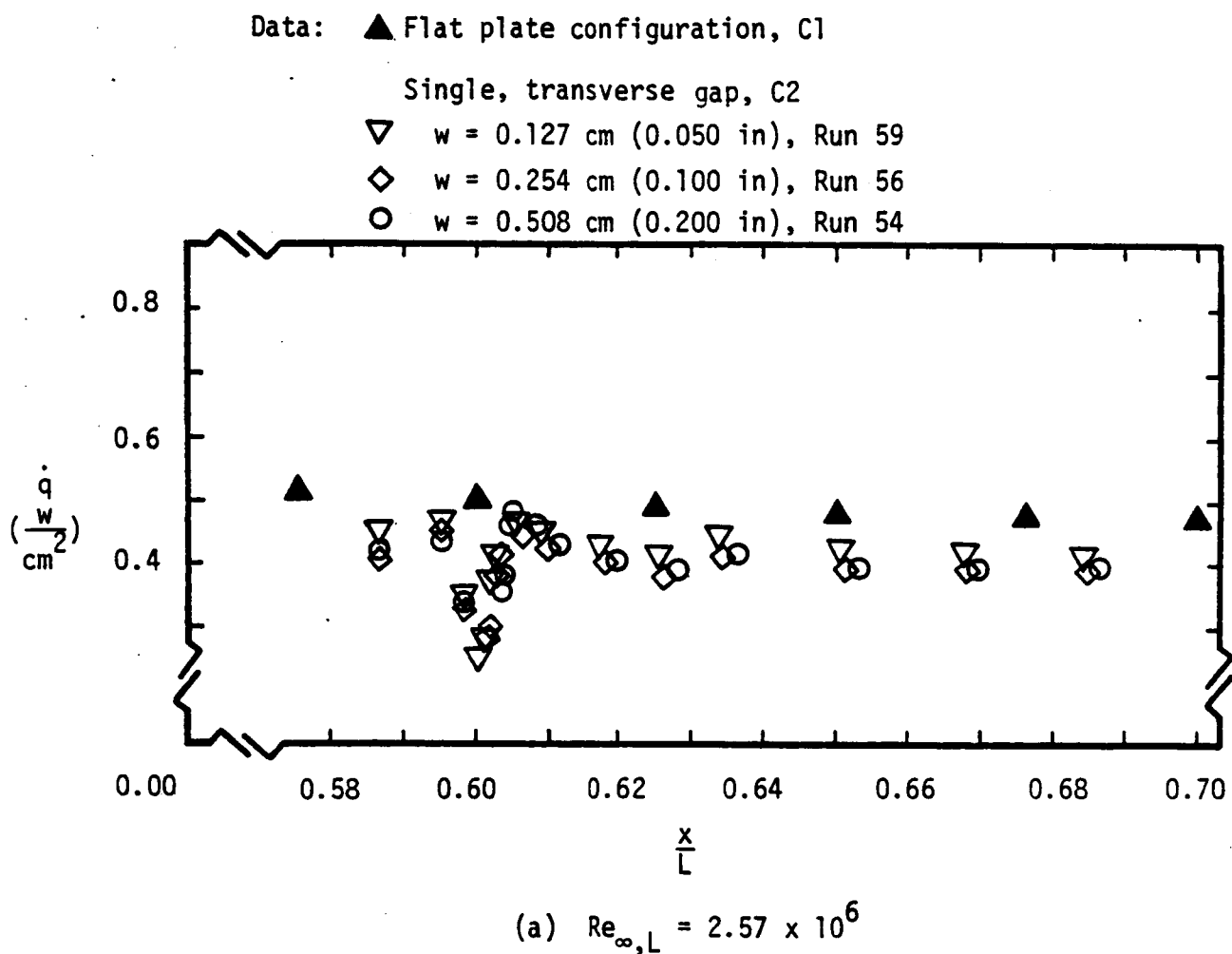
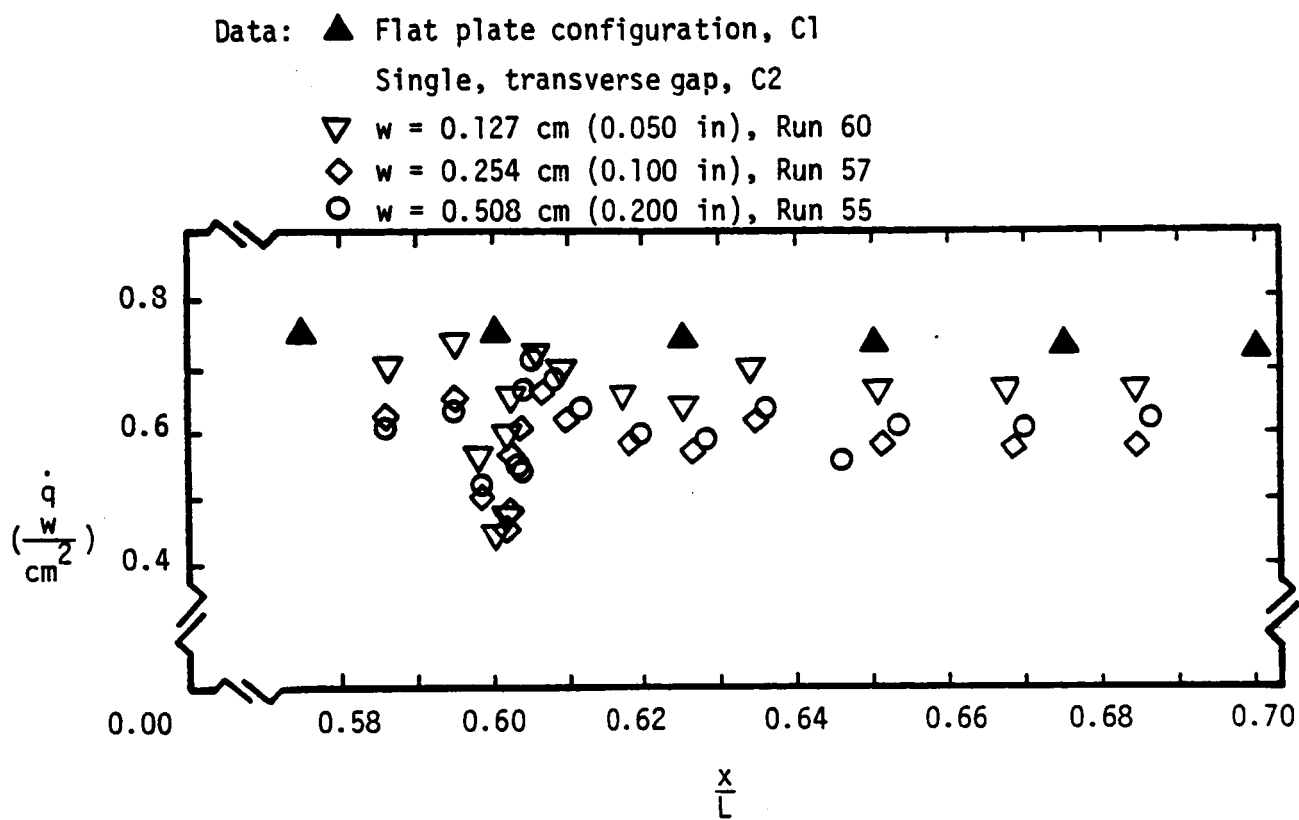


Figure 8. - The heating distribution upstream and downstream of a single, transverse gap in a laminar boundary layer. Data for $y = 0.000L$ (section BB)



(b) $Re_{\infty, L} = 4.10 \times 10^6$

Figure 8. - Concluded.

— NSBL, Perfect-gas solution for Run 38,BB

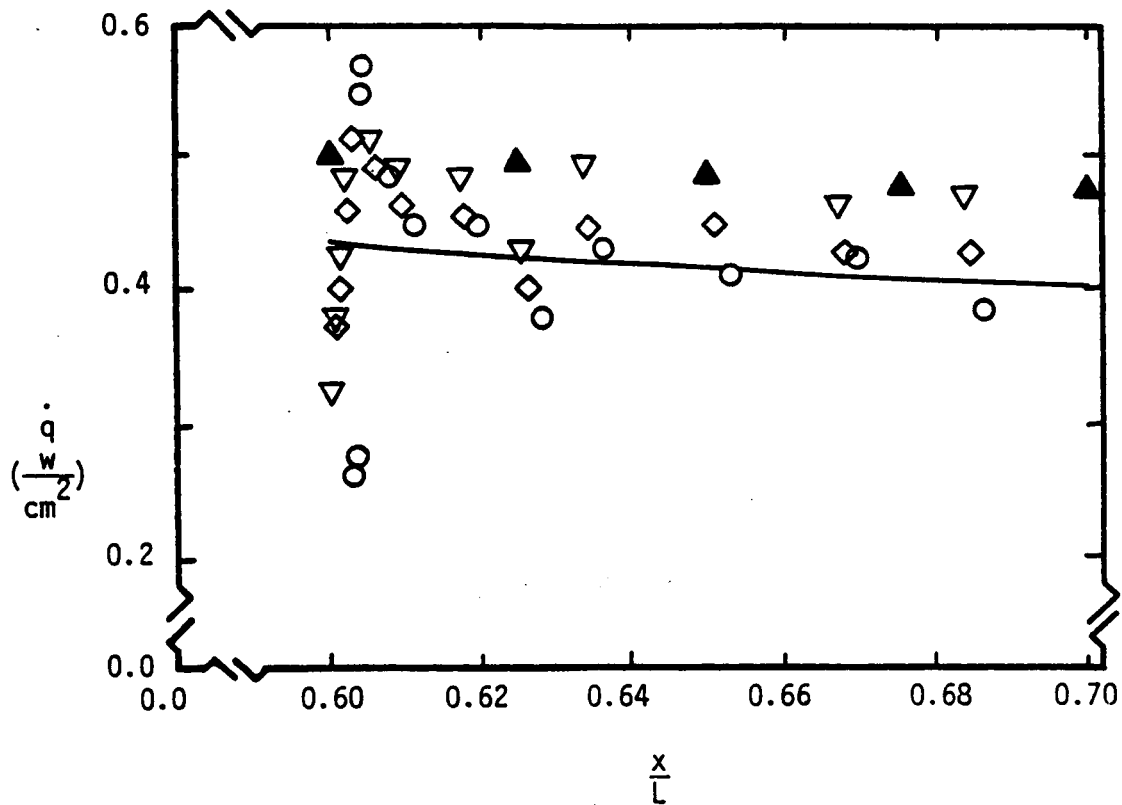
Data:▲ Flat plate configuration C1

Single, transverse gap, C2

▽ w = 0.127 cm (0.050 in)

◇ w = 0.254 cm (0.100 in)

○ w = 0.508 cm (0.200 in)



(a) $Re_{\infty,L} = 2.57 \times 10^6$

Figure 9. - Comparison of the heat-transfer distribution for flat plate with those downstream of a single, transverse gap. Data for $y=0.000L$ (section BB).

— NSBL, Perfect-gas solution for Run 39,BB

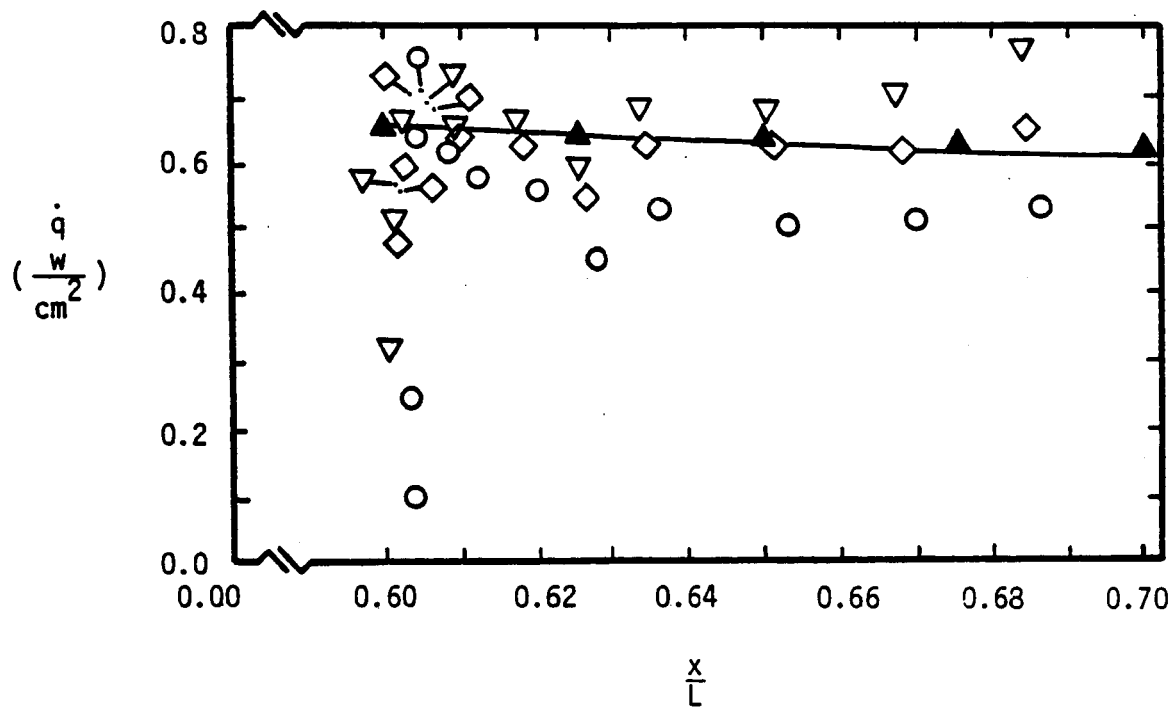
Data: ▲ Flat plate configuration C1

Single, transverse gap, C2

▽ w = 0.127 cm (0.050 in)

◇ w = 0.254 cm (0.100 in)

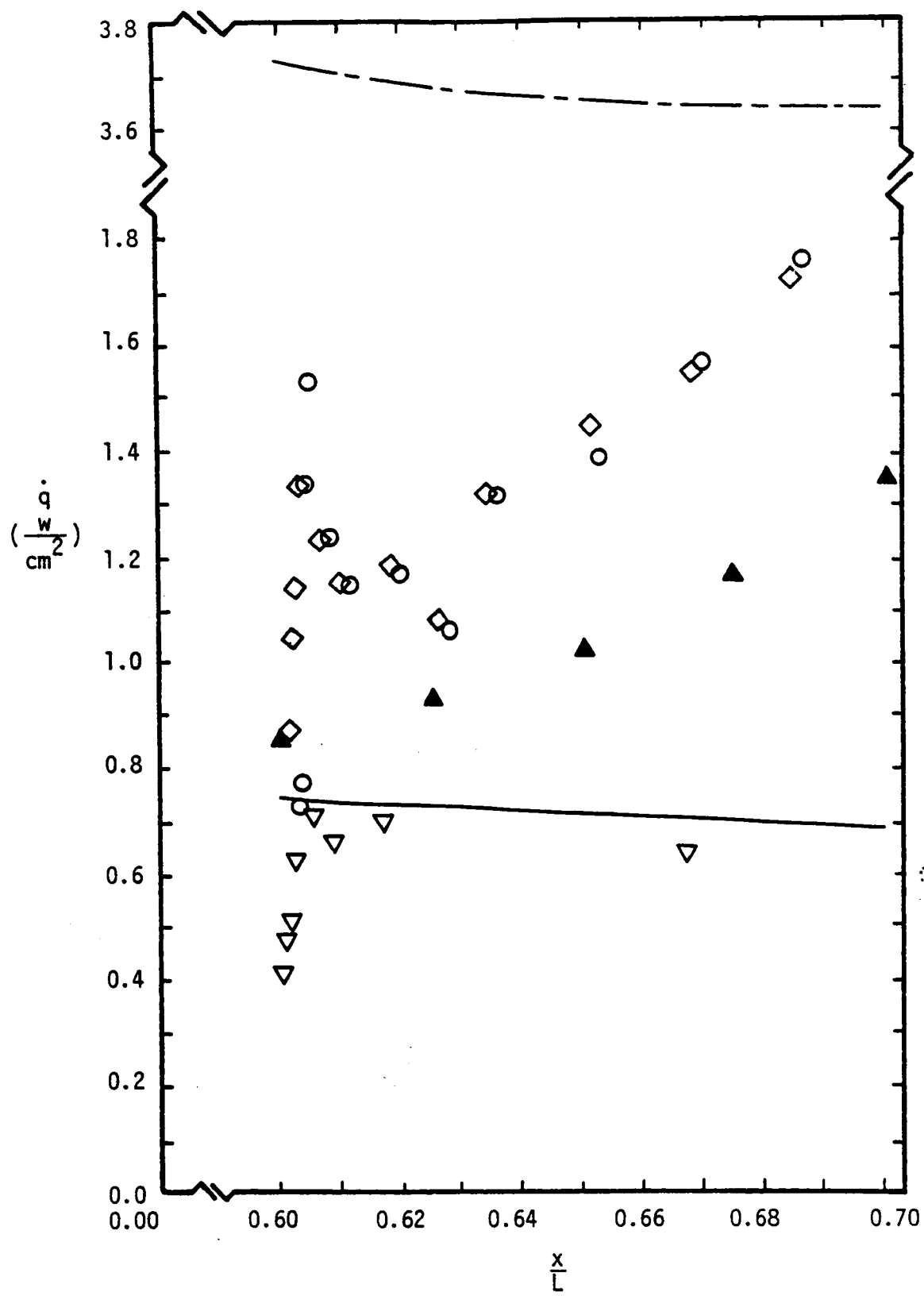
○ w = 0.508 cm (0.200 in)



(b) $Re_{\infty,L} = 4.01 \times 10^6$

Figure 9. - Continued.

The symbols used for this figure are those used in Fig. 9d, except that the solutions are for Run 40,BB



(c) $Re_{\infty,L} = 5.90 \times 10^6$

Figure 9. - Continued

-- BLIMP, Perfect-gas, $(Re_{\theta}/M_e)_{tr} = 0.0$
 — NSBL, Perfect-gas solution for Run 41,BB

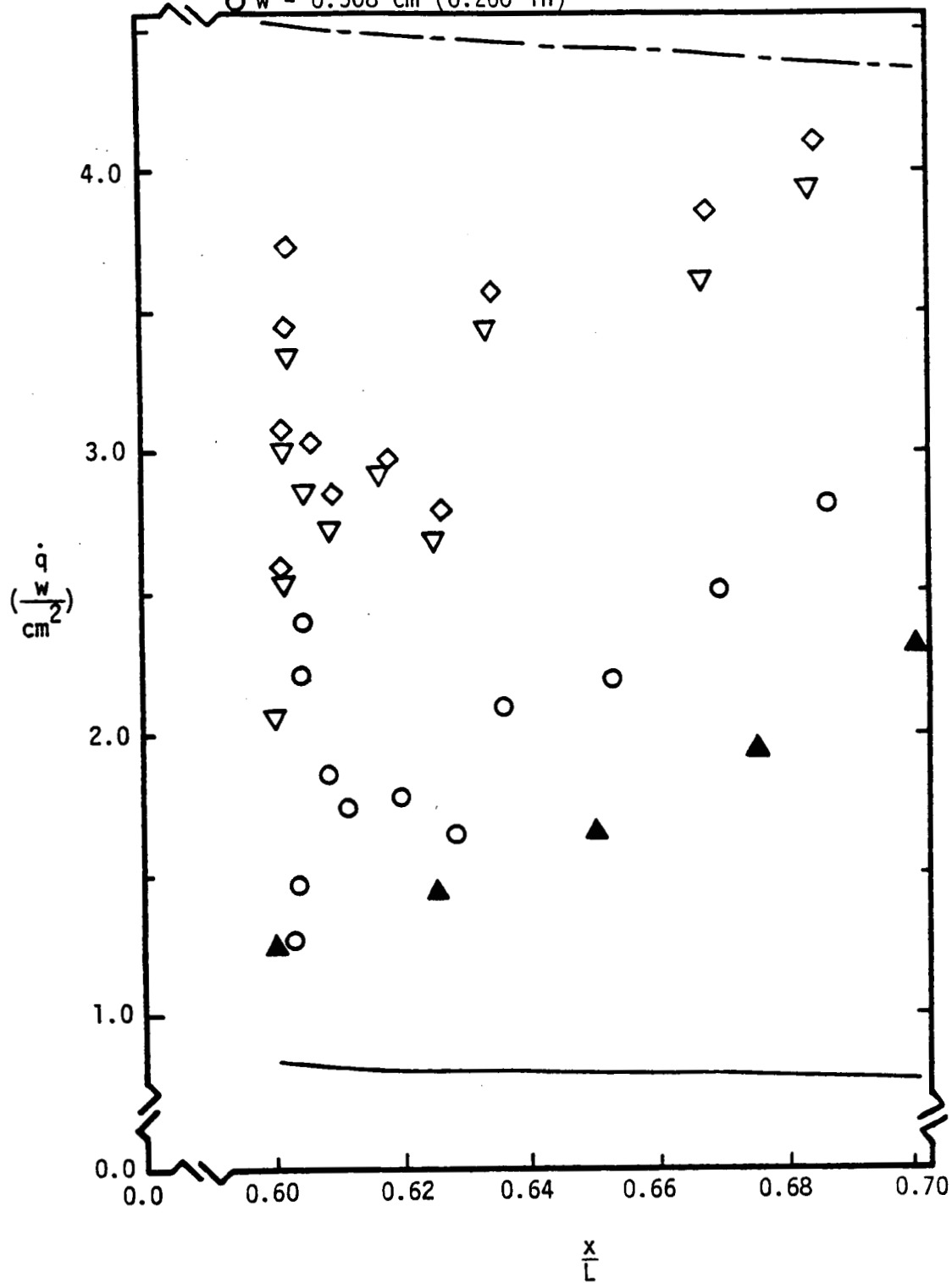
Data: ▲ Flat plate configuration C1

Single, transverse gap, C2

▽ $w = 0.127$ cm (0.050 in)

◇ $w = 0.254$ cm (0.100 in)

○ $w = 0.508$ cm (0.200 in)



(d) $Re_{\infty,L} = 8.11 \times 10^6$

Figure 9.- Concluded

$Re_{\infty,L}$: $\triangle 2.57 \times 10^6$ $\circ 4.01 \times 10^6$
 $\diamond 5.90 \times 10^6$ $\bigcirc 8.11 \times 10^6$

' $y = +0.135L$, $d = 1.016$ cm (section AA)
 no flag $y = 0.000L$, $d = 2.032$ cm (section BB)
 " $y = -0.135L$, $d = 4.064$ cm (section CC)

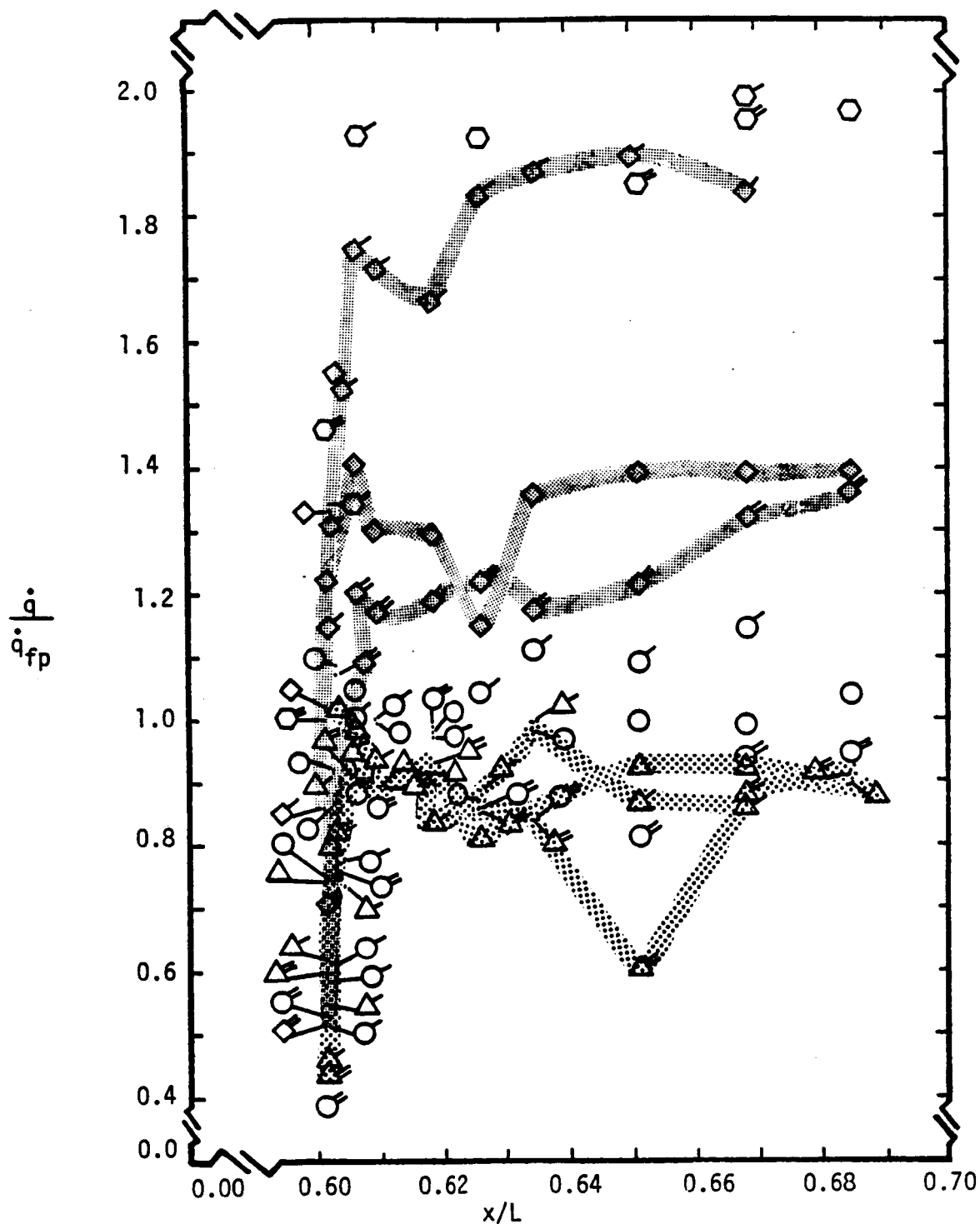


Figure 10. - The effect of Reynolds number and of gap depth on the heat-transfer distribution downstream of a single, transverse gap, $w = 0.254$ cm.

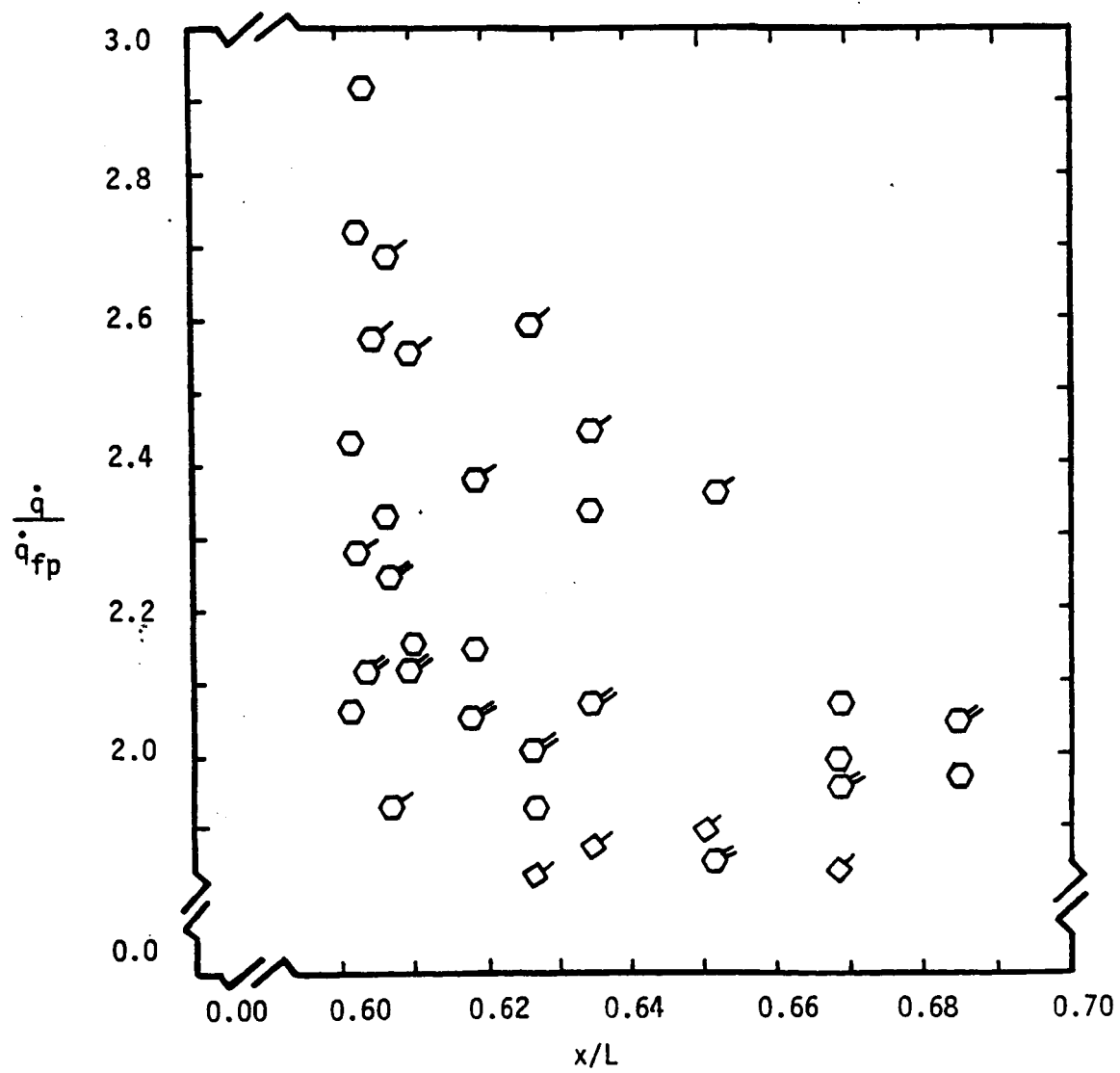


Figure 10. - Concluded.

◇ $w = 0.127$ cm

○ $w = 0.254$ cm

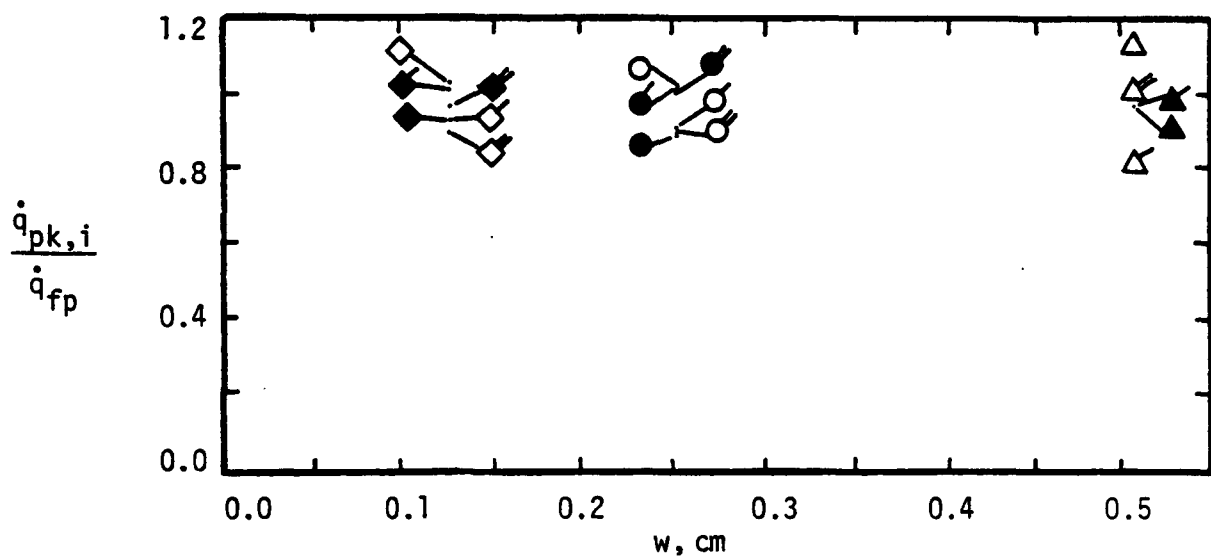
△ $w = 0.508$ cm

open symbols are for OH2A; filled symbols for OH2B

' $y = +0.135L$, $d = 1.016$ cm (Section AA)

No flag $y = 0.000L$, $d = 2.032$ cm (Section BB)

" $y = -0.135L$, $d = 4.064$ cm (Section CC)



(a) $Re_{\infty,L} = 2.57 \times 10^6$

Figure 11. - The maximum heating increase in the impingement region as a function of gap width for a single, transverse gap.

◇ w = 0.127 cm

○ w = 0.254 cm

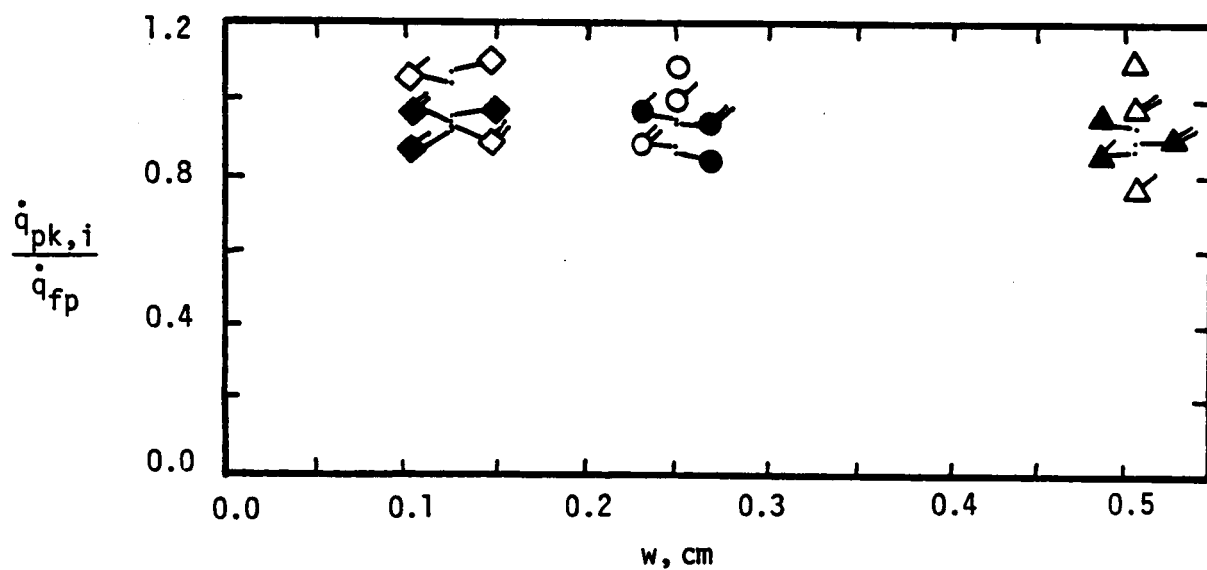
△ w = 0.508 cm

open symbols are for OH2A; filled symbols for OH2B

' y = +0.135L, d = 1.016 cm (Section AA)

No flag y = 0.000L, d = 2.032 cm (Section BB)

" y = -0.135L, d = 4.064 cm (Section CC)



(b) $Re_{\infty,L} = 4.01 \times 10^6$

Figure 11. - Concluded.

◇ $w = 0.127$ cm

○ $w = 0.254$ cm

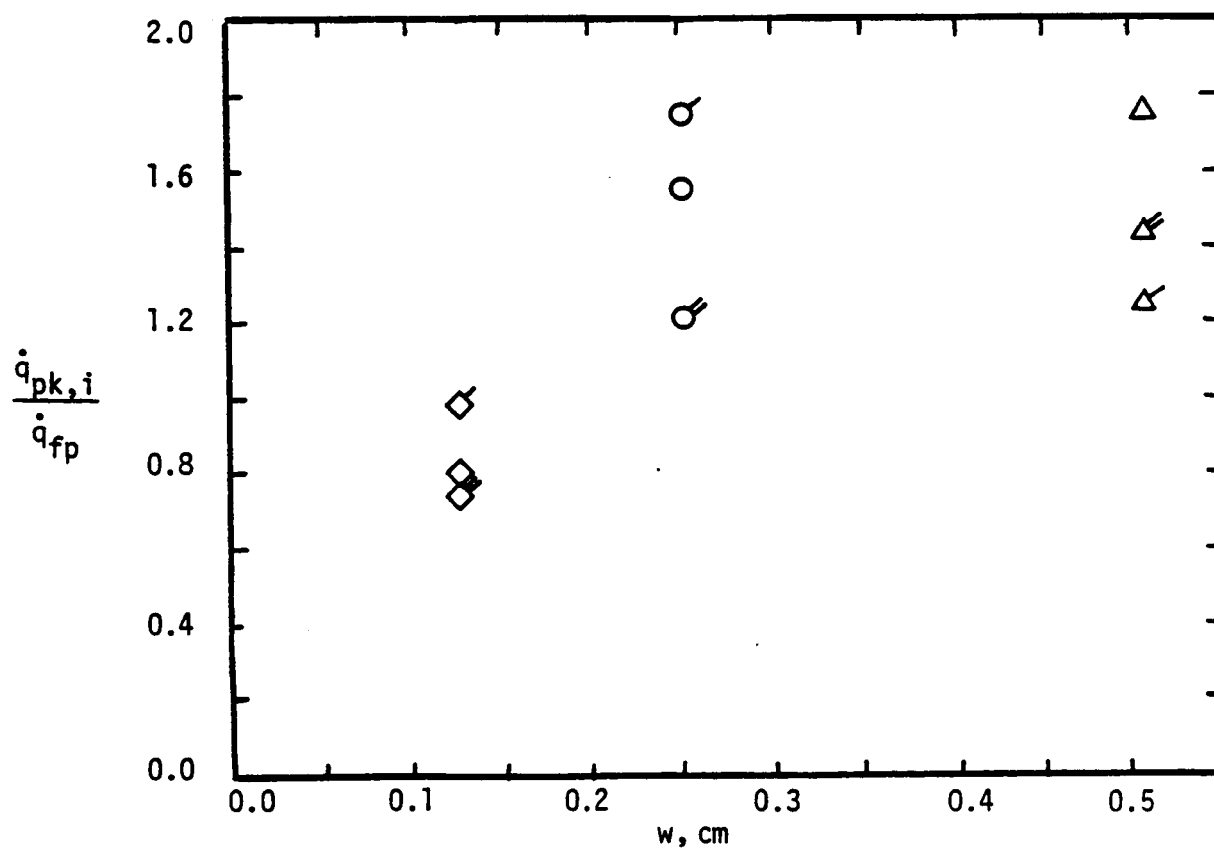
△ $w = 0.508$ cm

open symbols are for OH2A; filled symbols for OH2B

' $y = +0.135L$, $d = 1.016$ cm (Section AA)

No flag $y = 0.000L$, $d = 2.032$ cm (Section BB)

" $y = -0.135L$, $d = 4.064$ cm (Section CC)



(c) $Re_{\infty,L} = 5.90 \times 10^6$

Figure 11. - Continued.

◇ w = 0.127 cm

○ w = 0.254 cm

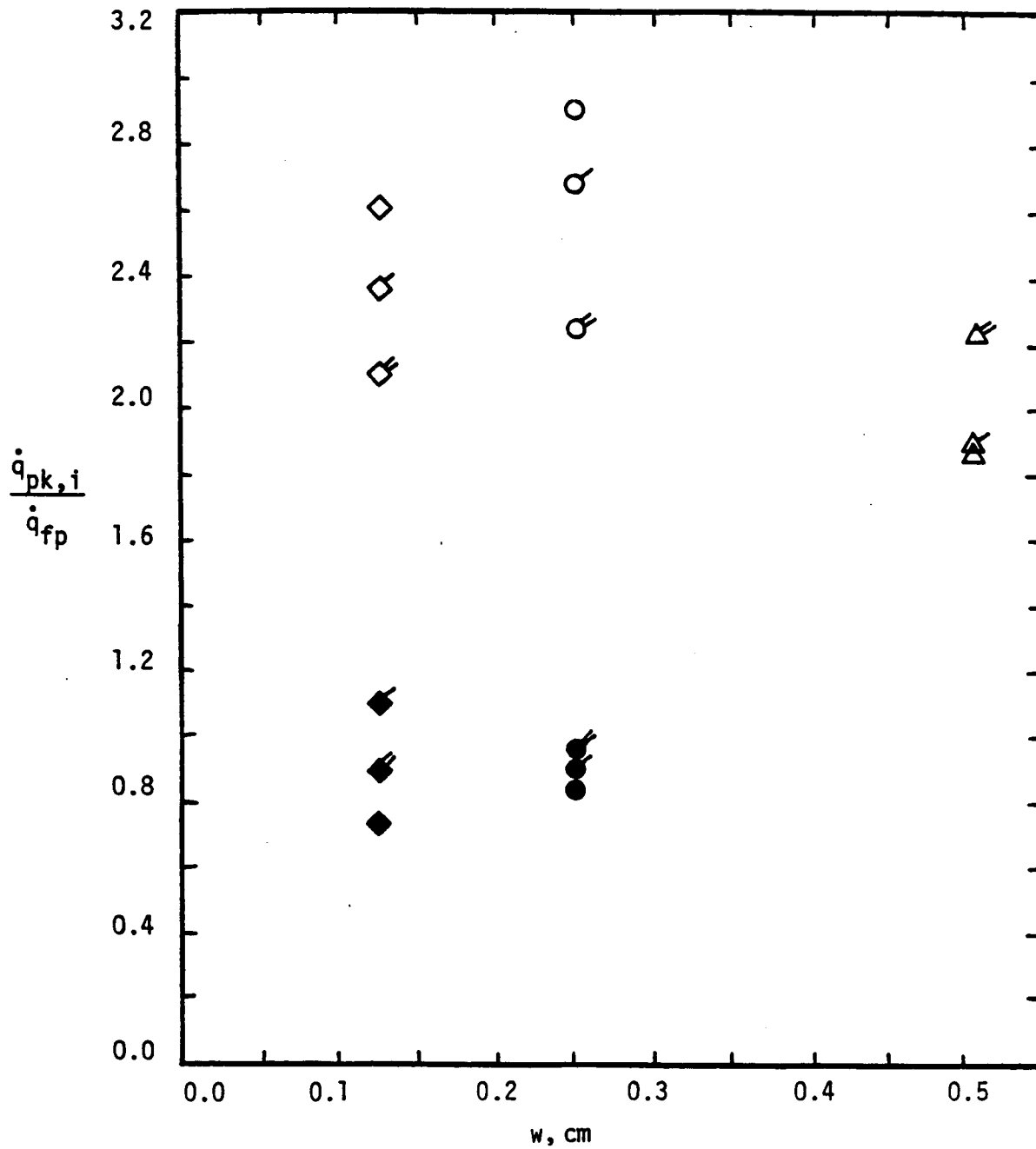
△ w = 0.508 cm

open symbols are for OH2A; filled symbols for OH2B

' y = +0.135L, d = 0.016 cm (Section AA)

No flag y = 0.000L, d = 2.032 cm (Section BB)

" y = -0.135L, d = 4.064 cm (Section CC)



(d) $Re_{\infty,L} = 8.11 \times 10^6$

Figure 11. - concluded.

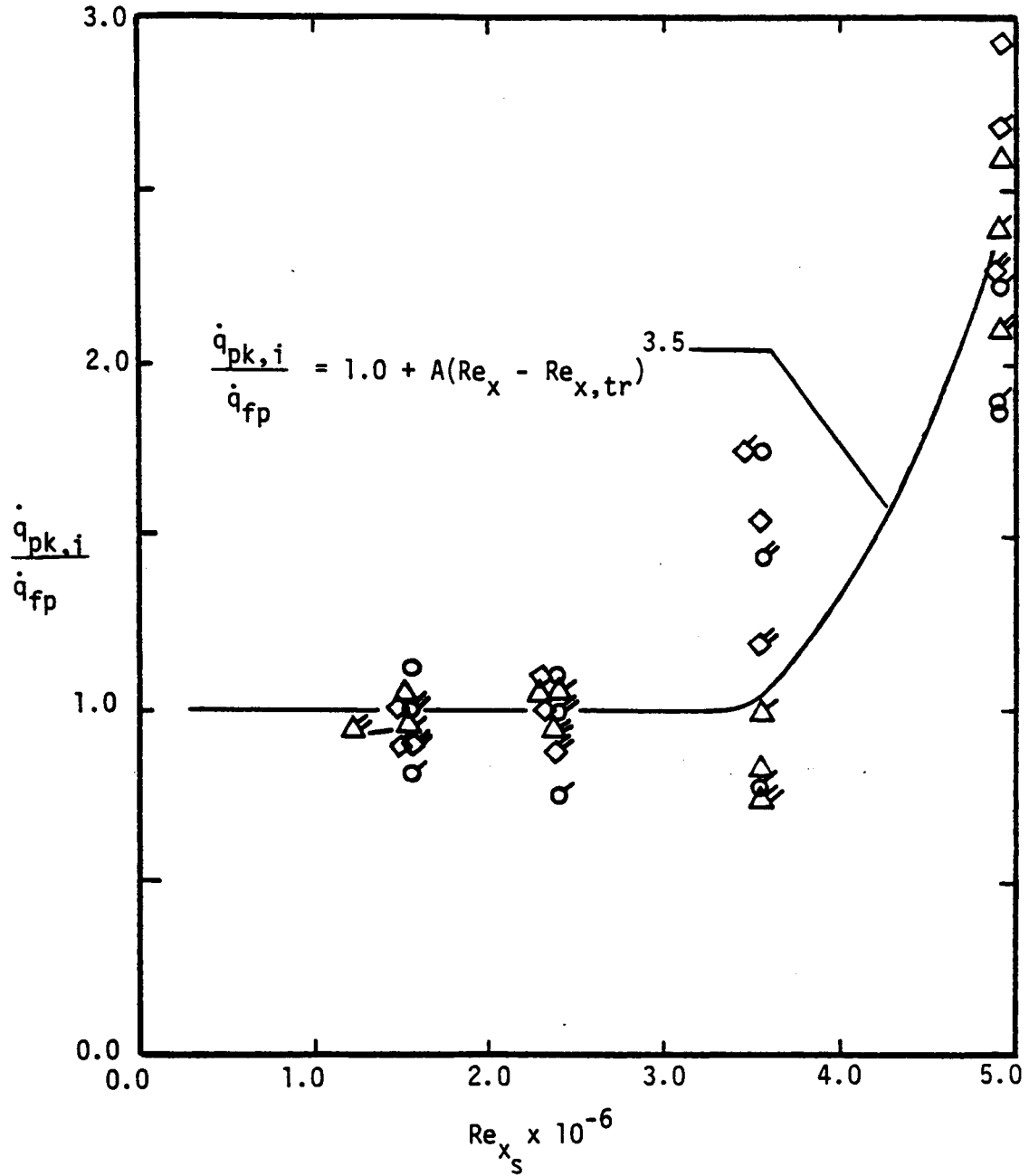
Data:

$\triangle w = 0.127 \text{ cm (0.050 in)}$

$\diamond w = 0.254 \text{ cm (0.100 in)}$

$\circ w = 0.508 \text{ cm (0.200 in)}$

No flag: $y = 0.000L$; $\prime y = +0.135L$; $\prime\prime y = -0.135L$



(a) At the gap

Figure 12. - Local maxima of the ratio of the perturbed heat-transfer rate to the corresponding flat-plate value for the C2 configuration, $k = 0.0$.

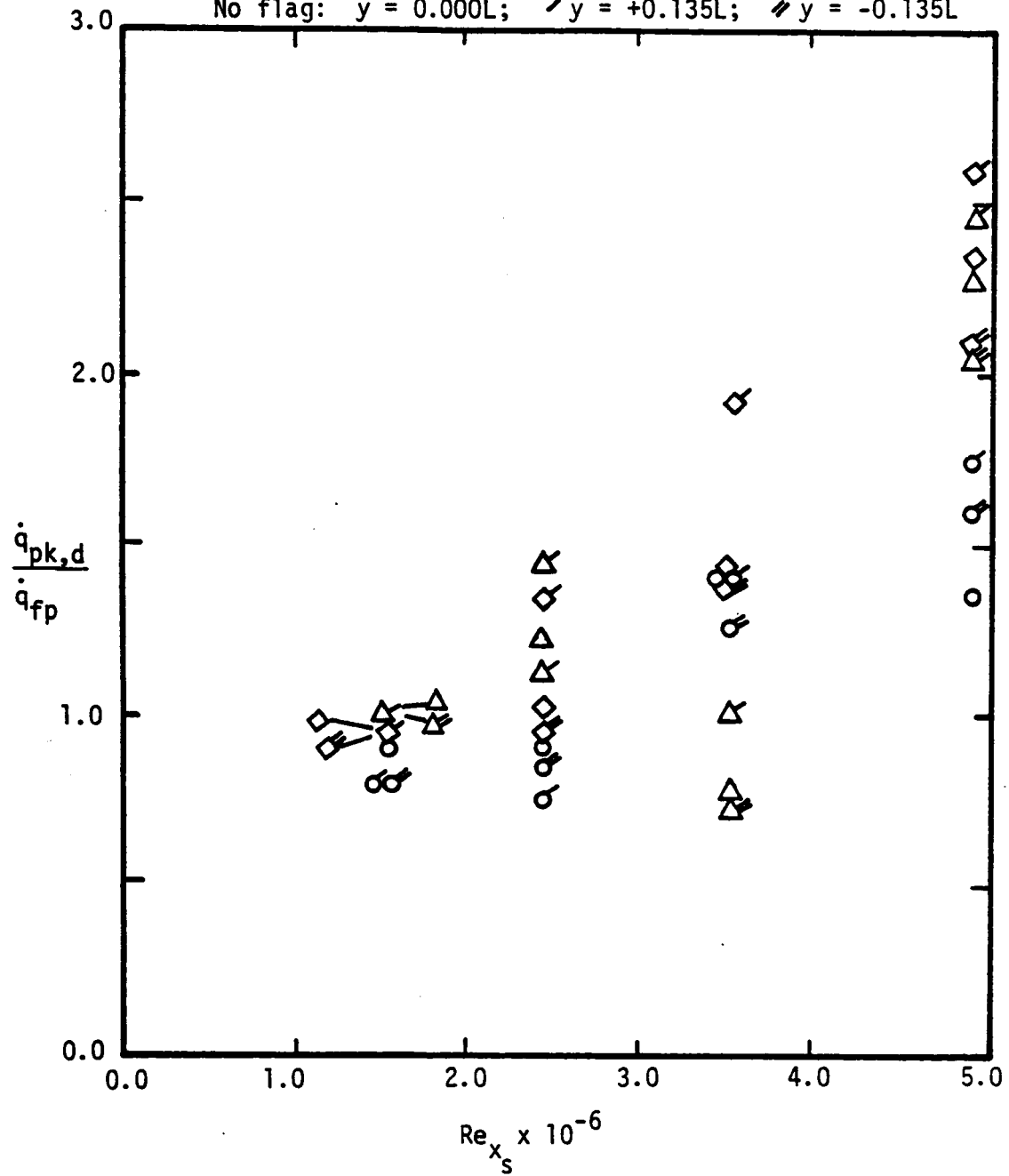
Data:

\triangle $w = 0.127$ cm (0.050 in)

\diamond $w = 0.254$ cm (0.100 in)

\circ $w = 0.508$ cm (0.200 in)

No flag: $y = 0.000L$; \nearrow $y = +0.135L$; \nwarrow $y = -0.135L$



(b) Downstream

Figure 12. -Concluded.

Points shown are for individual solutions

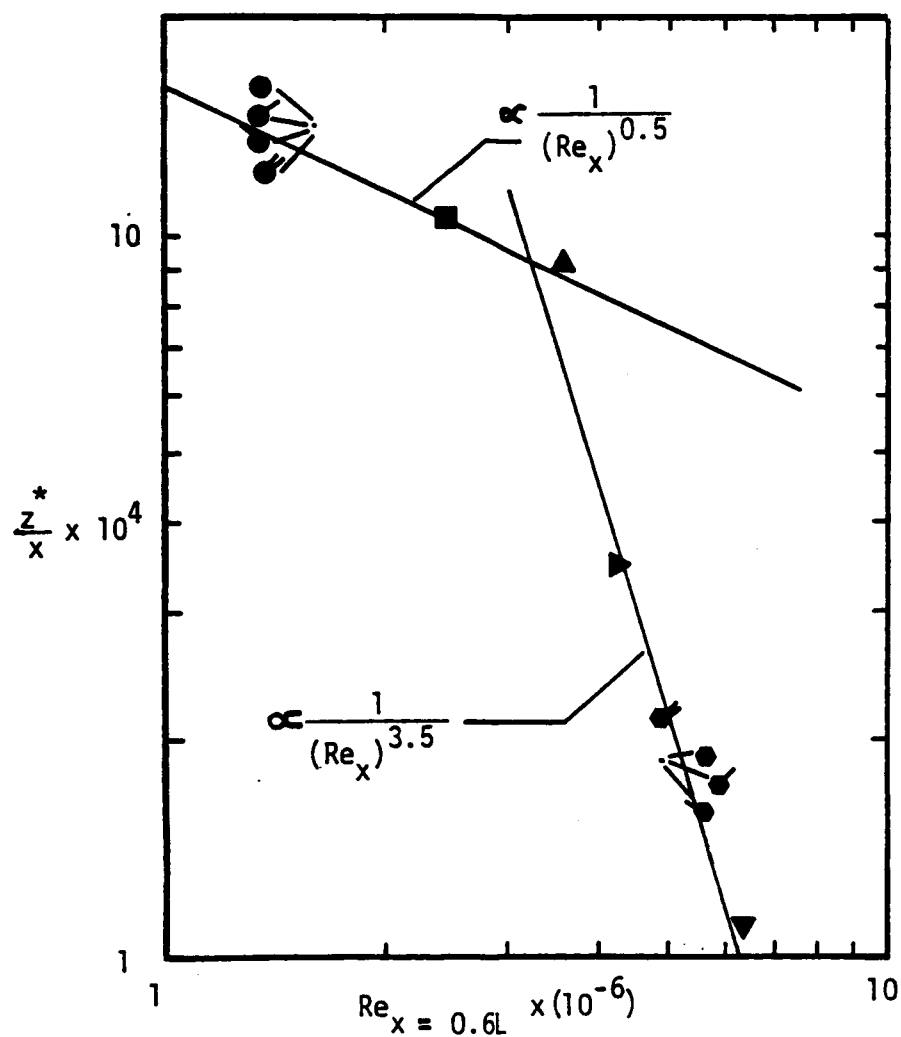
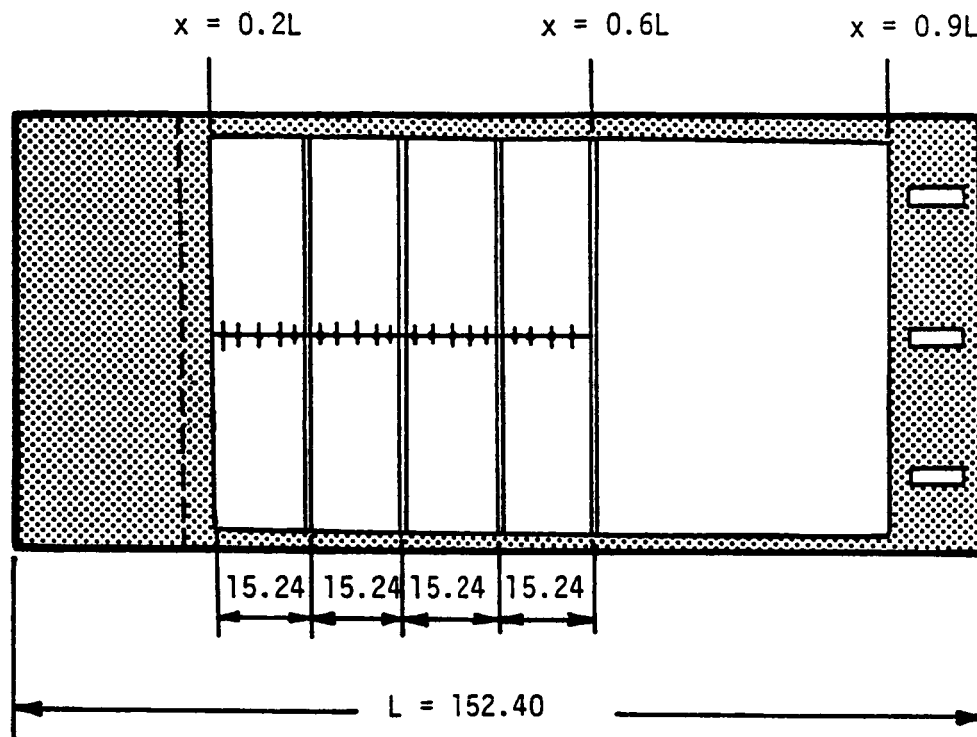


Figure 13. - The z-coordinate of the sonic point as a function of the Reynolds number at $x = 0.6L$



Note: dimensions are in cm

Figure 14. - Sketch of the multiple-transverse-gap insert placed in the structural carrier-plate to form Configuration 3(C3).

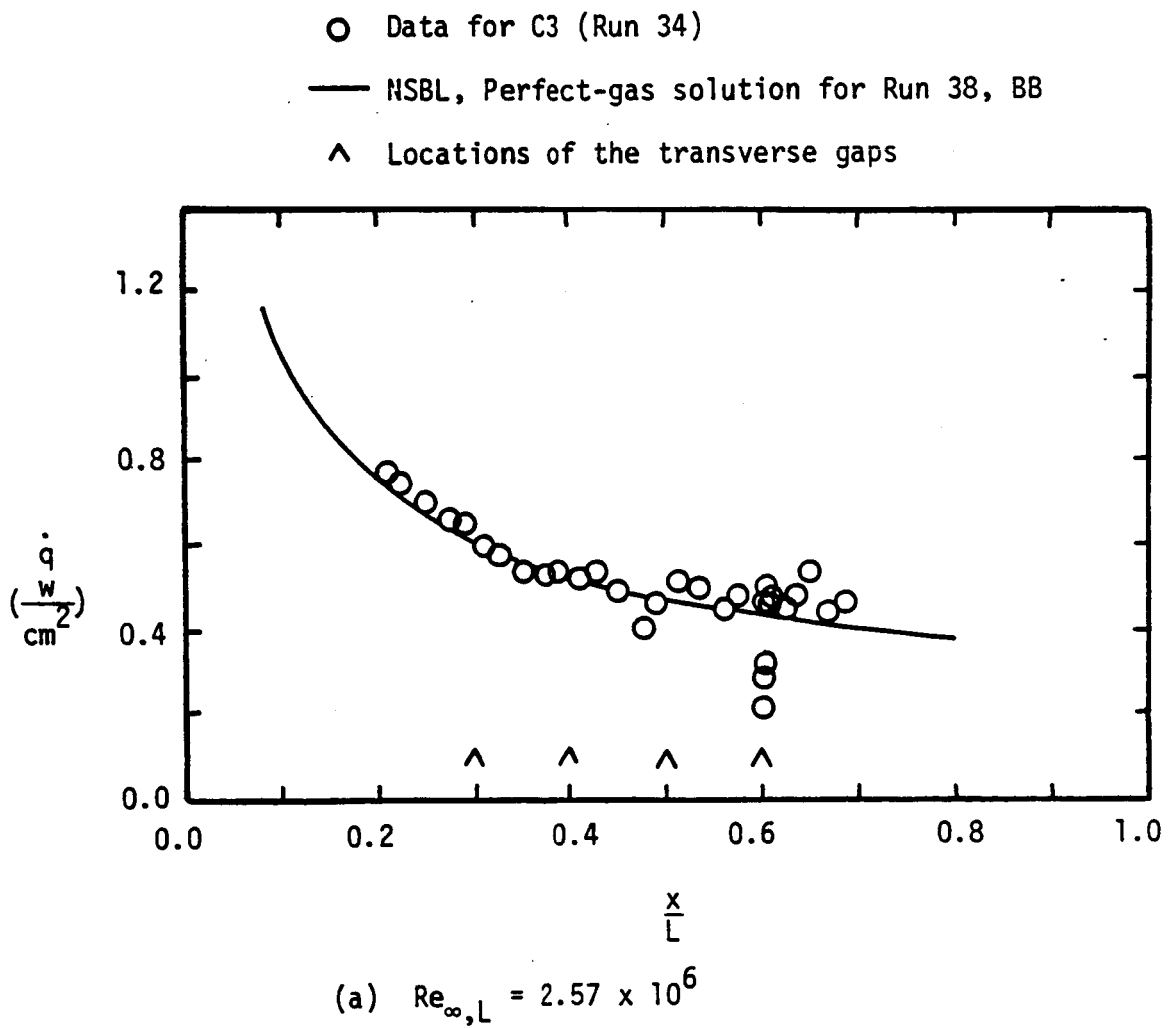
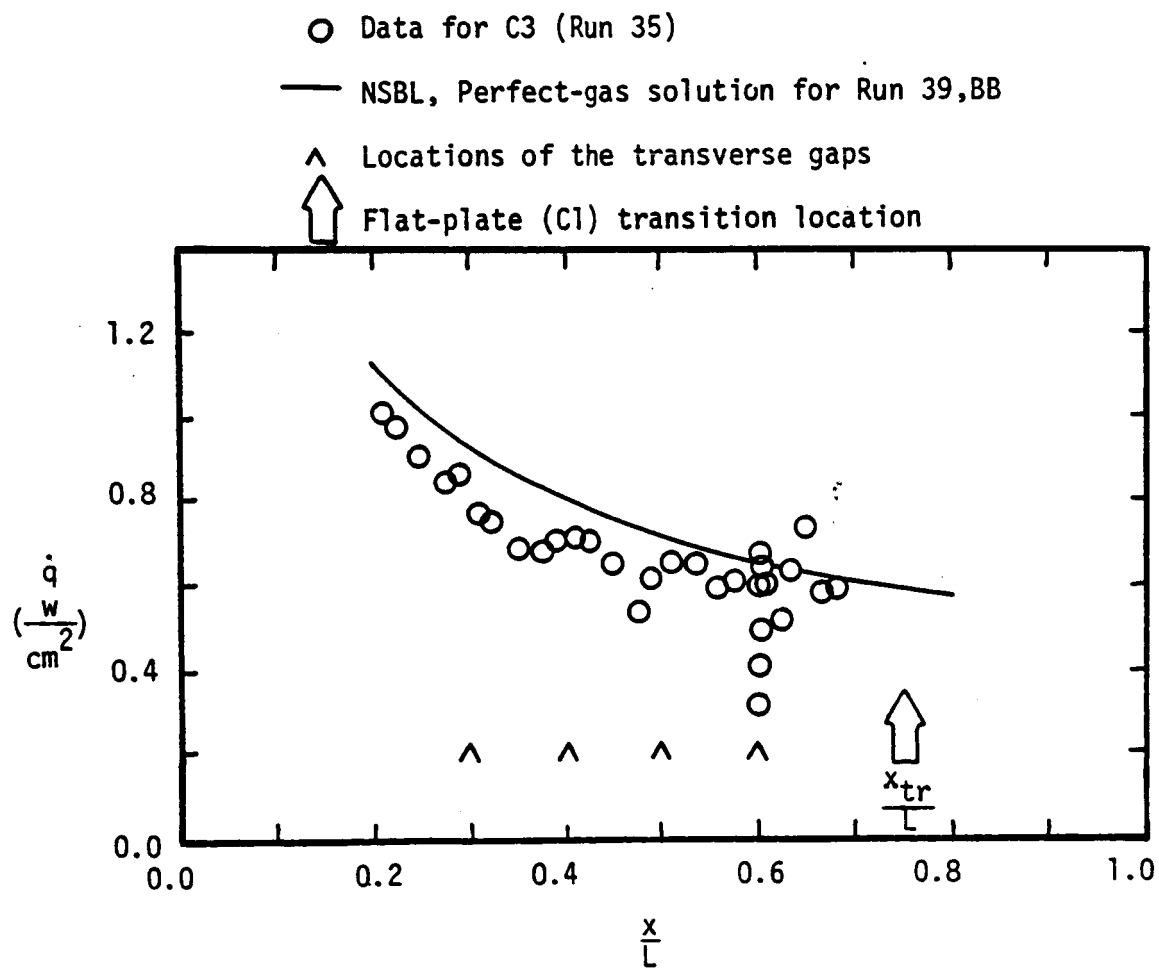
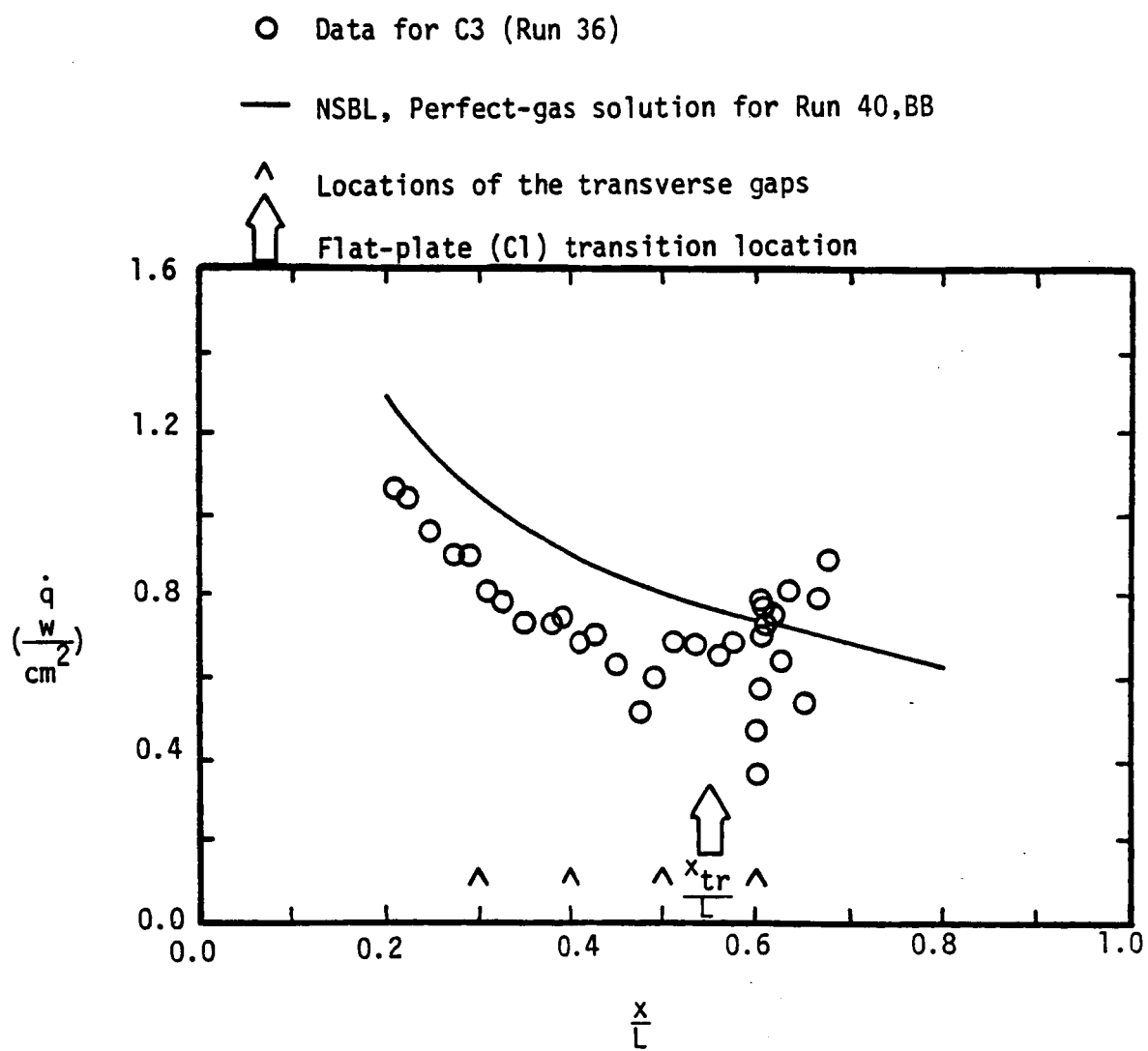


Figure 15. - The streamwise heat-transfer distribution for the multiple-transverse-gap configuration, C3.



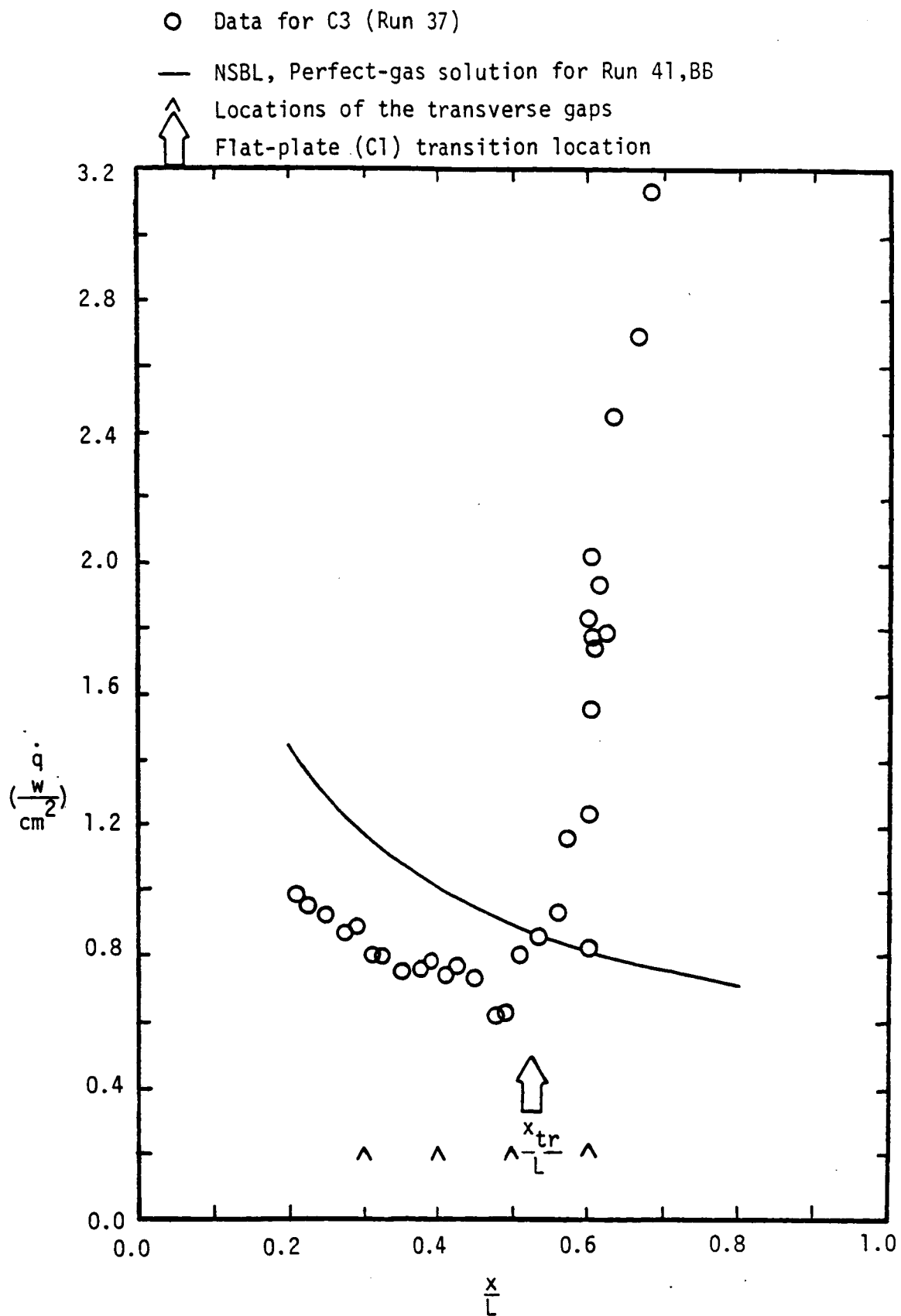
(b) $Re_{\infty,L} = 4.01 \times 10^6$

Figure 15. - Continued.



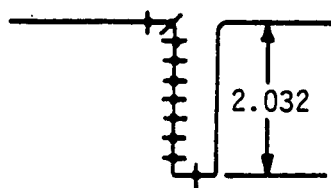
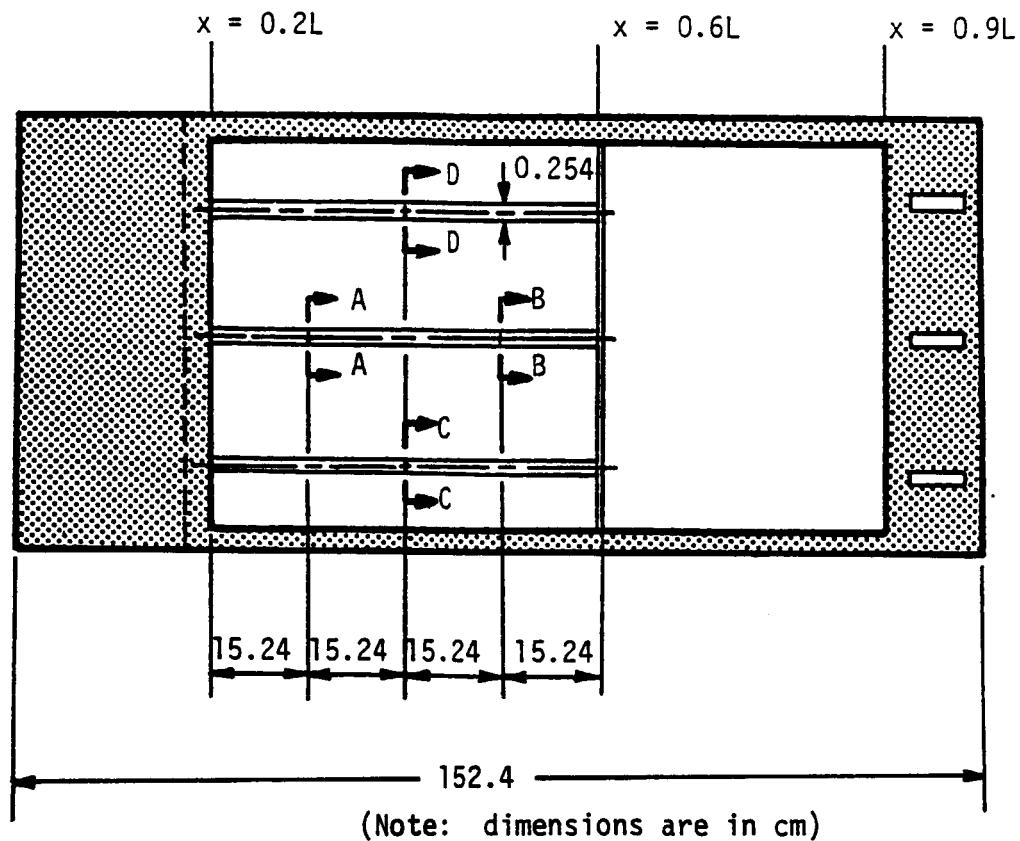
(c) $Re_{\infty,L} = 5.90 \times 10^6$

Figure 15. - Continued.

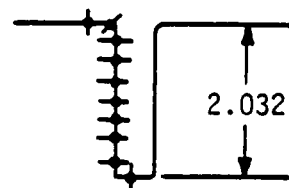


(d) $Re_{\infty,L} = 8.11 \times 10^6$

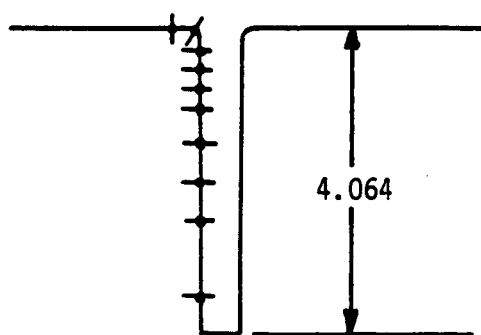
Figure 15. - Concluded.



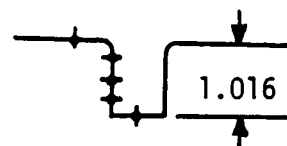
Section AA



Section BB



Section CC



Section DD

Figure 16. - Sketch of longitudinal, intersecting gap insert placed in the structural carrier plate to form Configuration 4(C4)

○ $z = 0.000$ cm; ◇ $z = -0.045$ cm; □ $z = -0.254$ cm

For the data

at $x = 0.3L$, $d = 2.032$ cm and $y = 0.000L$

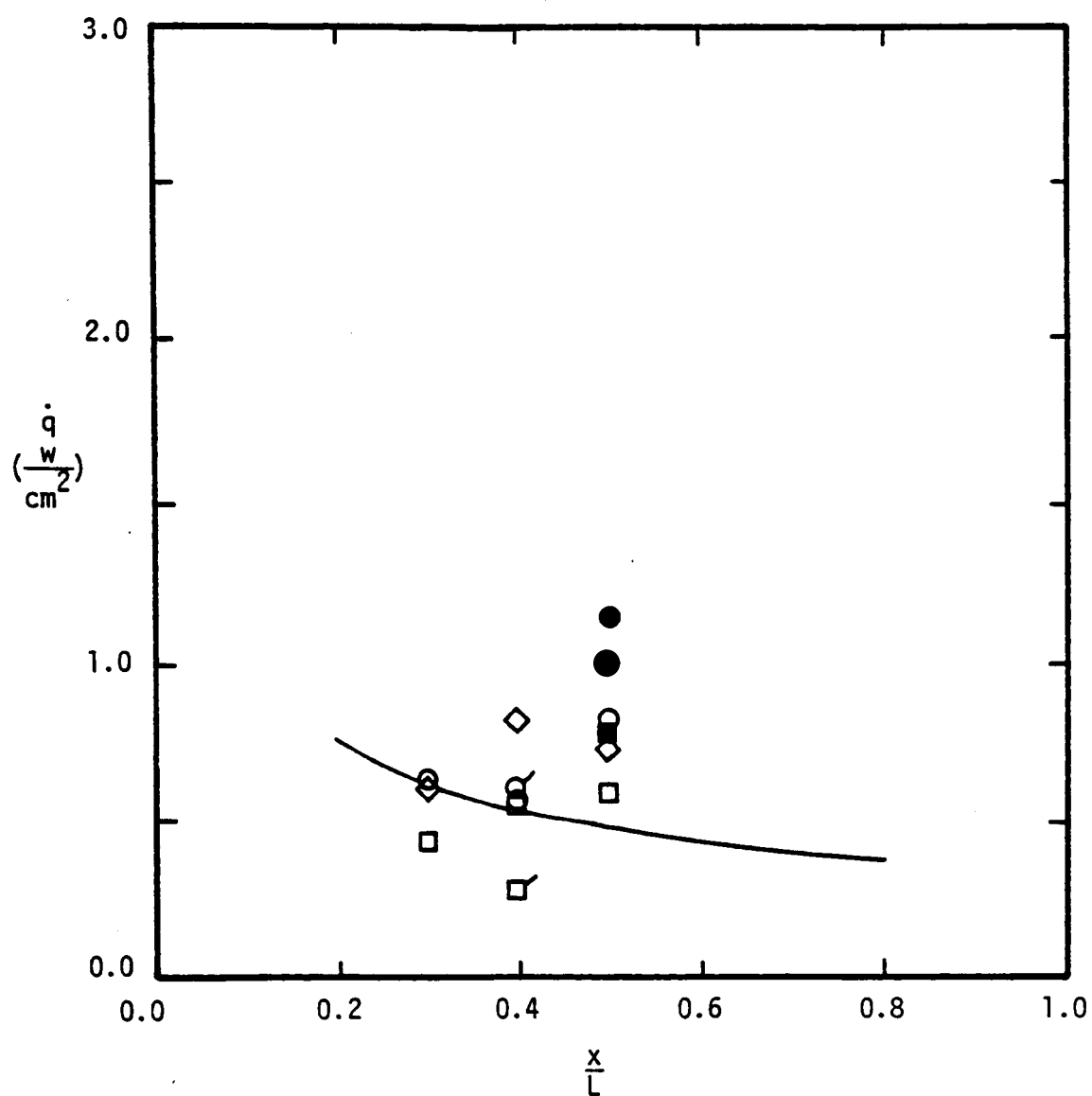
at $x = 0.4L$, $d = 1.016$ cm and $y = +0.135L$ if flagged

$d = 4.064$ cm and $y = -0.135L$ if unflagged

at $x = 0.5L$, $d = 2.032$ cm and $y = 0.000L$

filled symbols are for limited instrumentation runs

— NSBL, Perfect-gas solution for Run 38,8B



(a) $Re_{\infty,L} = 2.57 \times 10^6$

Figure 17. - The heat-transfer rates measured along the longitudinal slots of C4.

○ $z = 0.000$ cm; ◇ $z = -0.045$ cm; □ $z = 0.254$ cm

For the data

at $x = 0.3L$, $d = 2.032$ cm and $y = 0.000L$

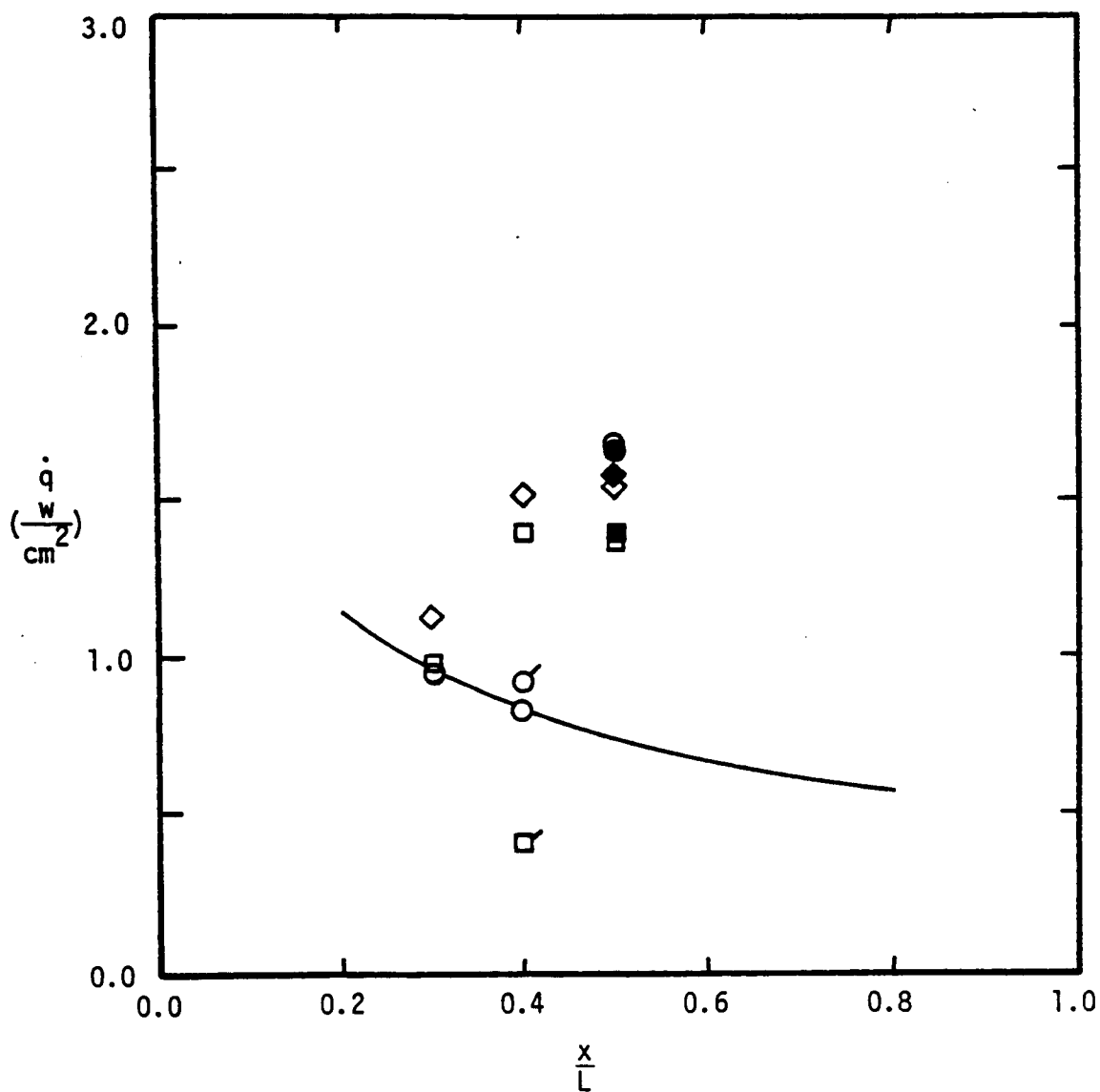
at $x = 0.4L$, $d = 1.016$ cm and $y = +0.135L$ if flagged

$d = 4.064$ cm and $y = -0.135L$ if unflagged

at $x = 0.5L$, $d = 2.032$ cm and $y = 0.000L$

filled symbols are for limited instrumentation runs

— NSBL, Perfect-gas solution for Run 39,BB



(b) $Re_{\infty,L} = 4.01 \times 10^6$

Figure 17. Continued

○ $z = 0.000$ cm; ◇ $z = -0.045$ cm; □ $z = -0.254$ cm.

For the data

at $x = 0.3L$, $d = 2.032$ cm and $y = 0.000L$

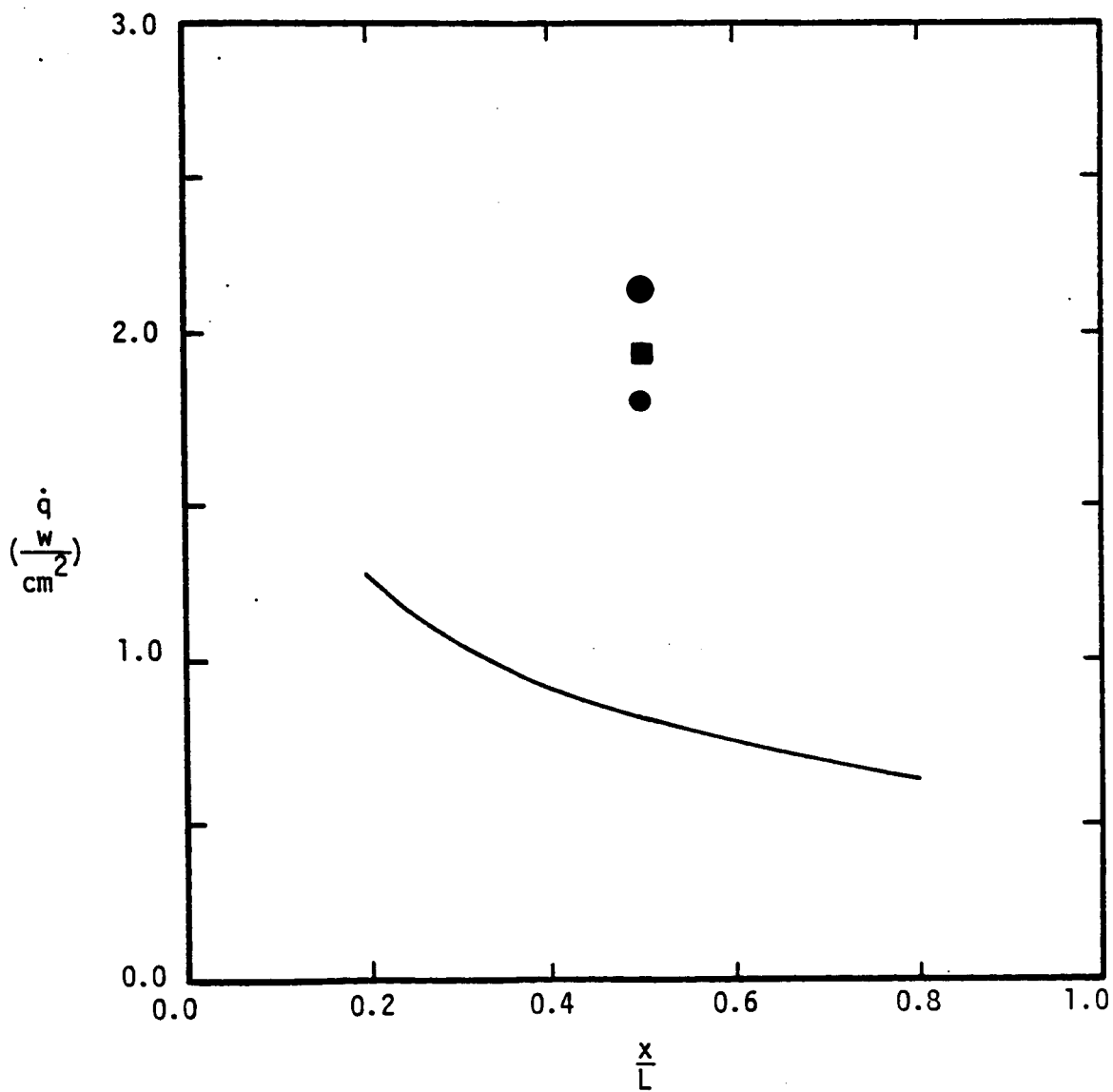
at $x = 0.4L$, $d = 1.016$ cm and $y = +1.135L$ if flagged

$d = 4.064$ cm and $y = -0.135L$ if unflagged

at $x = 0.5L$, $d = 2.032$ cm and $y = 0.000L$

filled symbols are for limited instrumentation runs

— NSBL, Perfect-gas solution for Run 40,BB



(c) $Re_{\infty,L} = 5.90 \times 10^6$

Figure 17. Continued.

○ $z = 0.000$ cm; ◇ $z = -0.045$ cm; □ $z = -0.254$ cm

For the data

at $x = 0.3L$, $d = 2.032$ cm and $y = 0.000L$

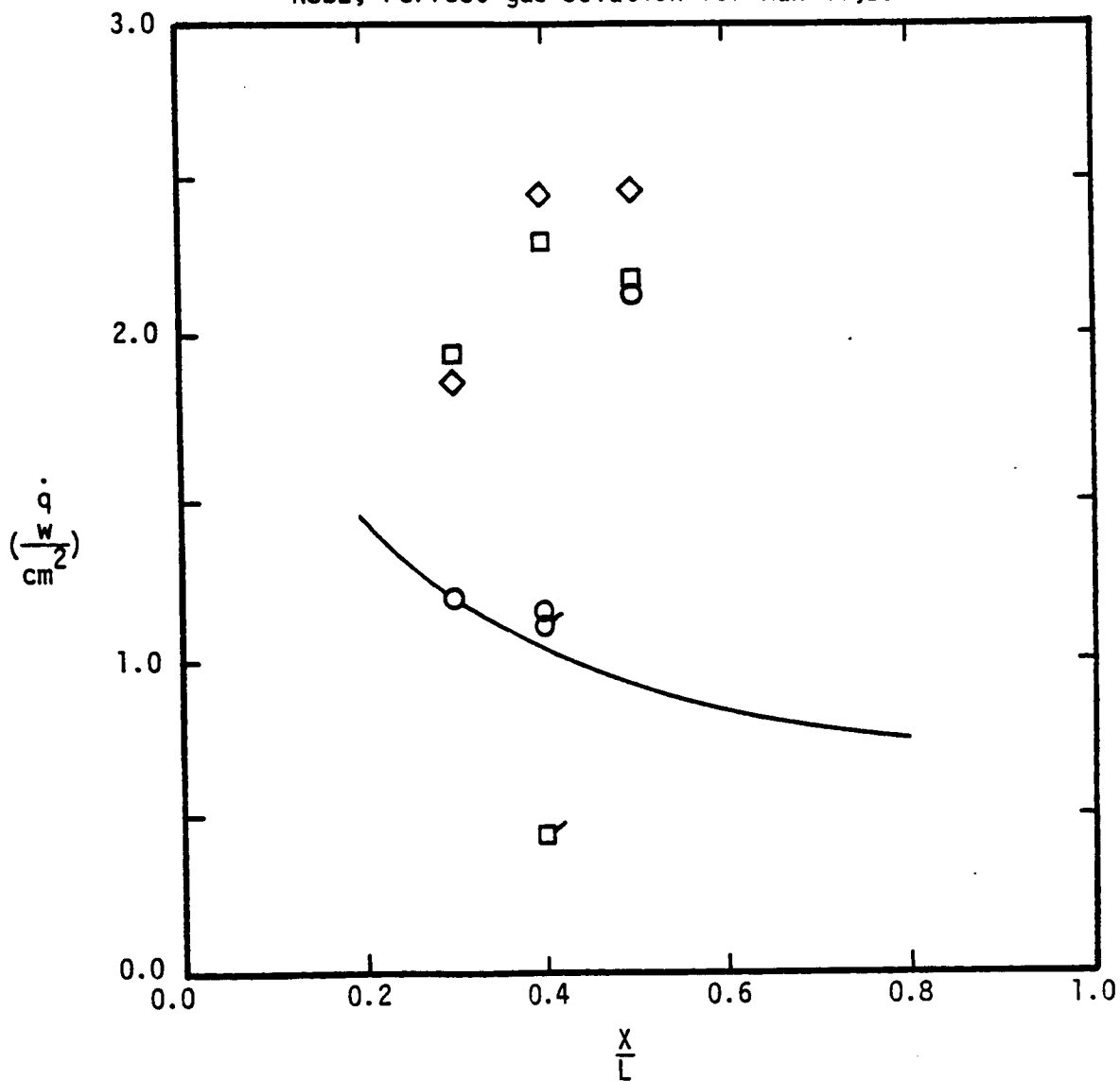
at $x = 0.4L$, $d = 1.016$ cm and $y = +0.135L$ if flagged

$d = 4.064$ cm and $y = -0.135L$ if unflagged

at $x = 0.5L$, $d = 2.032$ cm and $y = 0.000L$

filled symbols are for limited instrumentation runs

— NSBL, Perfect-gas solution for Run 41,BB



(d) $Re_{\infty,L} = 8.11 \times 10^6$

Figure 17. - Concluded

○ Section AA □ Section BB ◇ Section CC ○ Section DD

See Figure 16 for the geometry of these sections

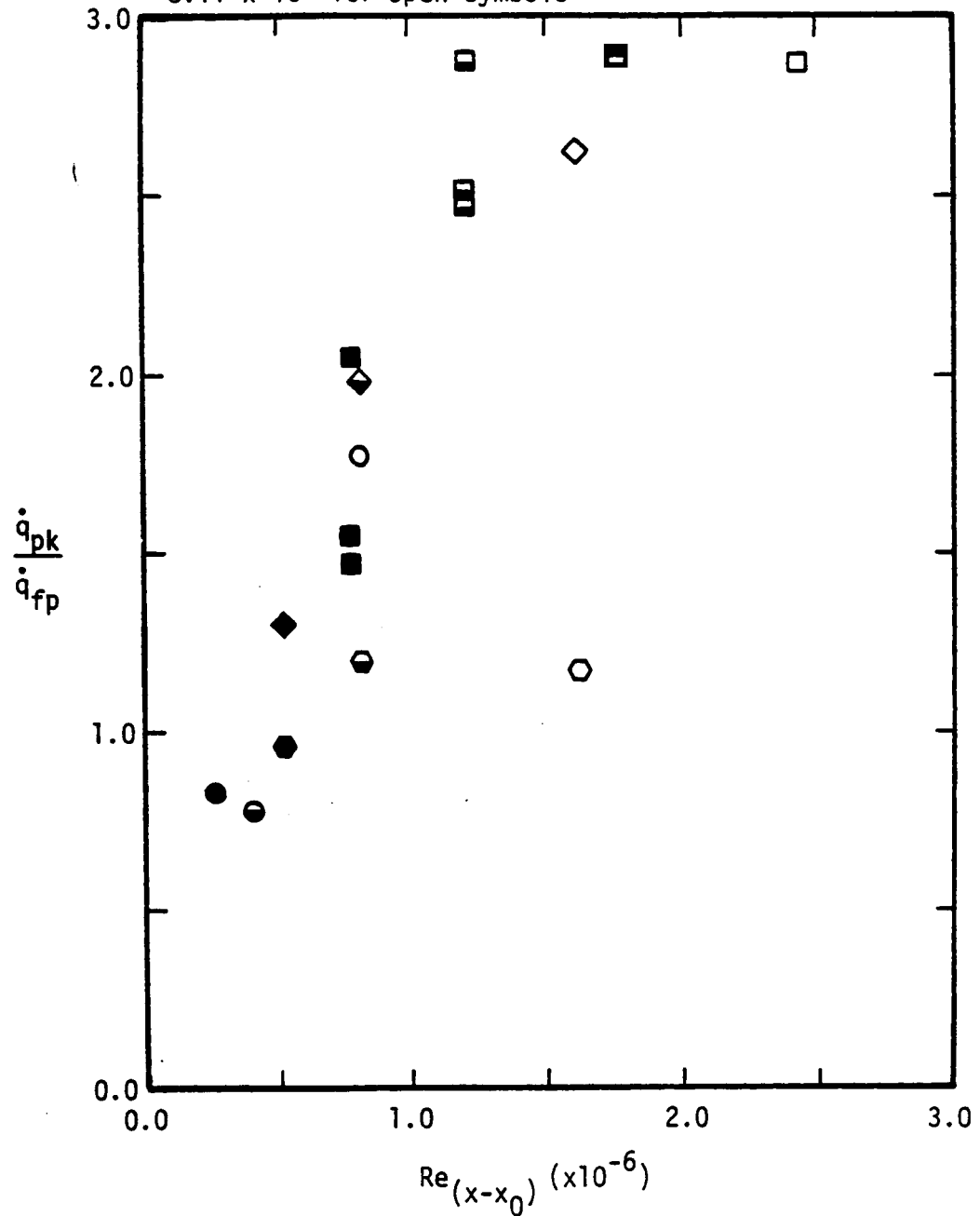
$Re_{\infty, l}$

2.57×10^6 for filled symbols

4.01×10^6 for bottom-half filled symbols

5.90×10^6 for top-half filled symbols

8.11×10^6 for open symbols



(a) Peak heating.

Figure 18. - The nondimensionalized heat-transfer rates for locations along the longitudinal slots of C4.

○ Section AA □ Section BB ◇ Section CC ○ Section DD

See Figure 16 for the geometry of these sections

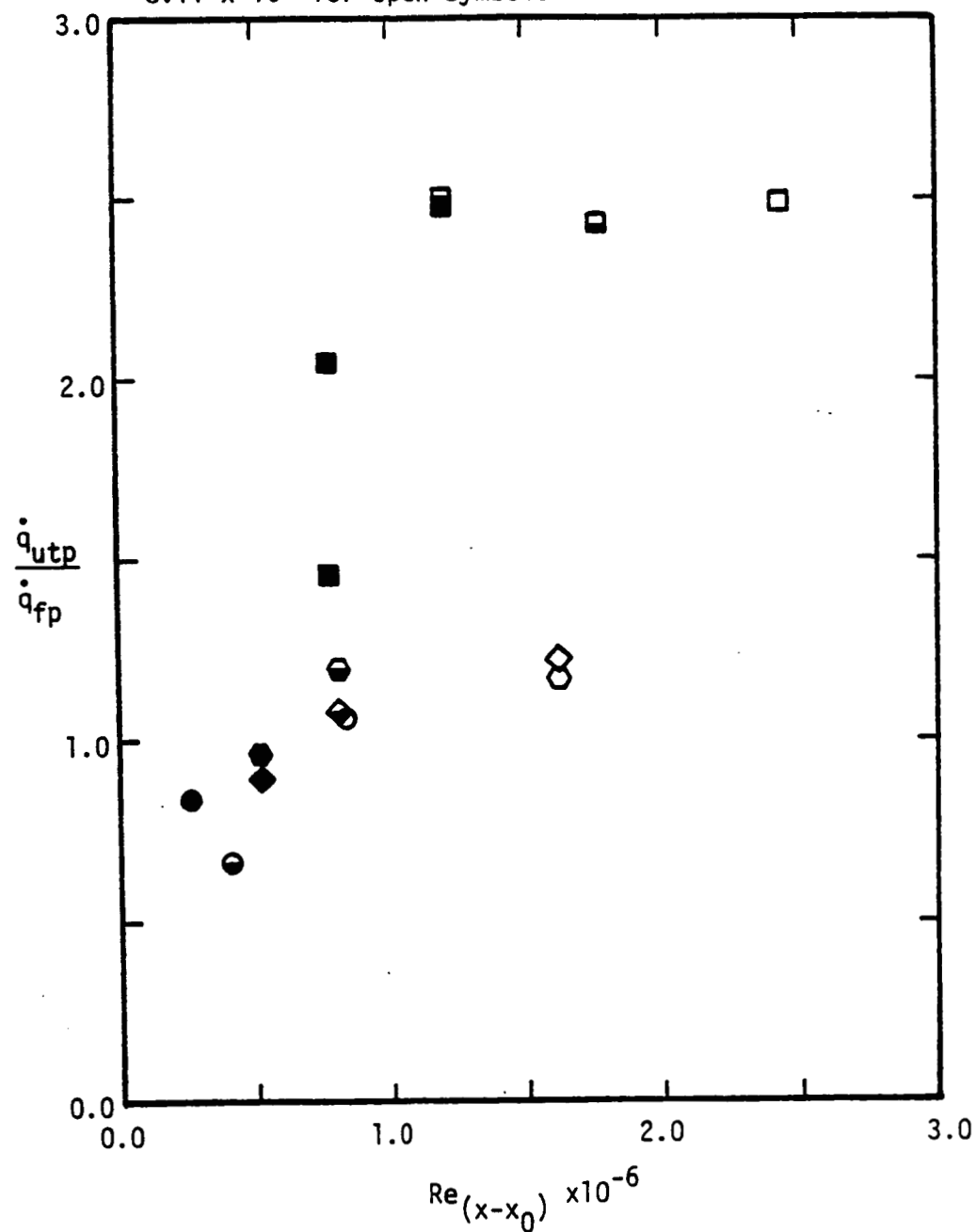
$Re_{\infty, L}$

2.57×10^6 for filled symbols

4.01×10^6 for bottom-half filled symbols

5.90×10^6 for top-half filled symbols

8.11×10^6 for open symbols

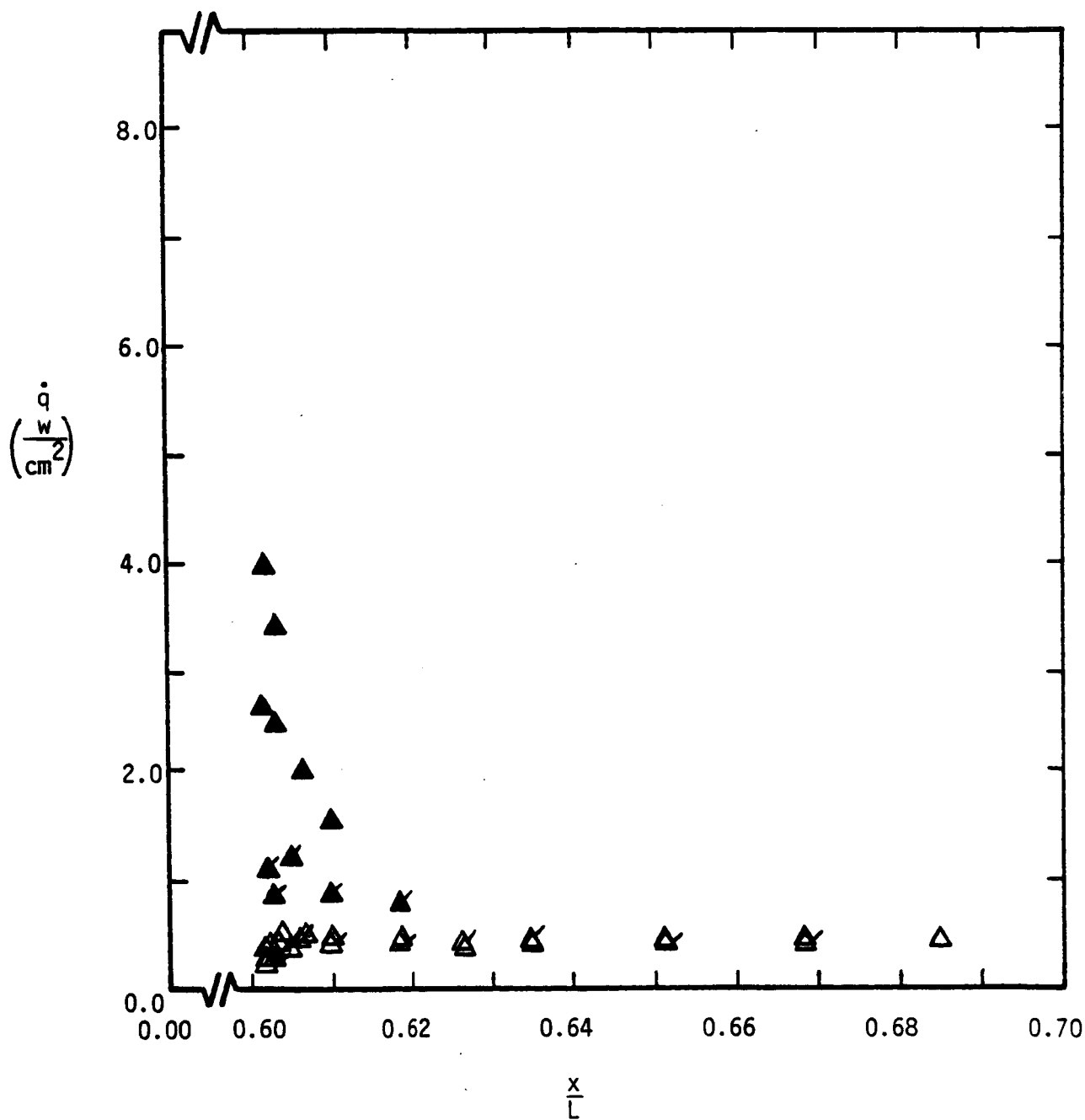


(b) Heating at the upper tangency point

Figure 18. - Concluded.

- \triangle Single, transverse gap, C2
 \blacktriangle Intersecting gap (or T), C4

Flagged symbols: $y = +0.135L$, $d = 1.016$ cm
 Unflagged symbols: $y = 0.000L$, $d = 2.032$ cm



(a) $Re_{\infty, L} = 2.57 \times 10^6$

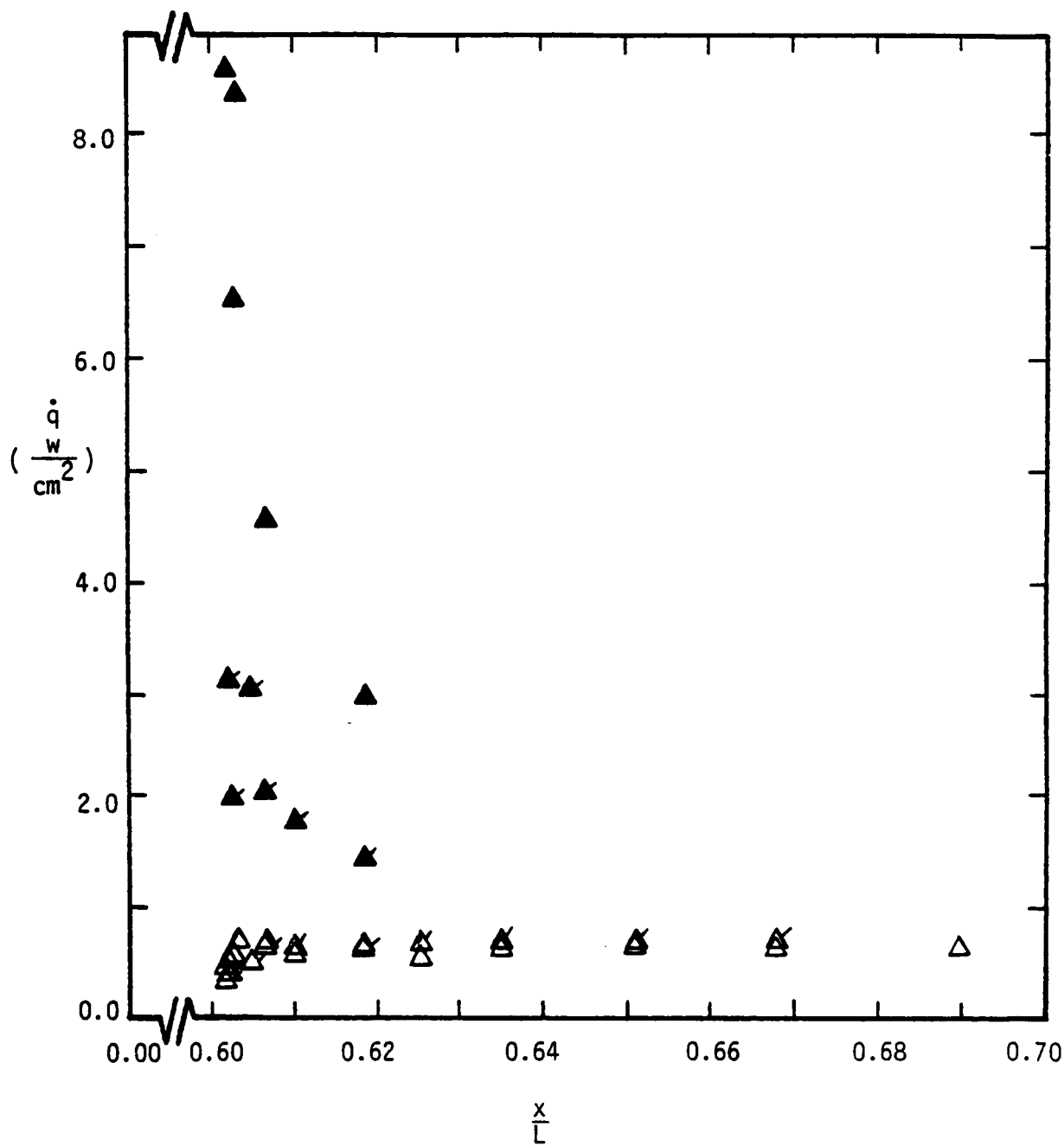
Figure 19. - A comparison of the heat-transfer-rate distributions downstream of a single, transverse gap (C2) and of a T gap (C4).

△ Single, transverse gap, C2

▲ Intersecting gap (or T), C4

Flagged symbols: $y = +0.135L$, $d = 1.016$ cm

Unflagged symbols: $y = 0.000L$, $d = 2.032$ cm



(b) $Re_{\infty, L} = 4.01 \times 10^6$

Figure 19. - Continued.

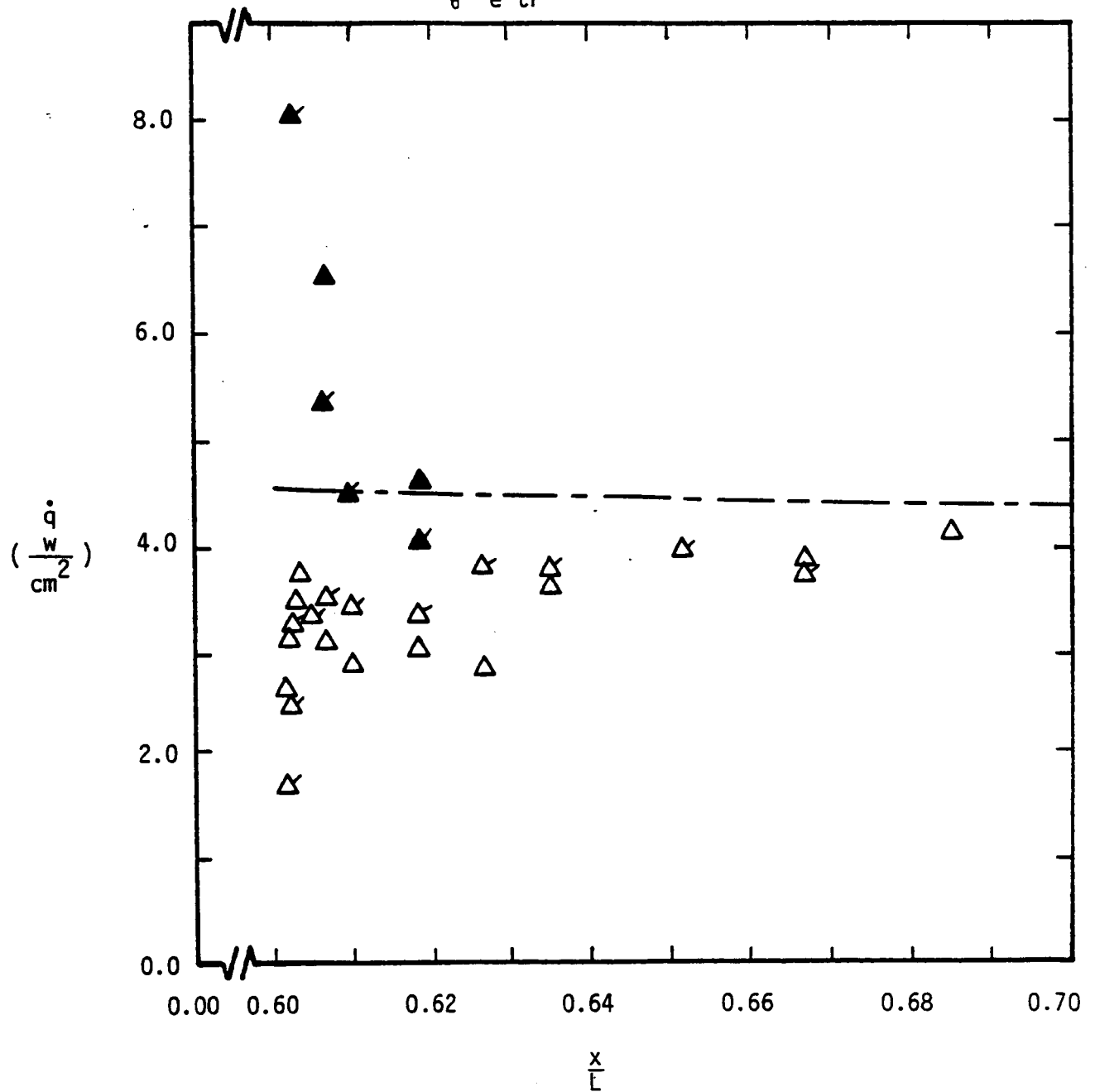
△ Single, transverse gap, C2

▲ Intersecting gap (or T), C4

Flagged symbols: $y = +0.135L$, $d = 1.016$ cm

Unflagged symbols: $y = 0.000L$, $d = 2.032$ cm

— - BLIMP, Perfect-gas, $(Re_\theta/M_e)_{tr} = 0.0$

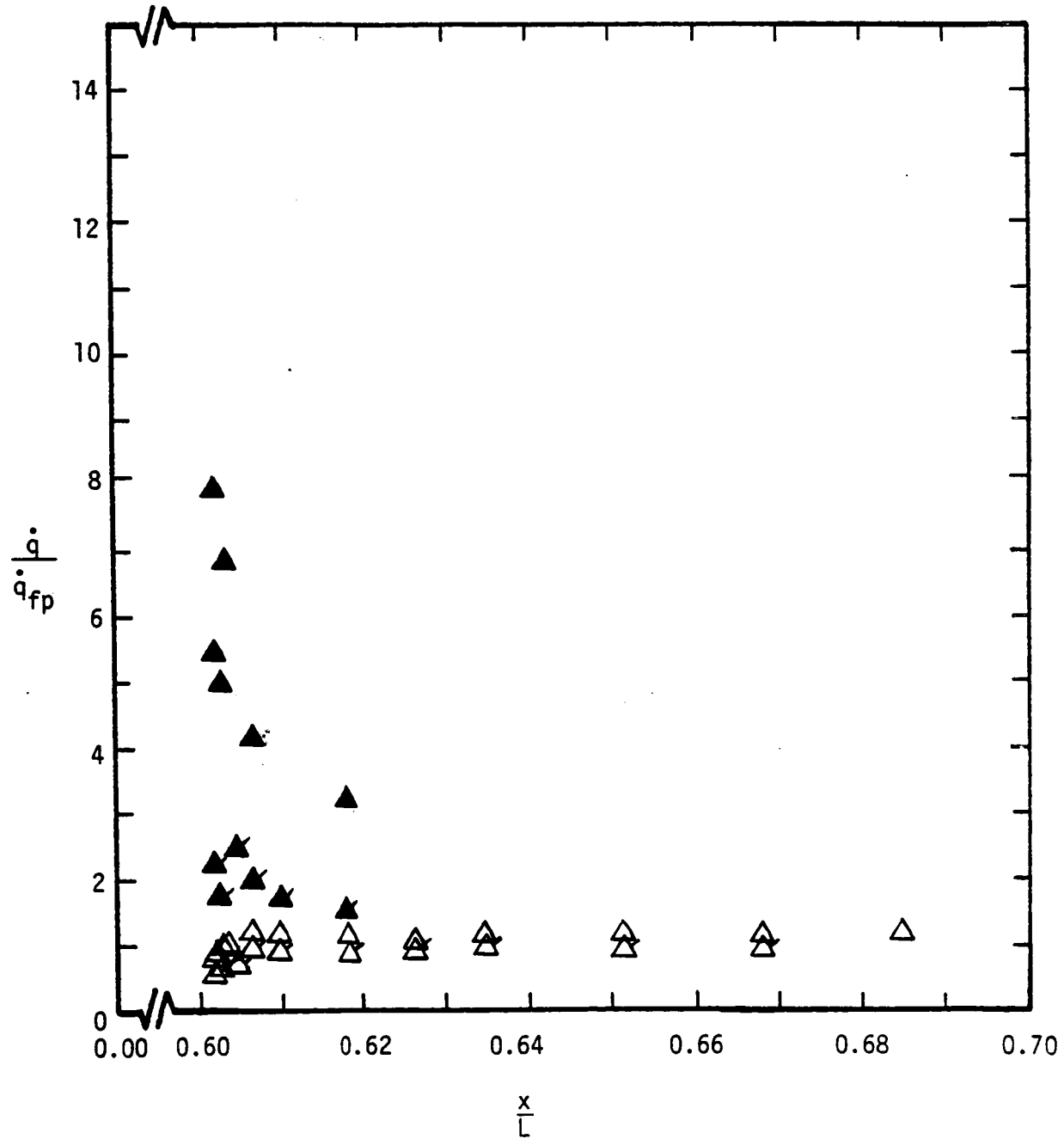


(c) $Re_{\infty,L} = 8.11 \times 10^6$

Figure 19. - Concluded.

\triangle Single, transverse gap, C2
 \blacktriangle Intersecting gap (or T), C4

Flagged symbols: $y = +0.135L$, $d = 1.016$ cm
 Unflagged symbols: $y = 0.000L$, $d = 2.032$ cm



(a) $Re_{\infty, L} = 2.57 \times 10^6$

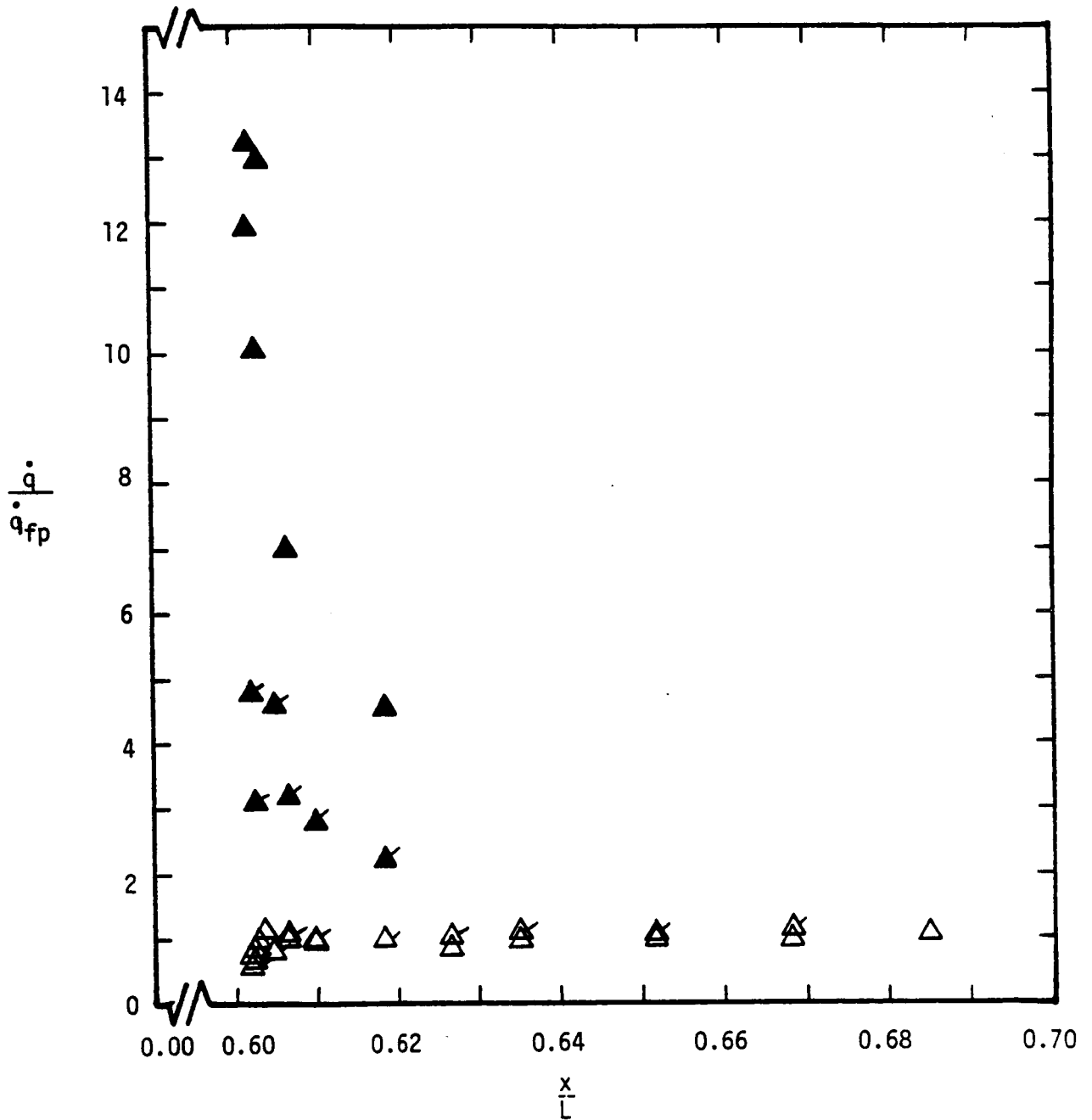
Figure 20. - A comparison of the heat-transfer-rate-ratio distributions downstream of a single, transverse gap (C2) and of a T gap (C4).

△ Single, transverse gap, C2

▲ Intersecting gap (or T), C4

Flagged symbols: $y = +0.135L$, $d = 1.016$ cm

Unflagged symbols: $y = 0.000L$, $d = 2.032$ cm

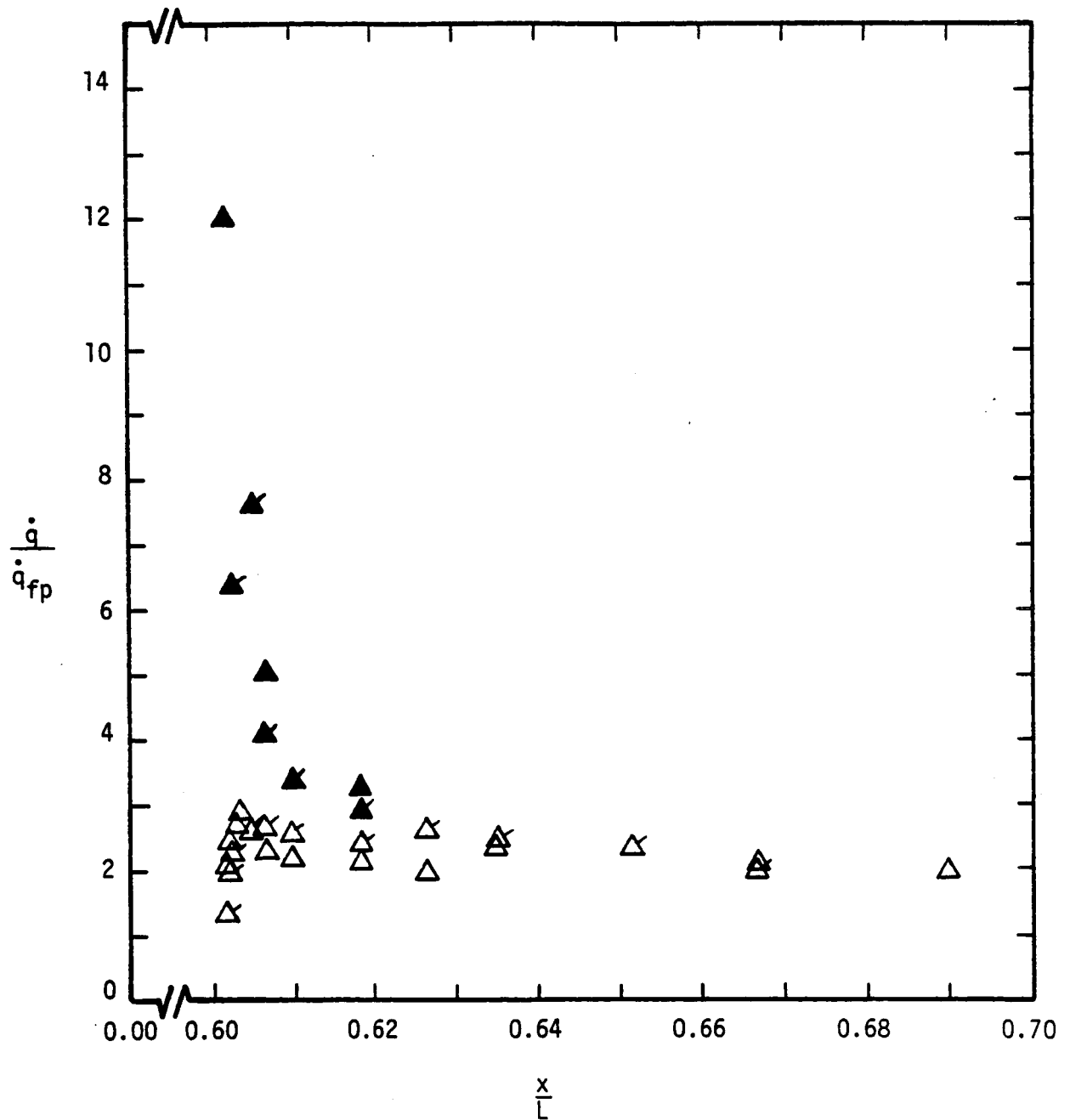


(b) $Re_{\infty, L} = 4.01 \times 10^6$

Figure 20. - Continued.

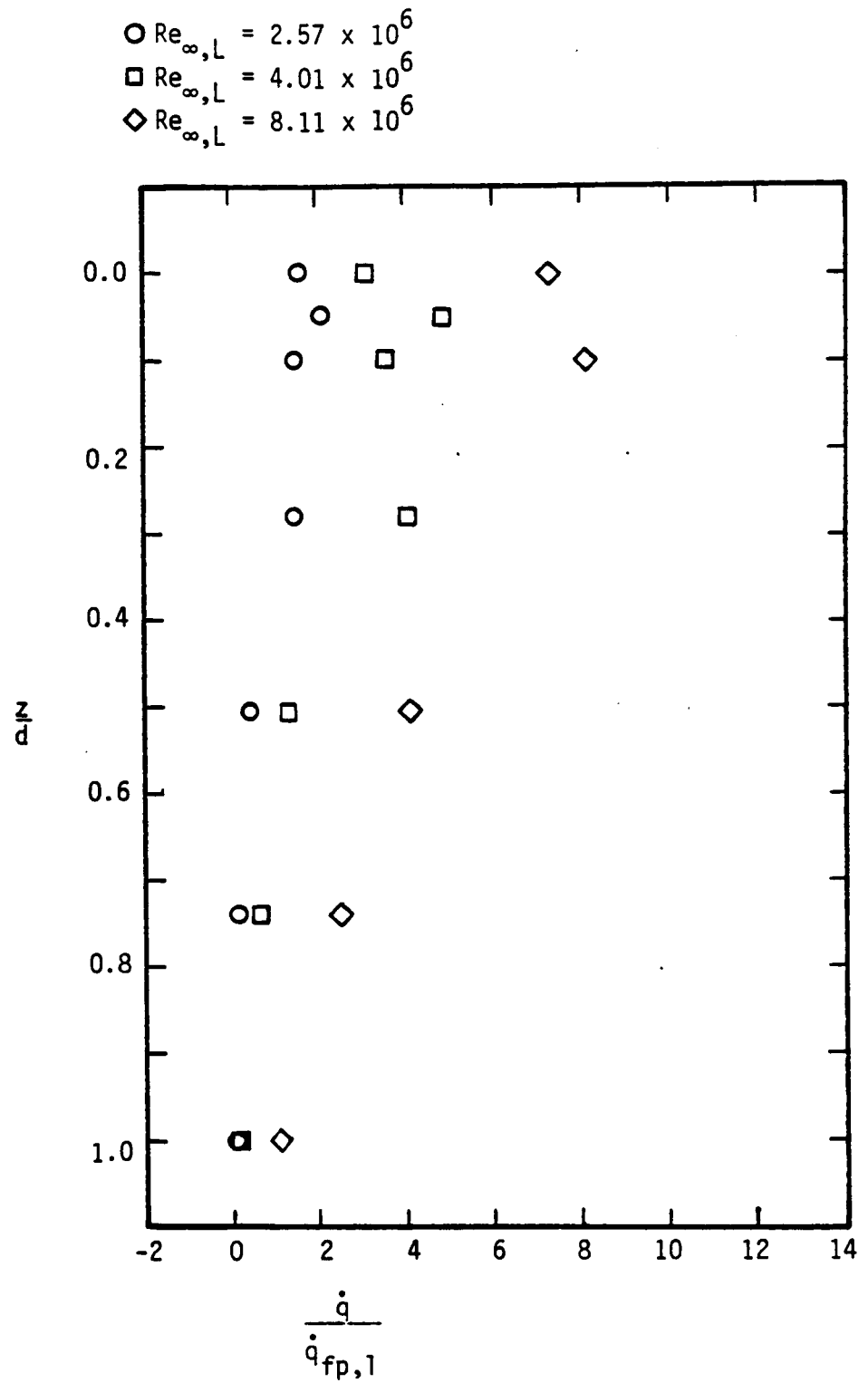
- \triangle Single, transverse gap, C2
 \blacktriangle Intersecting gap (or T), C4

Flagged symbols: $y = +0.135L$, $d = 1.016$ cm
 Unflagged symbols: $y = 0.000L$, $d = 2.032$ cm



(c) $Re_{\infty, L} = 8.11 \times 10^6$

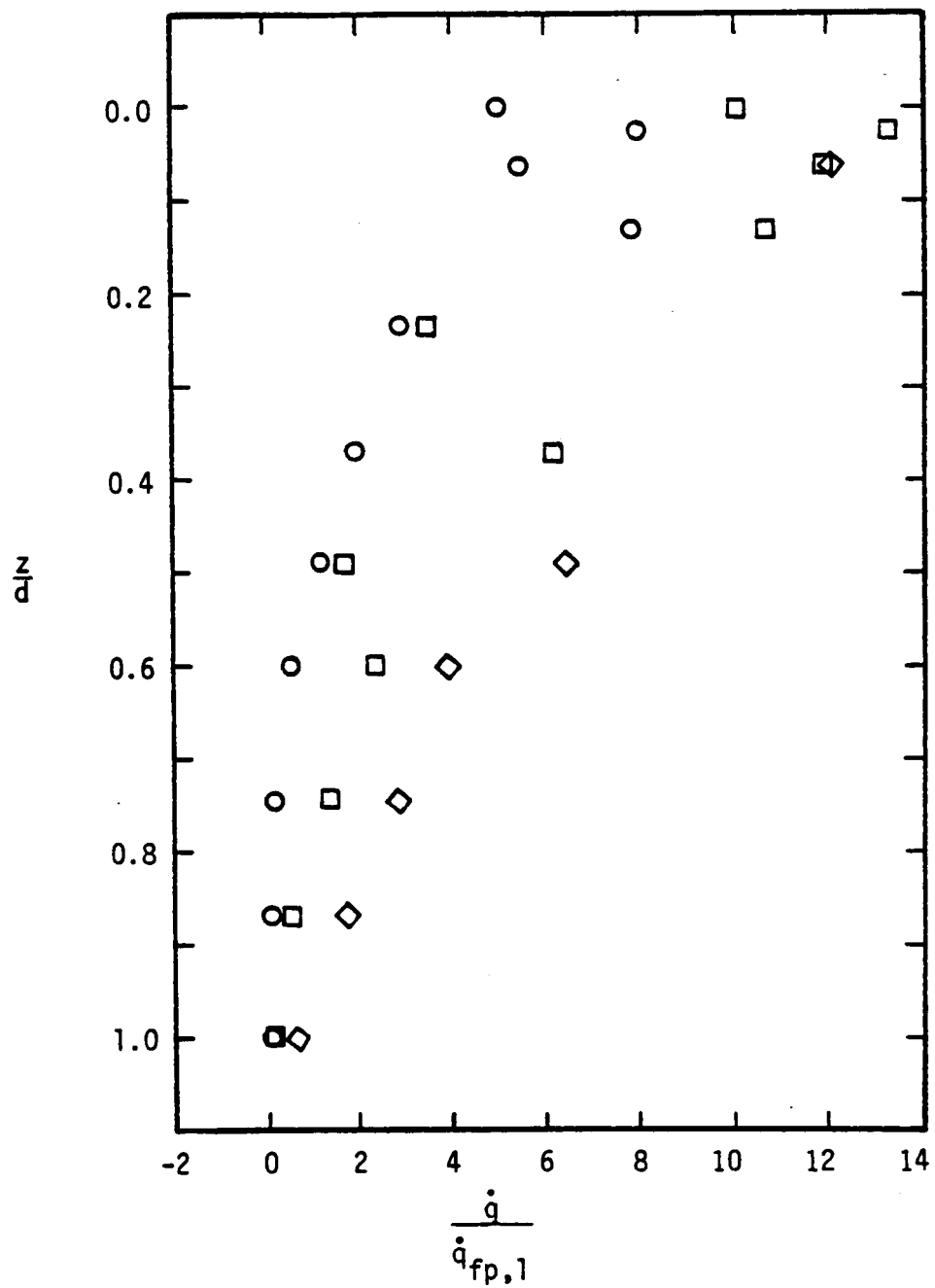
Figure 20. - Concluded.



(a) $y = +0.135L$, $d = 1.016 \text{ cm}$

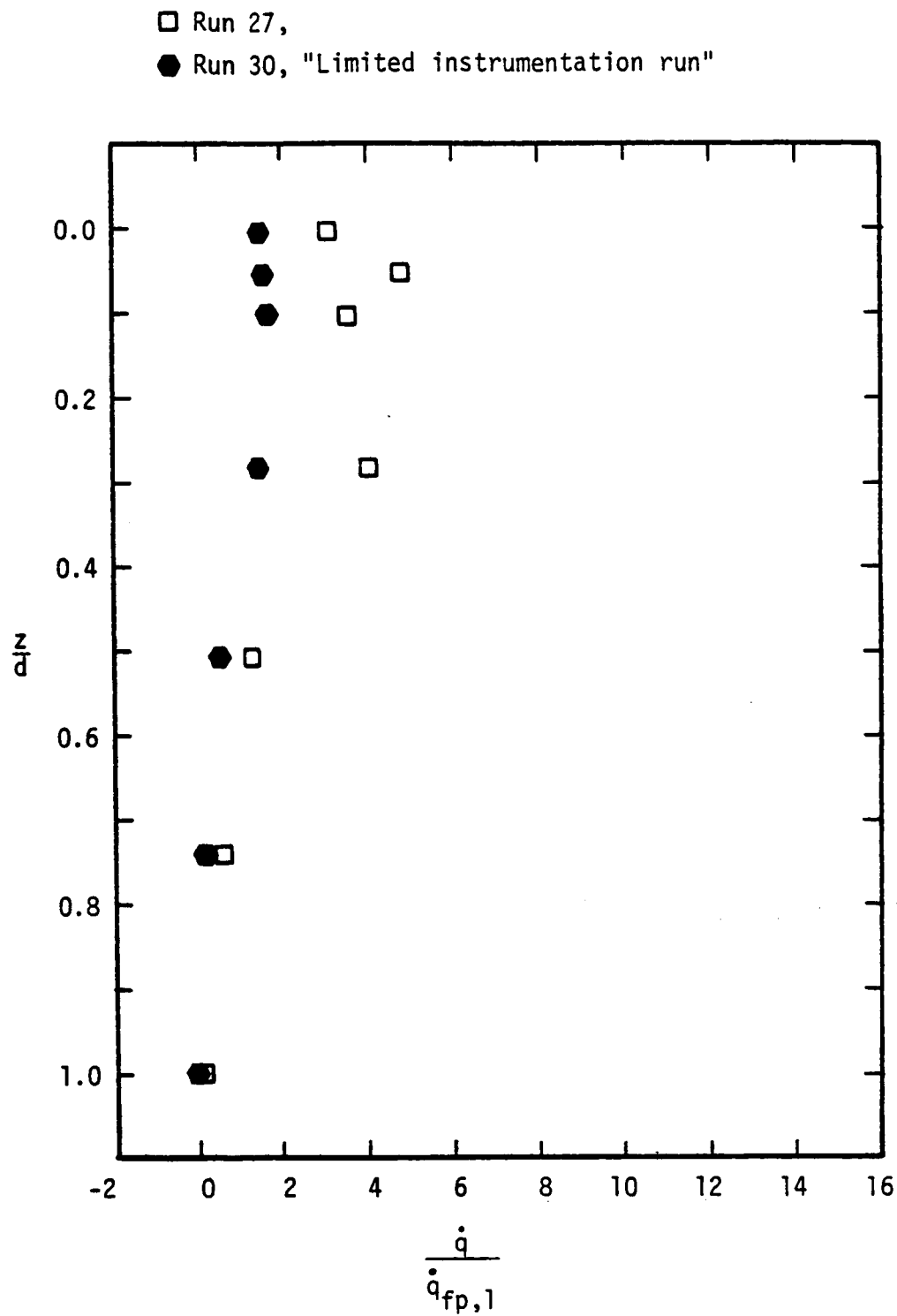
Figure 21. - Vertical heat-transfer distribution on the recompression surface of a T(C4).

$\circ \text{Re}_{\infty, L} = 2.57 \times 10^6$
 $\square \text{Re}_{\infty, L} = 4.01 \times 10^6$
 $\diamond \text{Re}_{\infty, L} = 8.11 \times 10^6$



(b) $y = +0.000L$, $d = 2.032 \text{ cm}$

Figure 21. - Concluded.

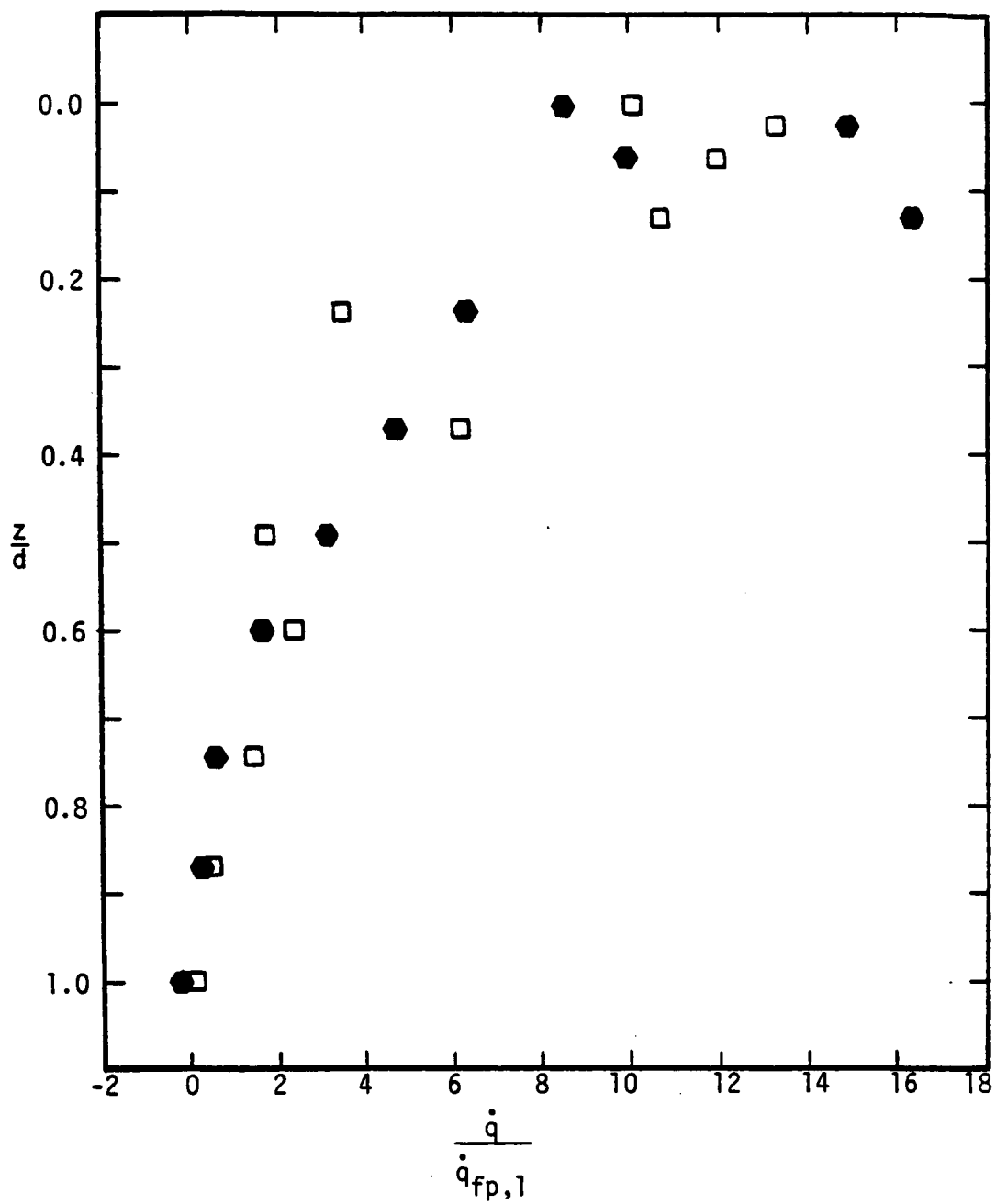


(a) $y = +0.135L$, $d = 1.016$ cm

Figure 22. - Run-to-run variations of the vertical heat-transfer distribution on the recompression surface of a T, (C4), $Re_{\infty,L} = 4.01 \times 10^6$.

□ Run 27,

● Run 30, "Limited instrumentation run"



(b) $y = 0.000L$, $d = 2.032$ cm

Figure 22. - Continued.

$Re_{\infty,L}$: $\bigcirc 2.57 \times 10^6$ $\square 4.01 \times 10^6$ $\bigcirc 5.90 \times 10^6$ $\diamond 8.11 \times 10^6$

open symbols: $y = +0.135L$, $d = 1.016$ cm

filled symbols: $y = +0.000L$, $d = 2.032$ cm

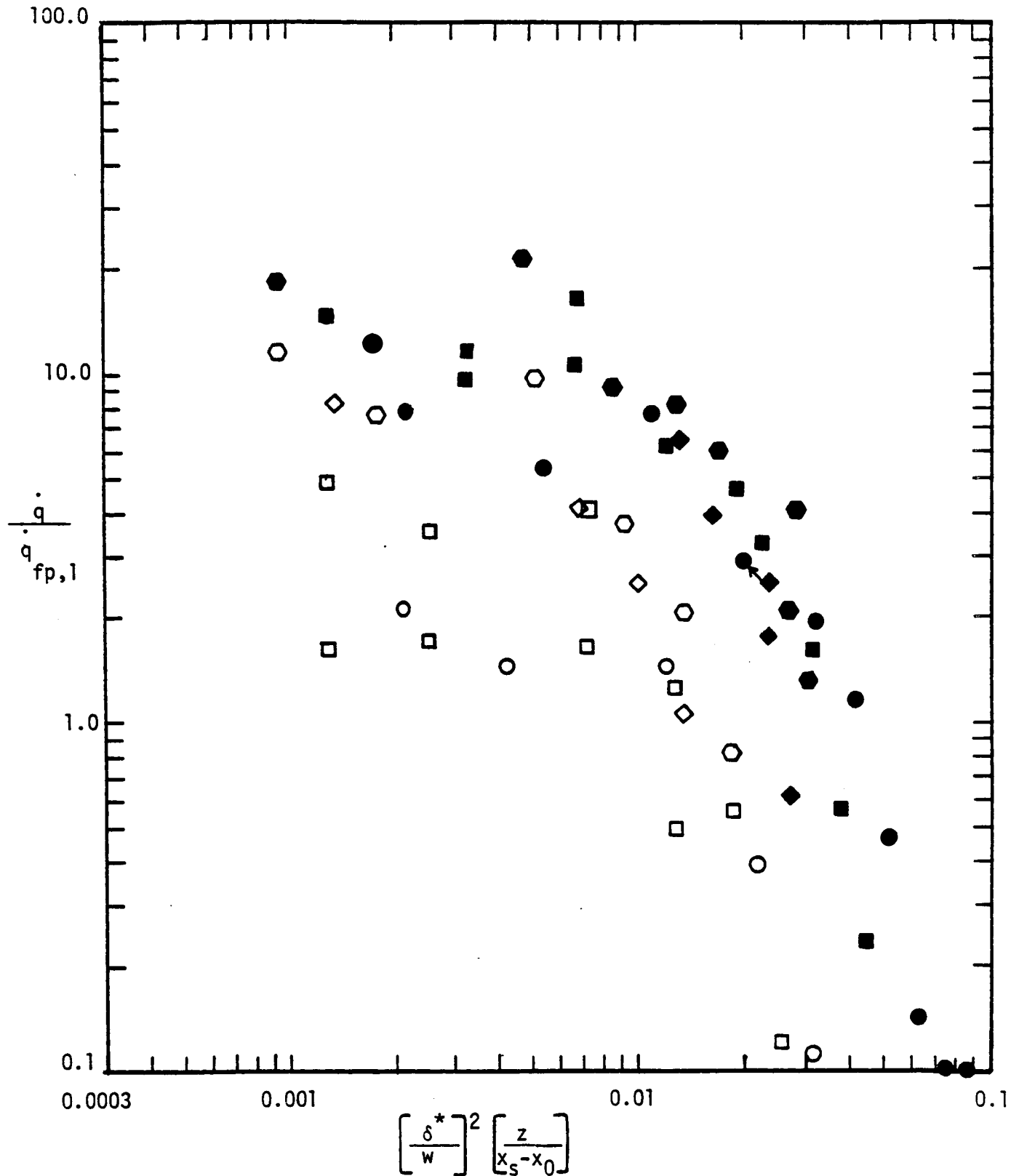


Figure 23. - Correlation of heat-transfer rates on the recompression surface.

$Re_{\infty,L}$: $\bigcirc 2.57 \times 10^6$ $\square 4.01 \times 10^6$ $\bigcirc 5.90 \times 10^6$ $\diamond 8.11 \times 10^6$

open symbols: $y = +0.135L$, $d = 1.016$ cm

filled symbols: $y = +0.000L$, $d = 2.032$ cm

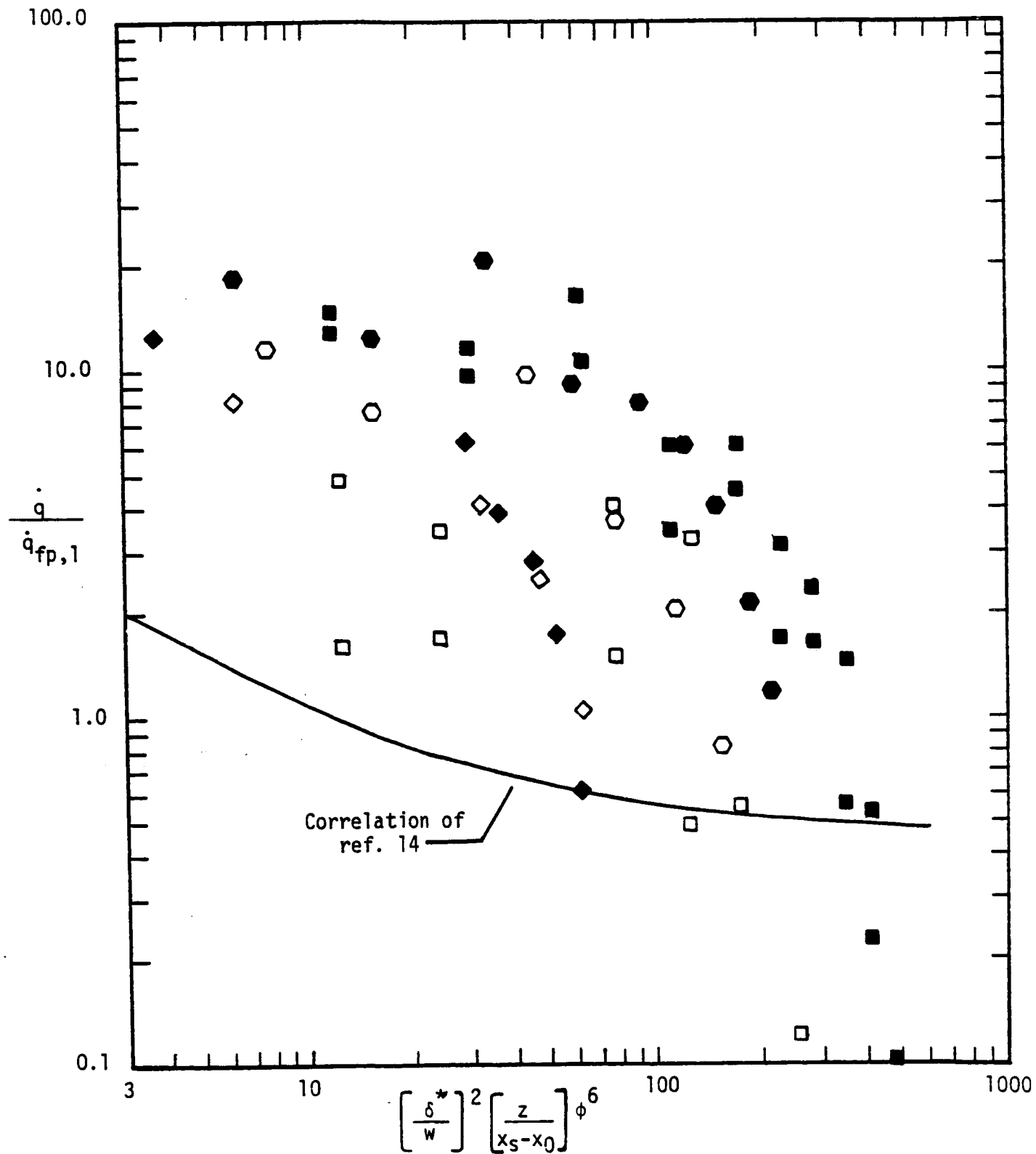


Figure 23. - Concluded.

Data: $\Delta y = +0.135L$, $d = 1.016$ cm

O $y = 0.000L$, $d = 2.032$ cm

Filled symbols are for limited instrumentation runs

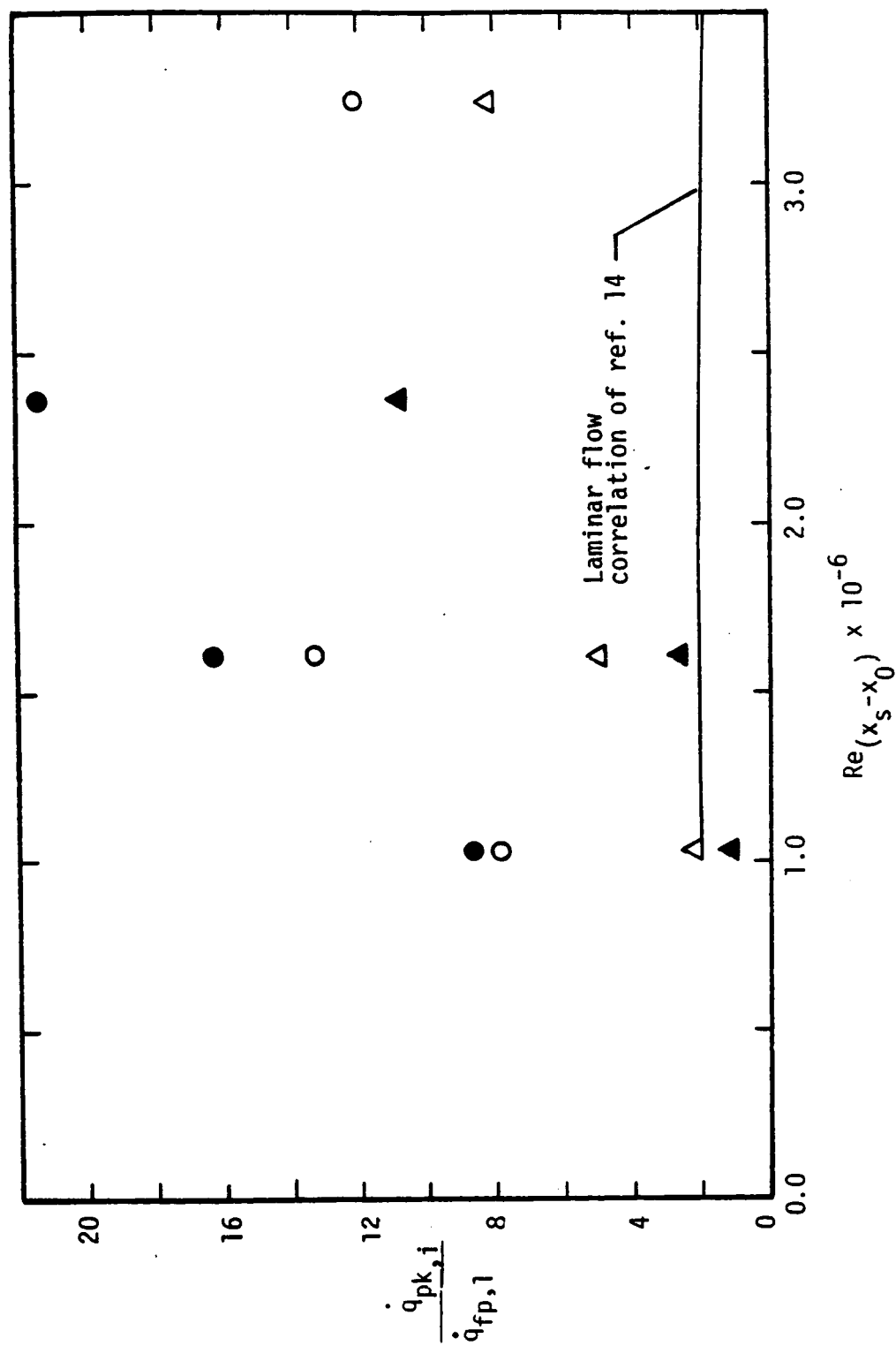


Figure 24. - Maximum value of the heating-rate ratio measured on the recompression surface of a T (C4).

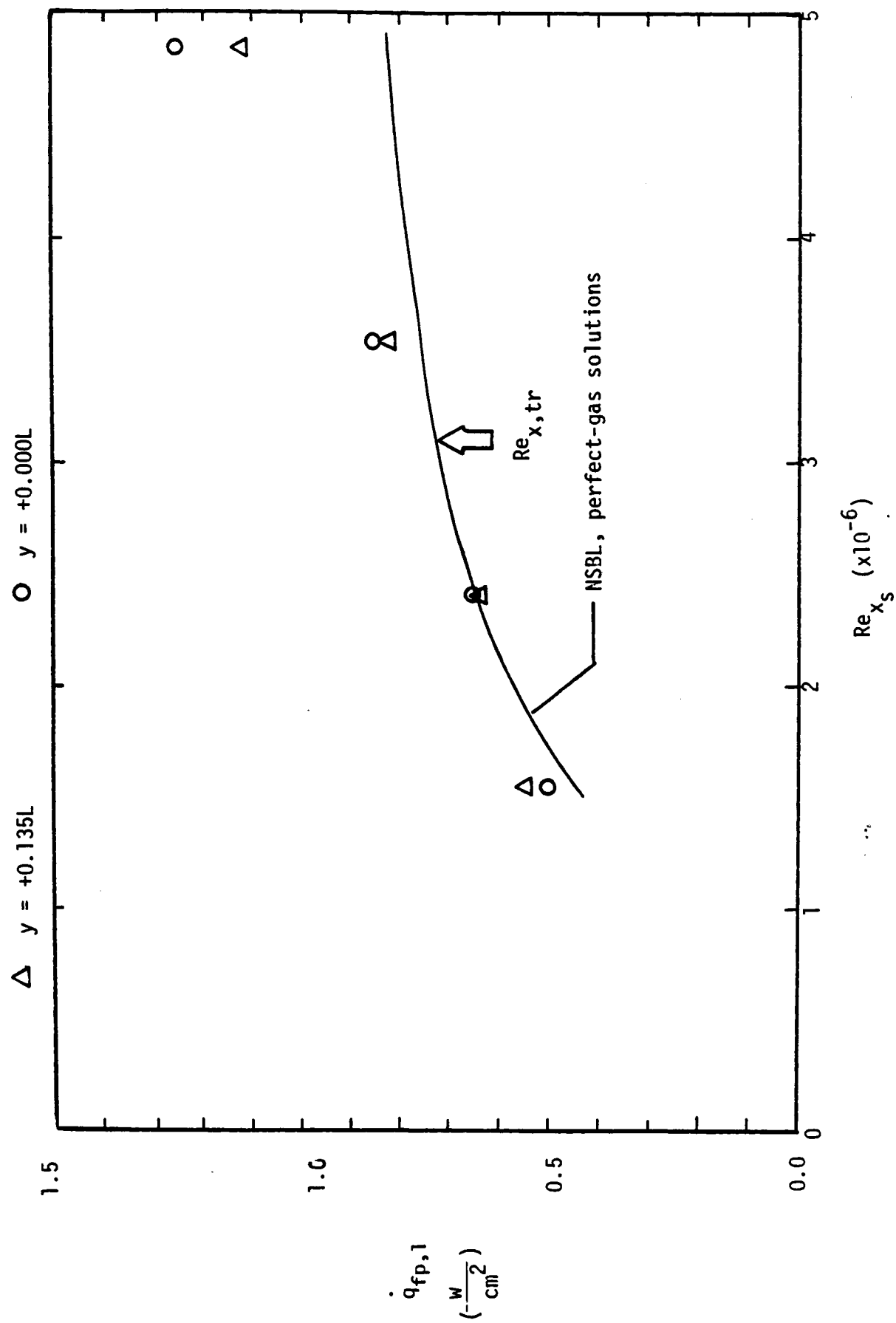
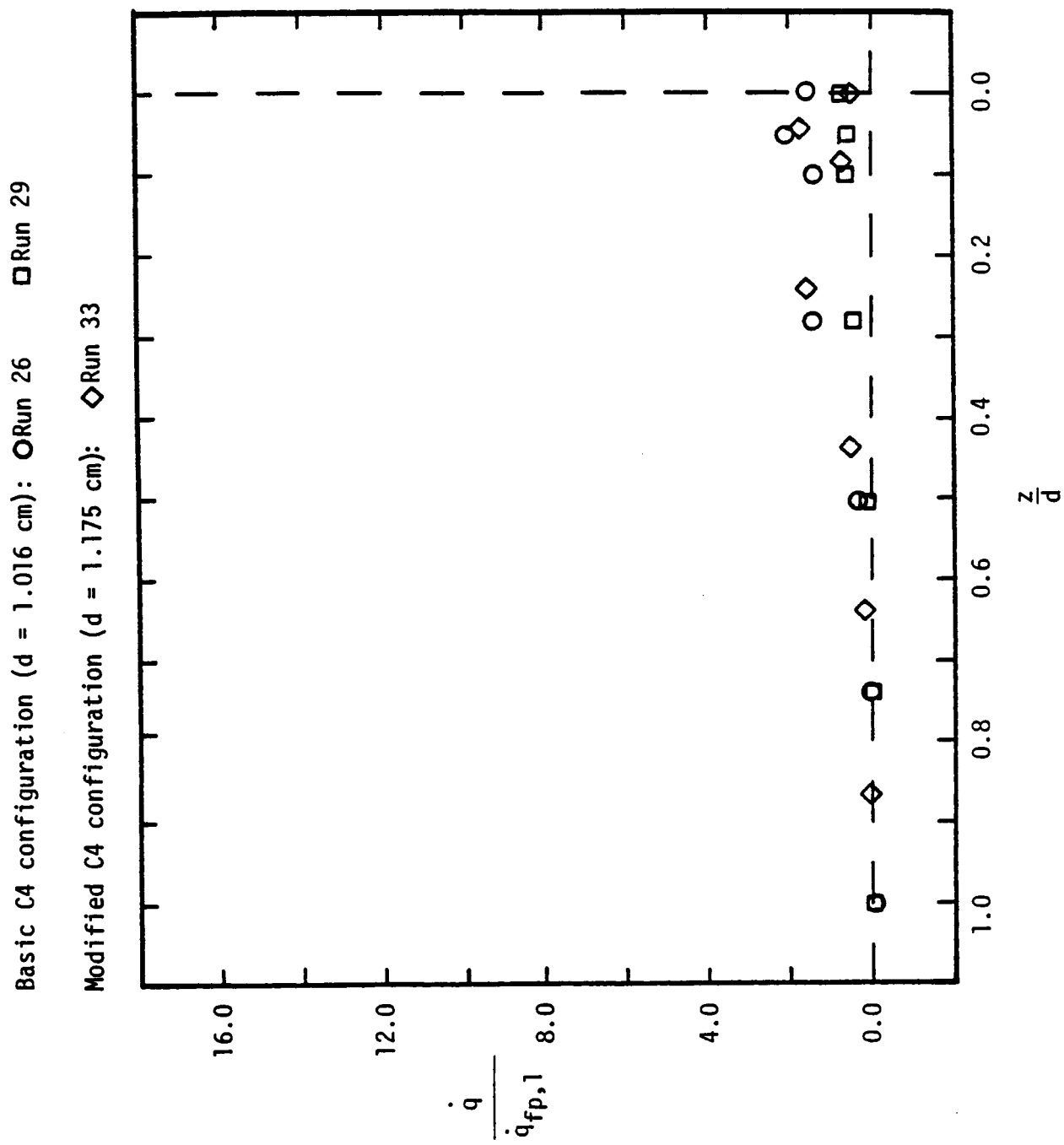
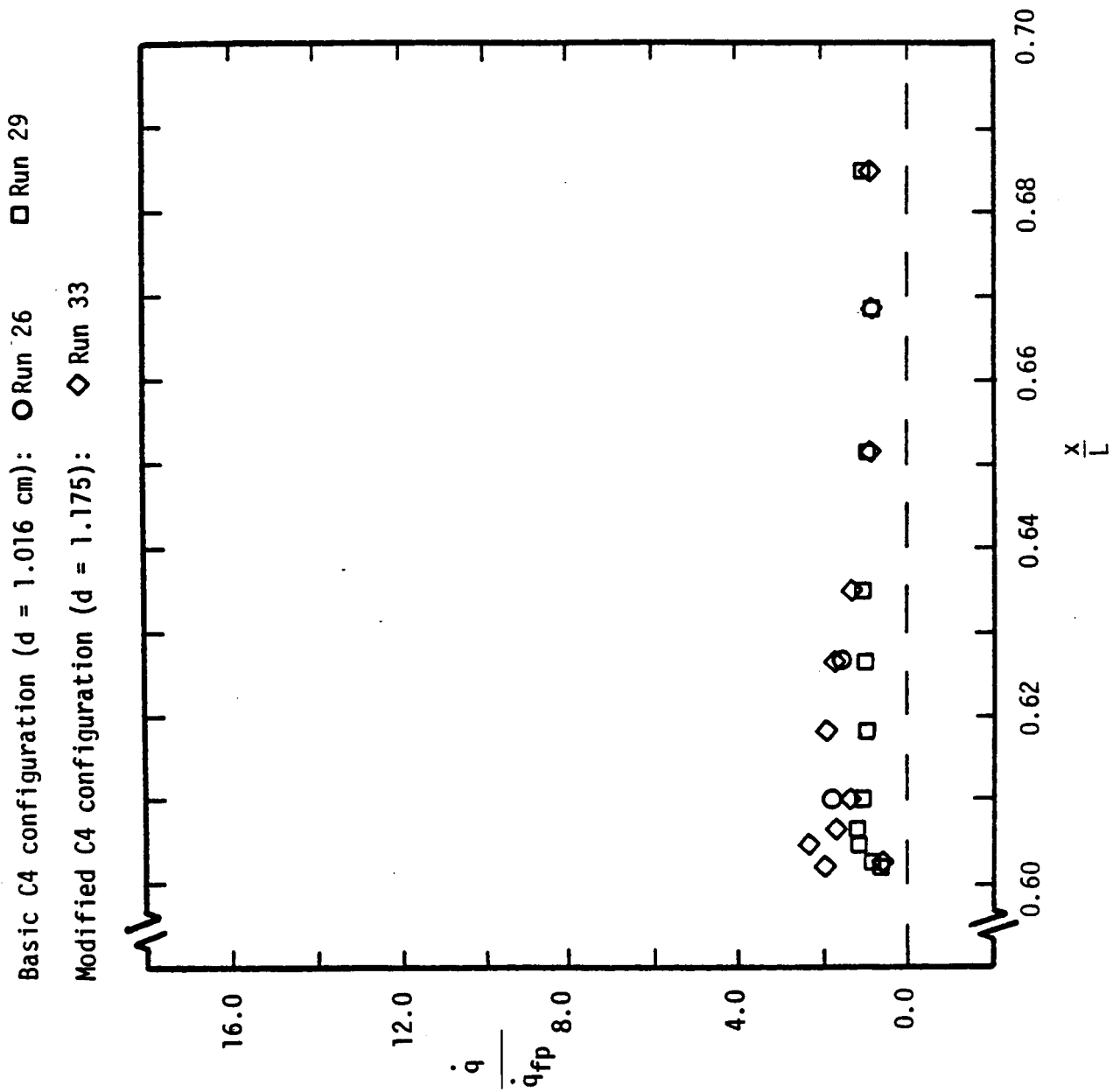


Figure 25. The experimental heat-transfer rates at $x = 0.6L$ for the flat-plate configuration (C1).

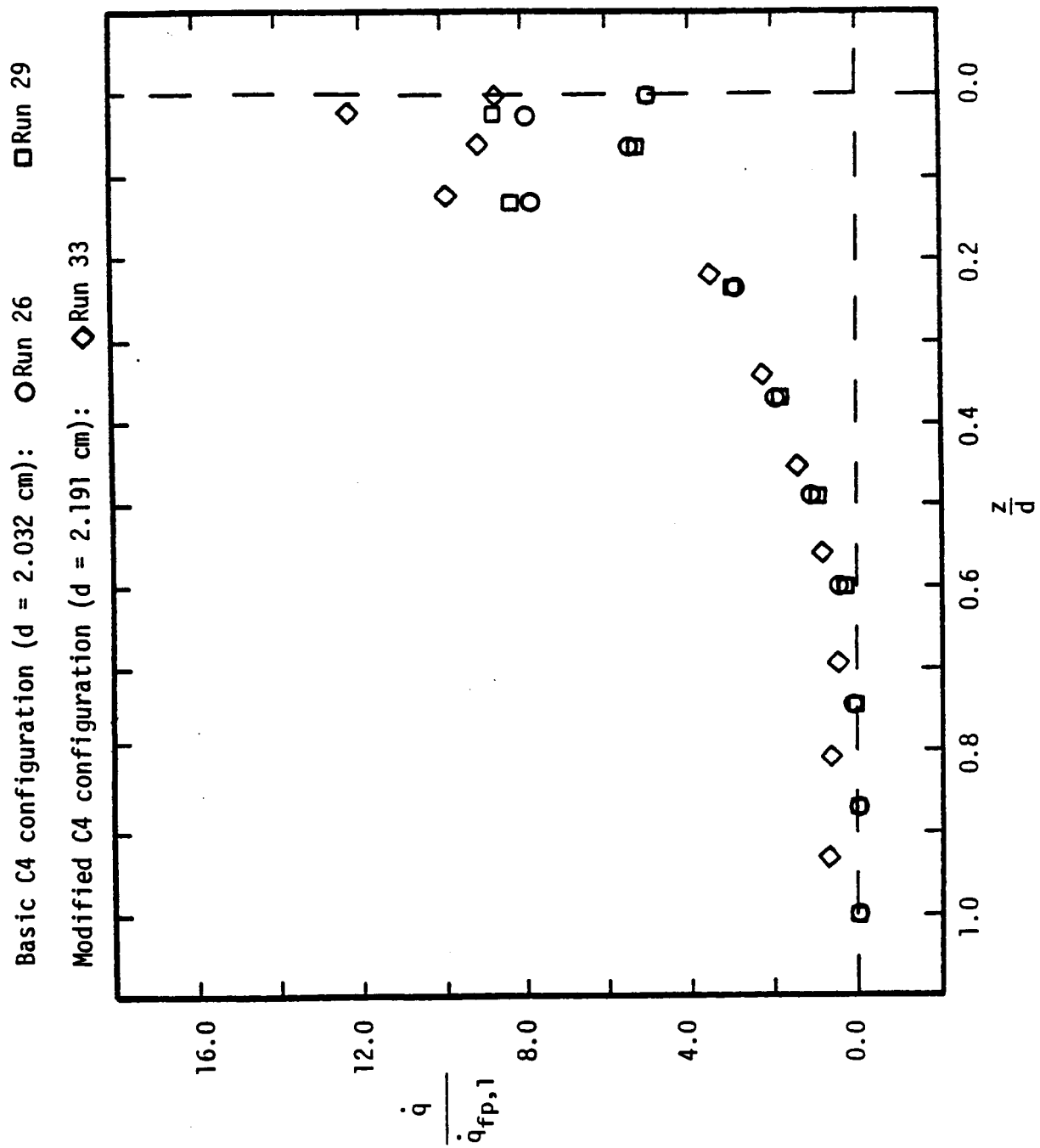


(a) For the vertical recompression surface

Figure 26. - The heat-transfer distribution downstream of a T, $y = +0.135L$, $Re_{\infty,L} = 2.57 \times 10^6$.

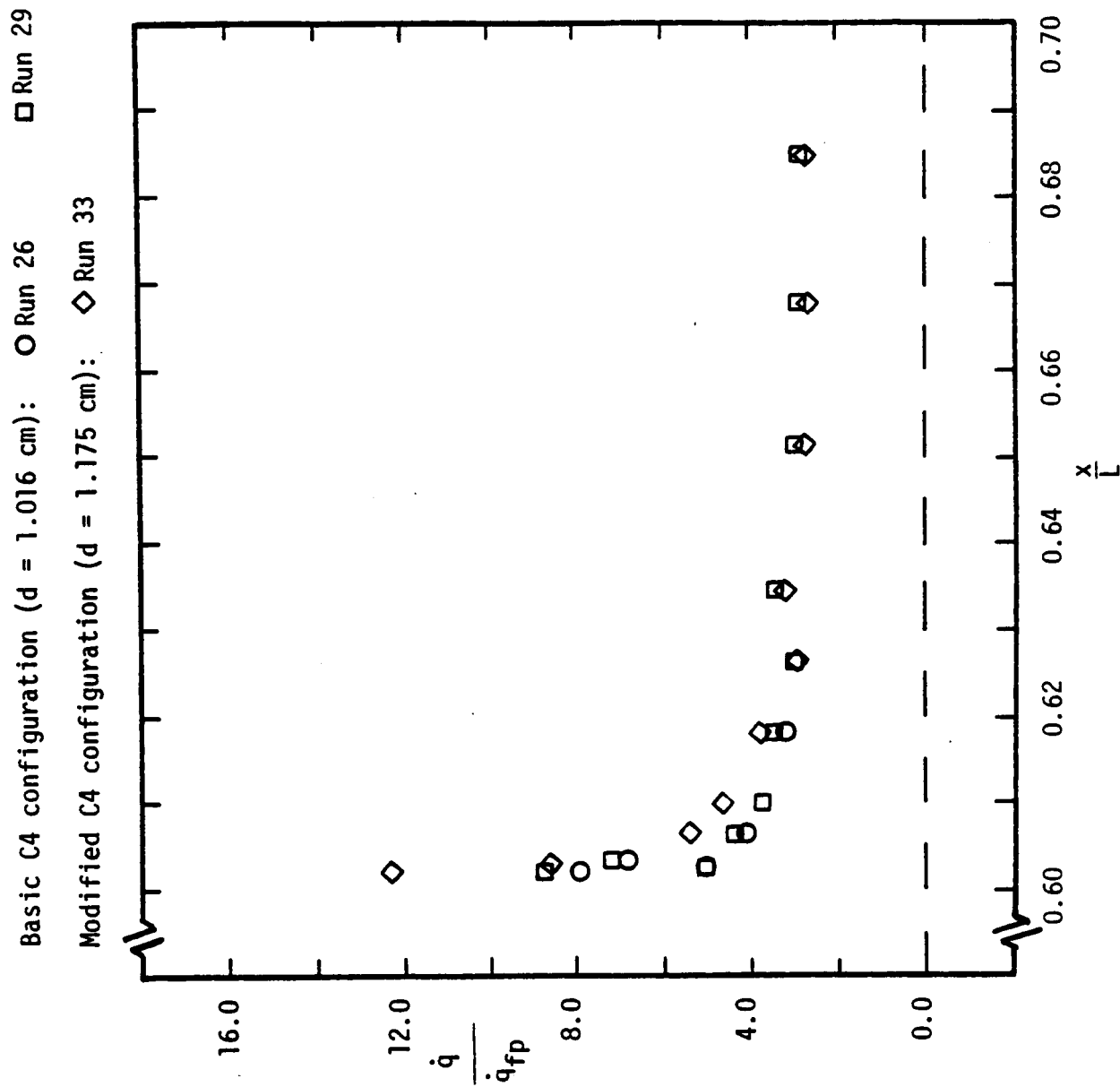


(b) On the horizontal surface of the recompression step

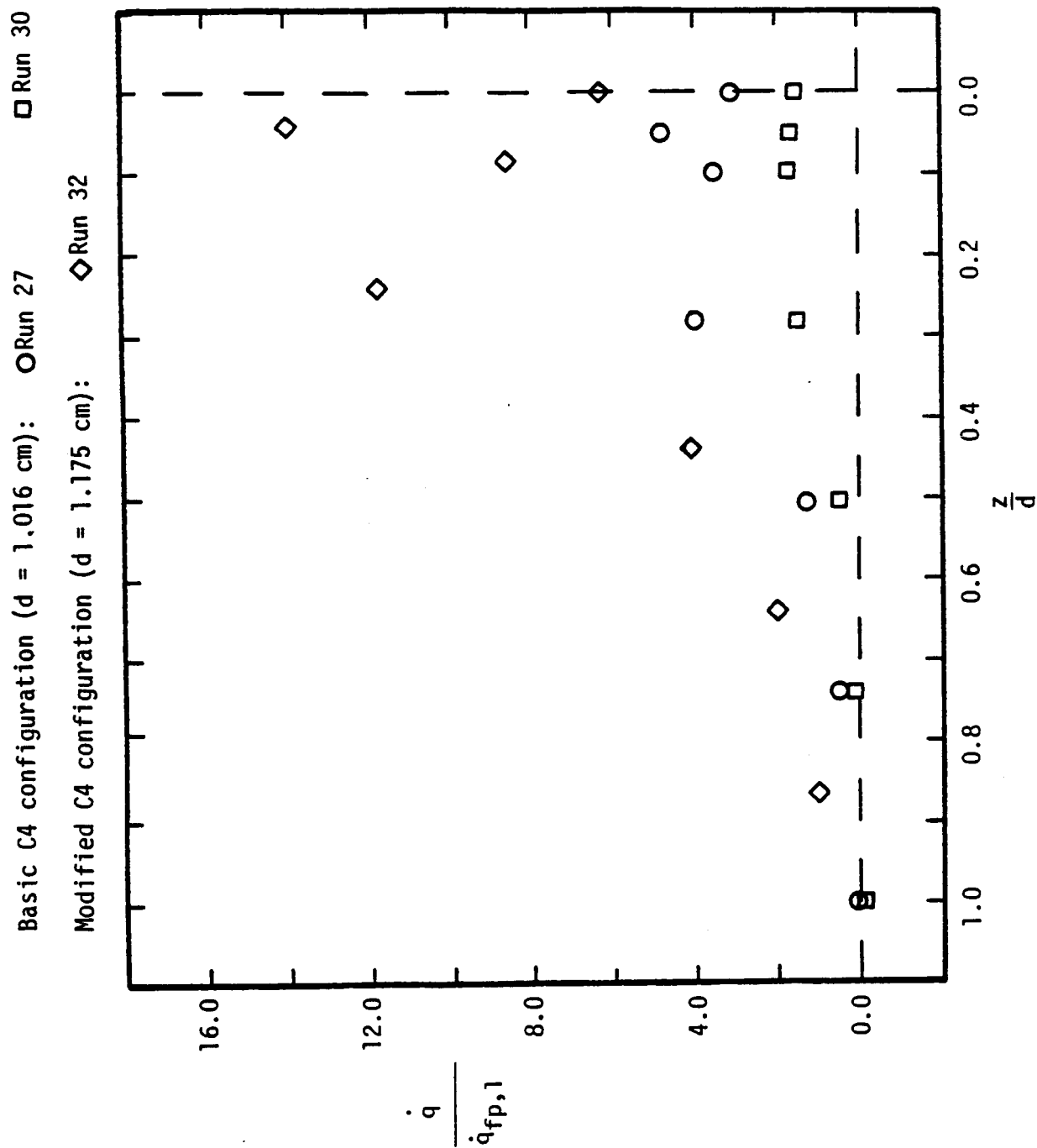


(a) For the vertical recompression surface

Figure 27. - The heat-transfer distribution downstream of a T, $y = 0.000L$, $Re_{\infty,L} = 2.57 \times 10^6$.



(b) On the horizontal surface of the recompression step

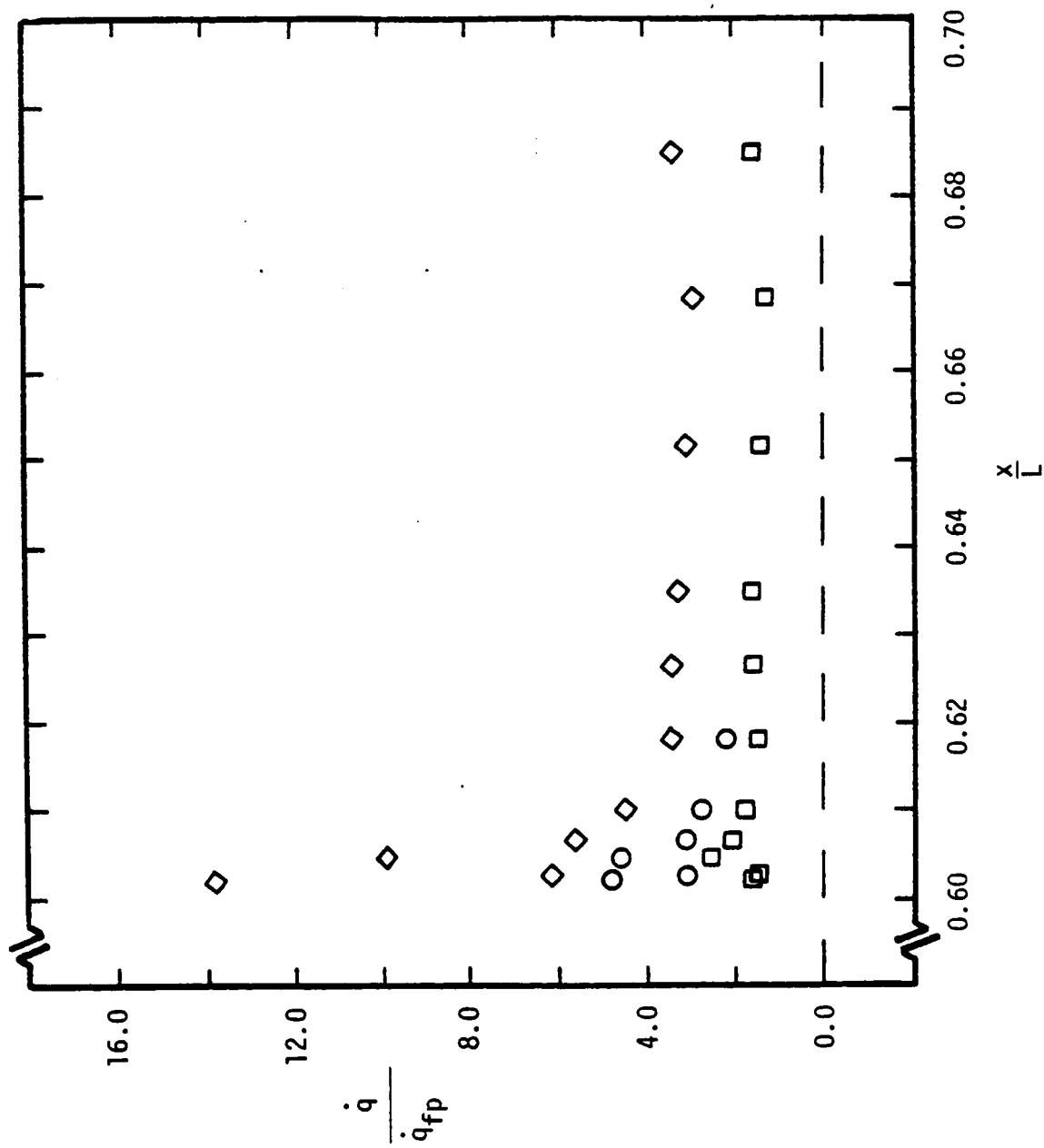


(a) For the vertical recompression surface

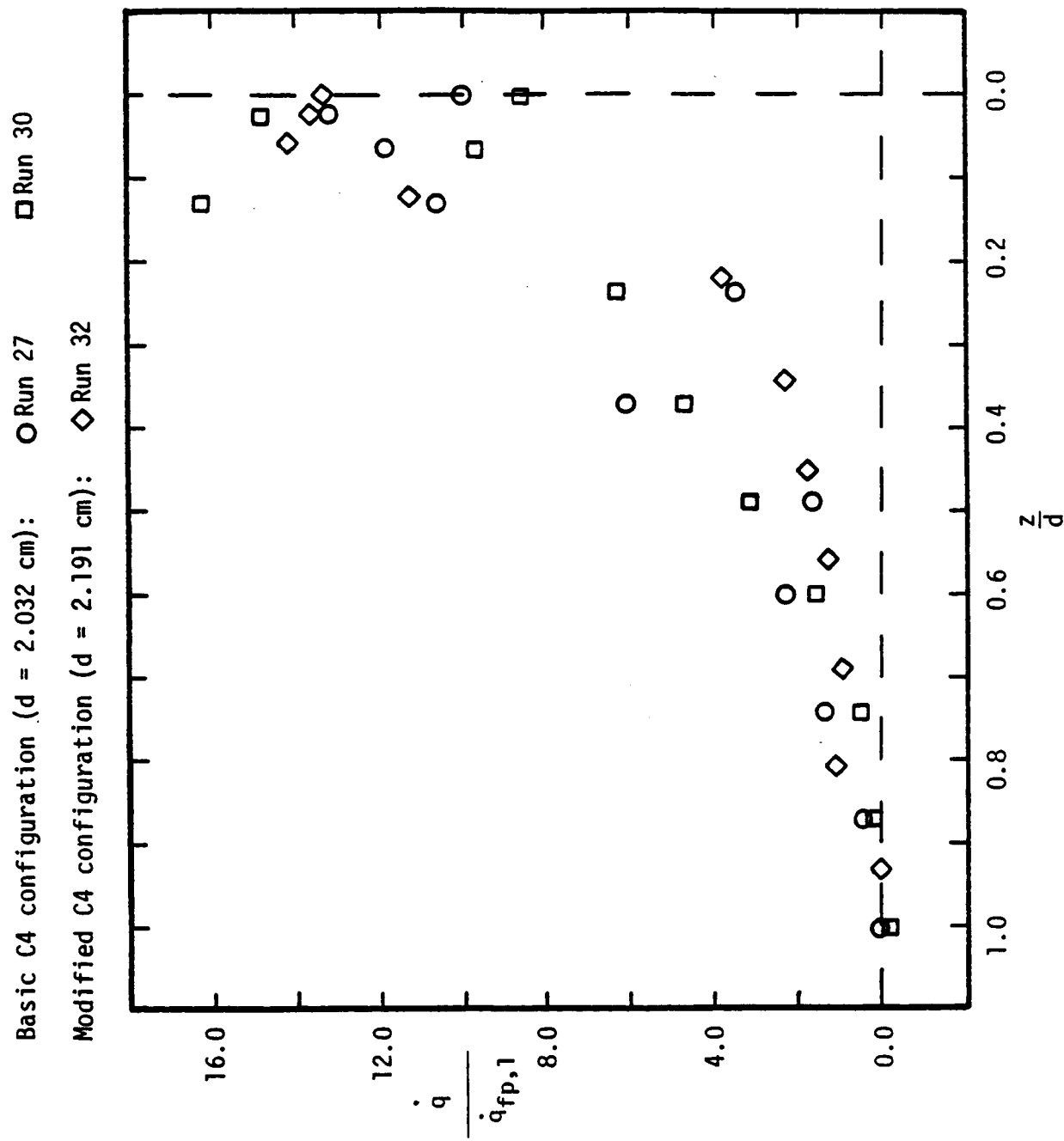
Figure 28. - The heat-transfer distribution downstream of a T, $y = +0.135L$, $Re_{\infty,L} = 4.01 \times 10^6$.

Basic C4 configuration ($d = 1.016$ cm): \circ Run 27 \square Run 30

Modified C4 configuration ($d = 1.175$ cm): \diamond Run 32

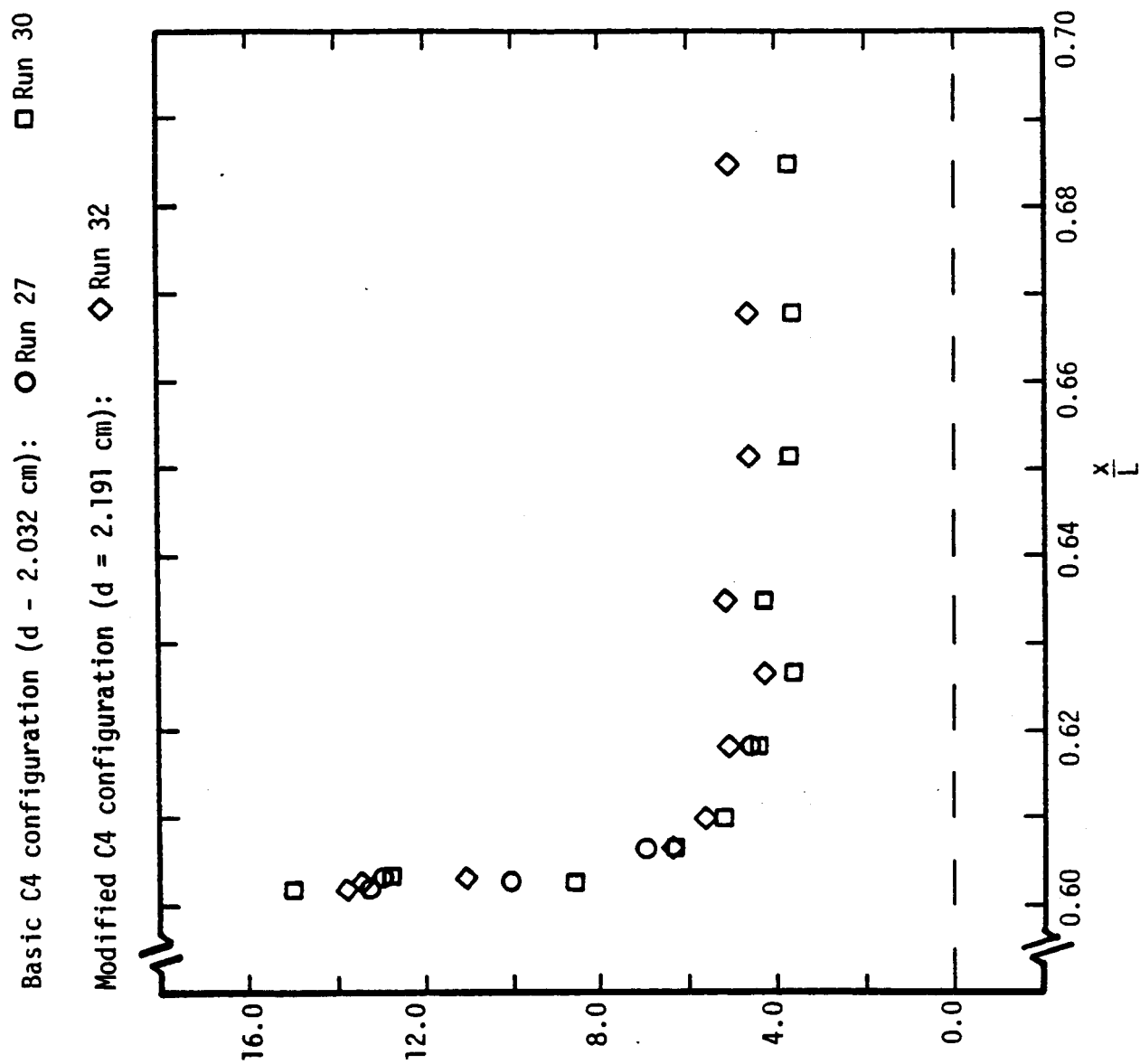


(b) On the horizontal surface of the recompression step



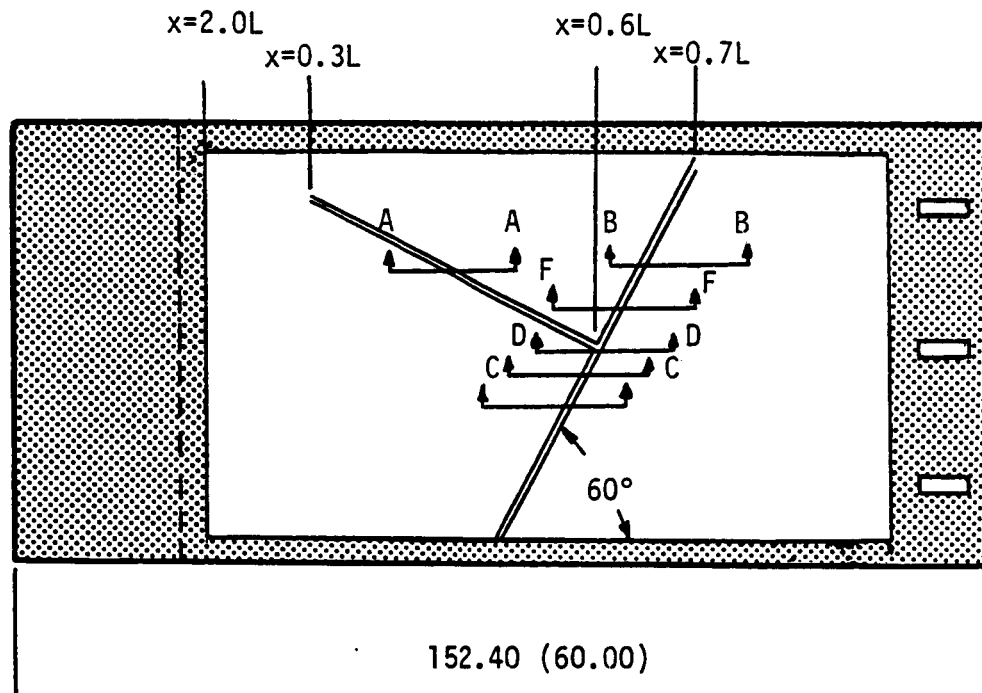
(a) For the vertical recompression surface

Figure 29. - The heat-transfer distribution downstream of a T, $y = 0.000L$, $Re_{\infty,L} = 4.01 \times 10^6$



(b) On the horizontal surface of the recompression step

Figure 29. - Concluded.



(a) Sketch of entire configuration

Figure 30. - Sketch of the insert with diagonal, intersecting gaps placed in the structural carrier plate to form Configuration 5(C5).

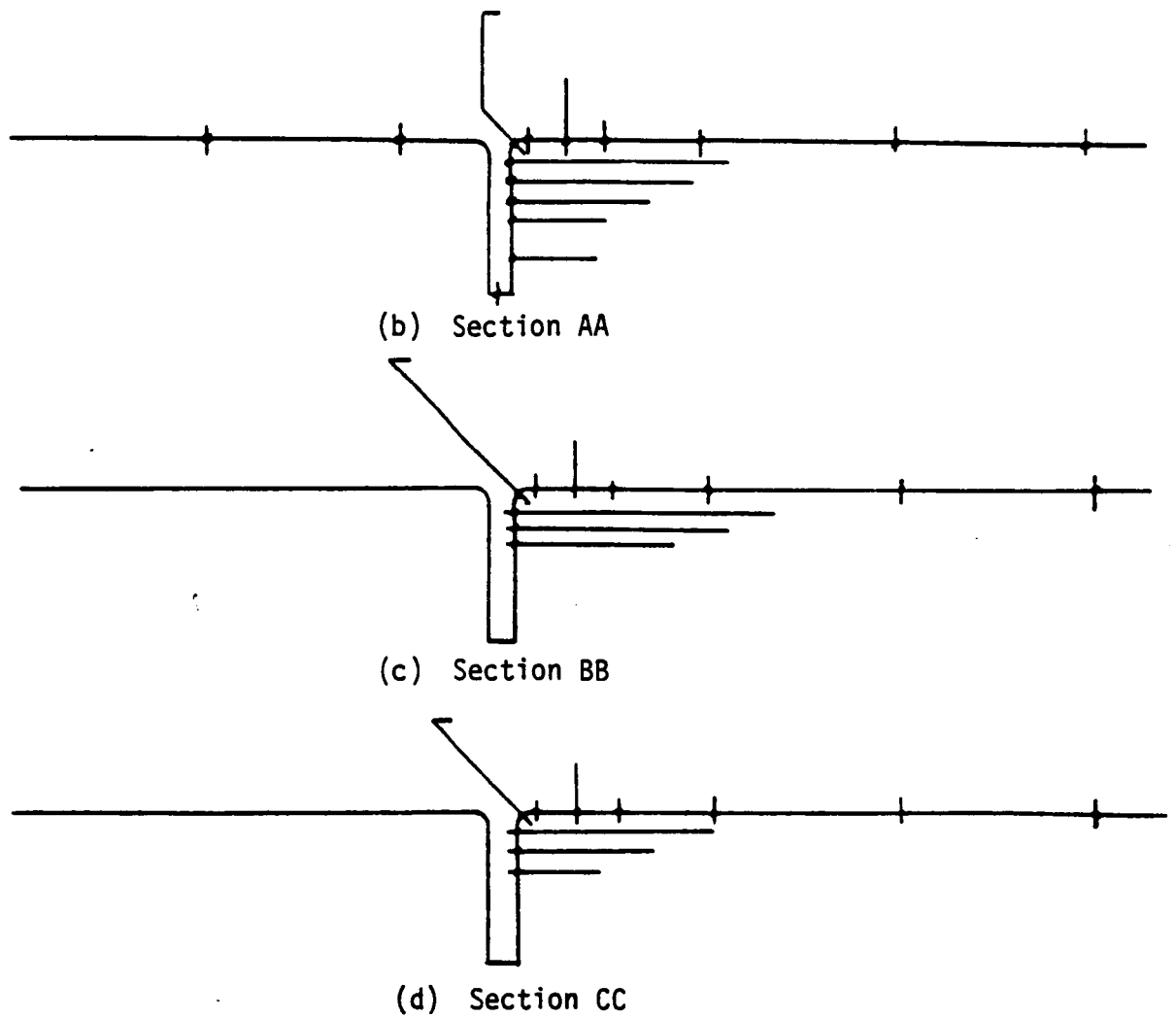
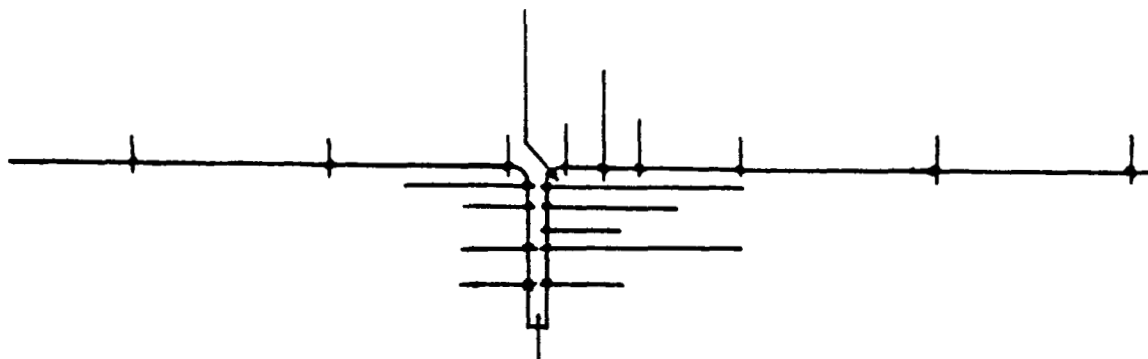
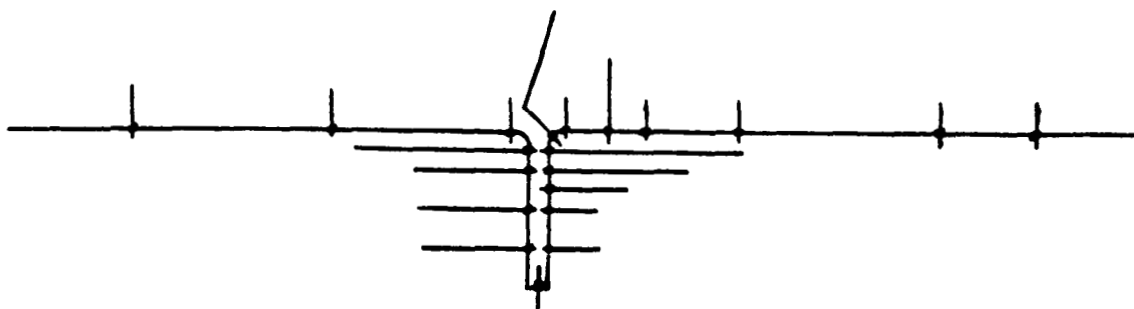


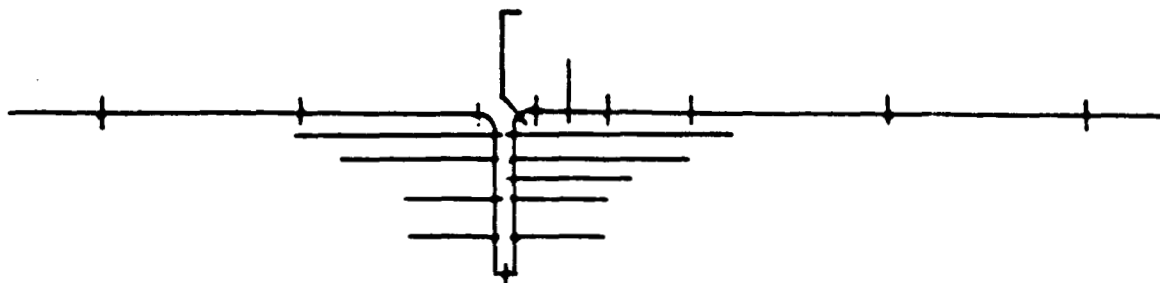
Figure 30. - Continued.



(e) Section DD



(f) Section EE



(g) Section FF

Figure 30. - Concluded.

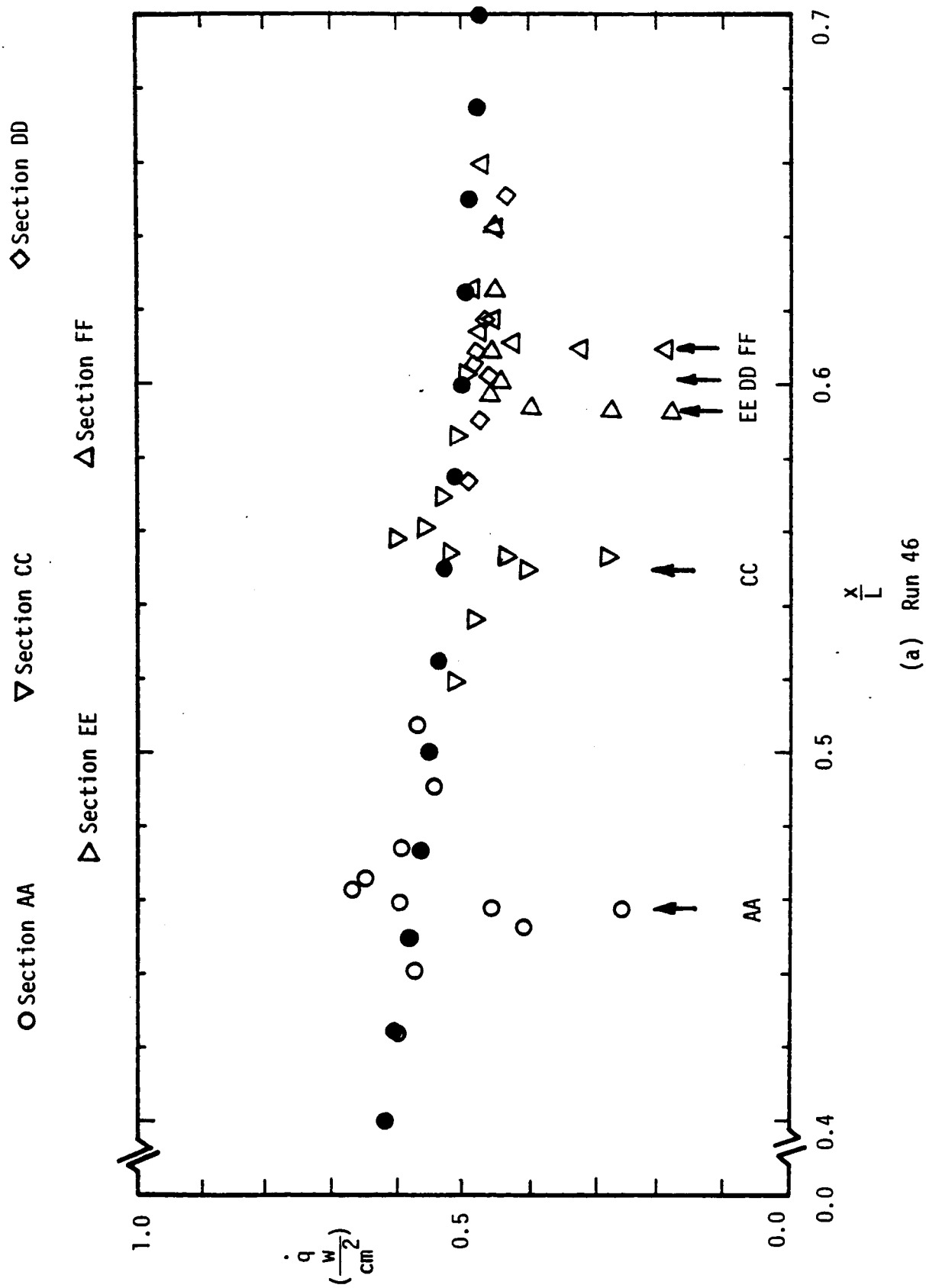
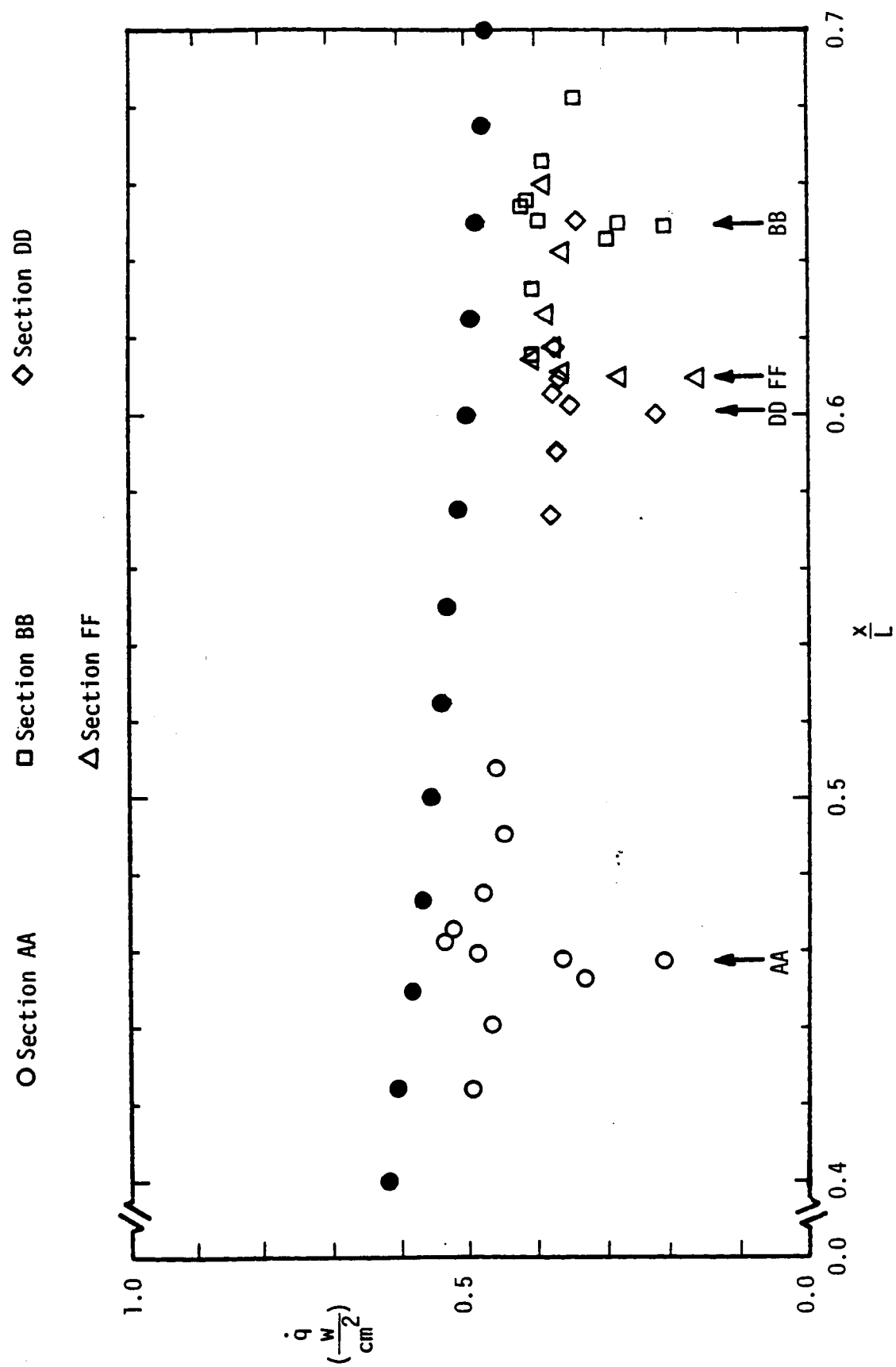
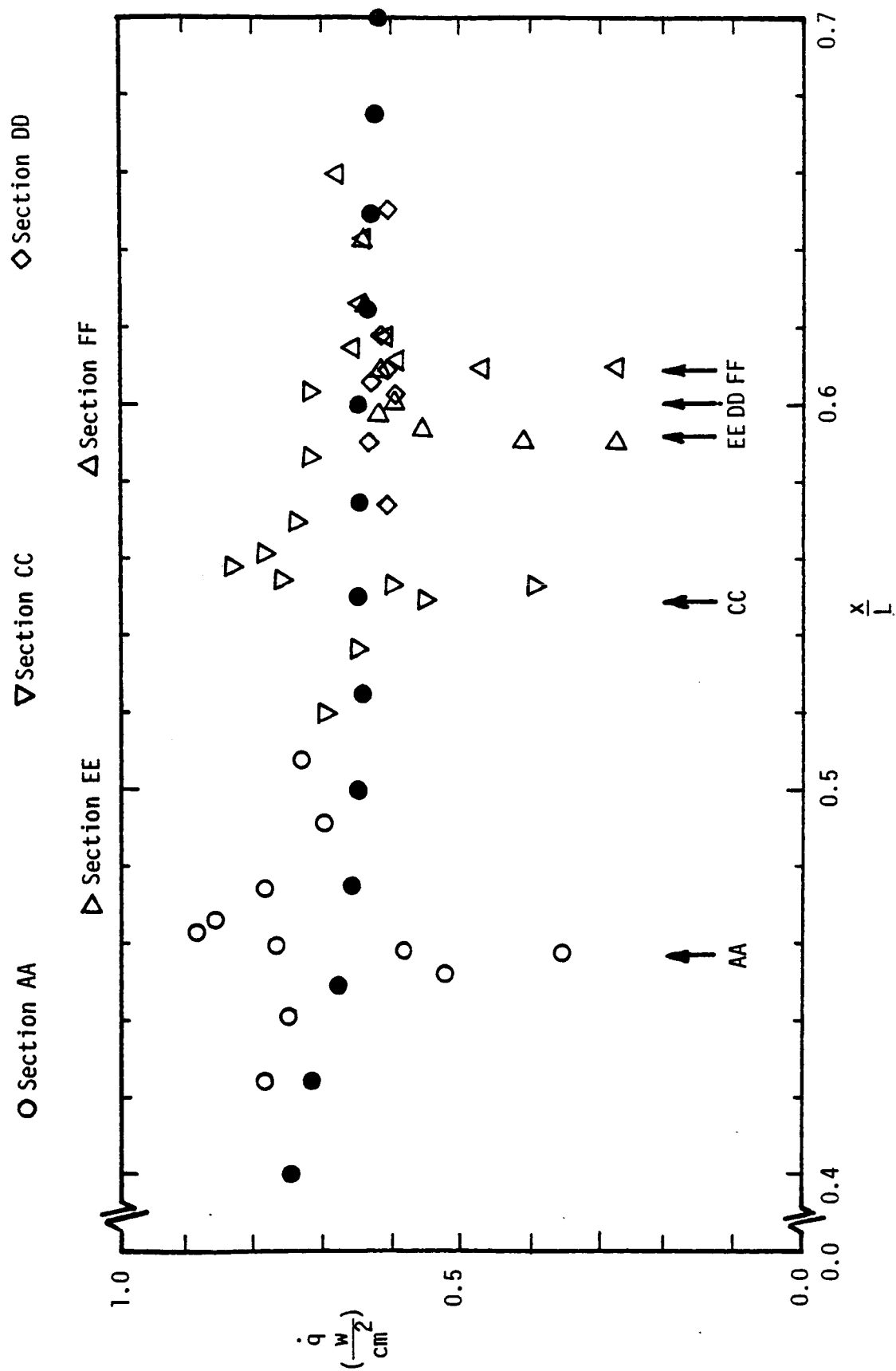


Figure 31. - The heat-transfer distribution in the vicinity of the diagonal, intersecting gaps of C5, $Re_{\infty, L} = 2.57 \times 10^6$. Filled symbols are for the flat plate (C1) at the same flow conditions (Run 38).



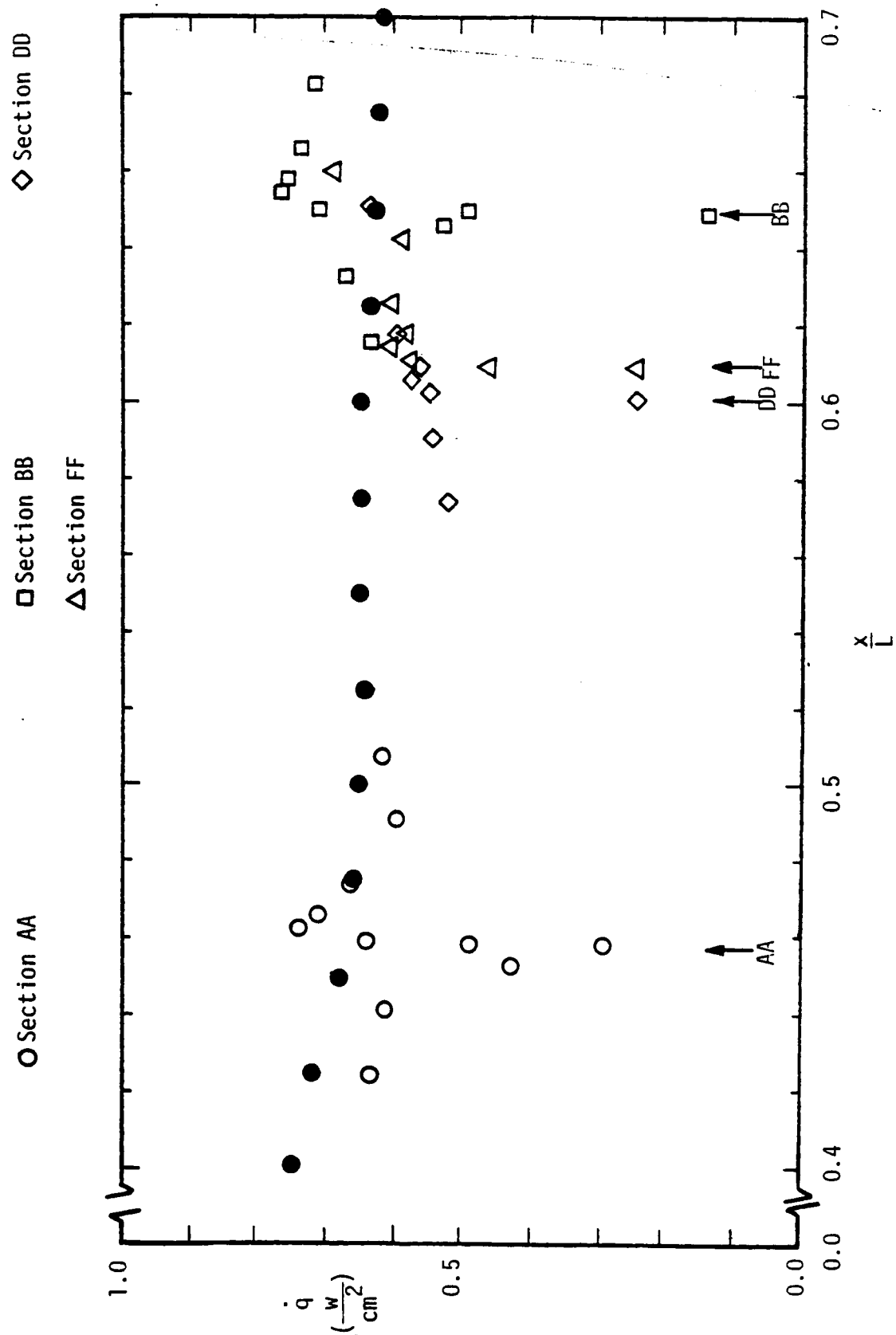
(b) Run 50

Figure 31 . - Concluded.



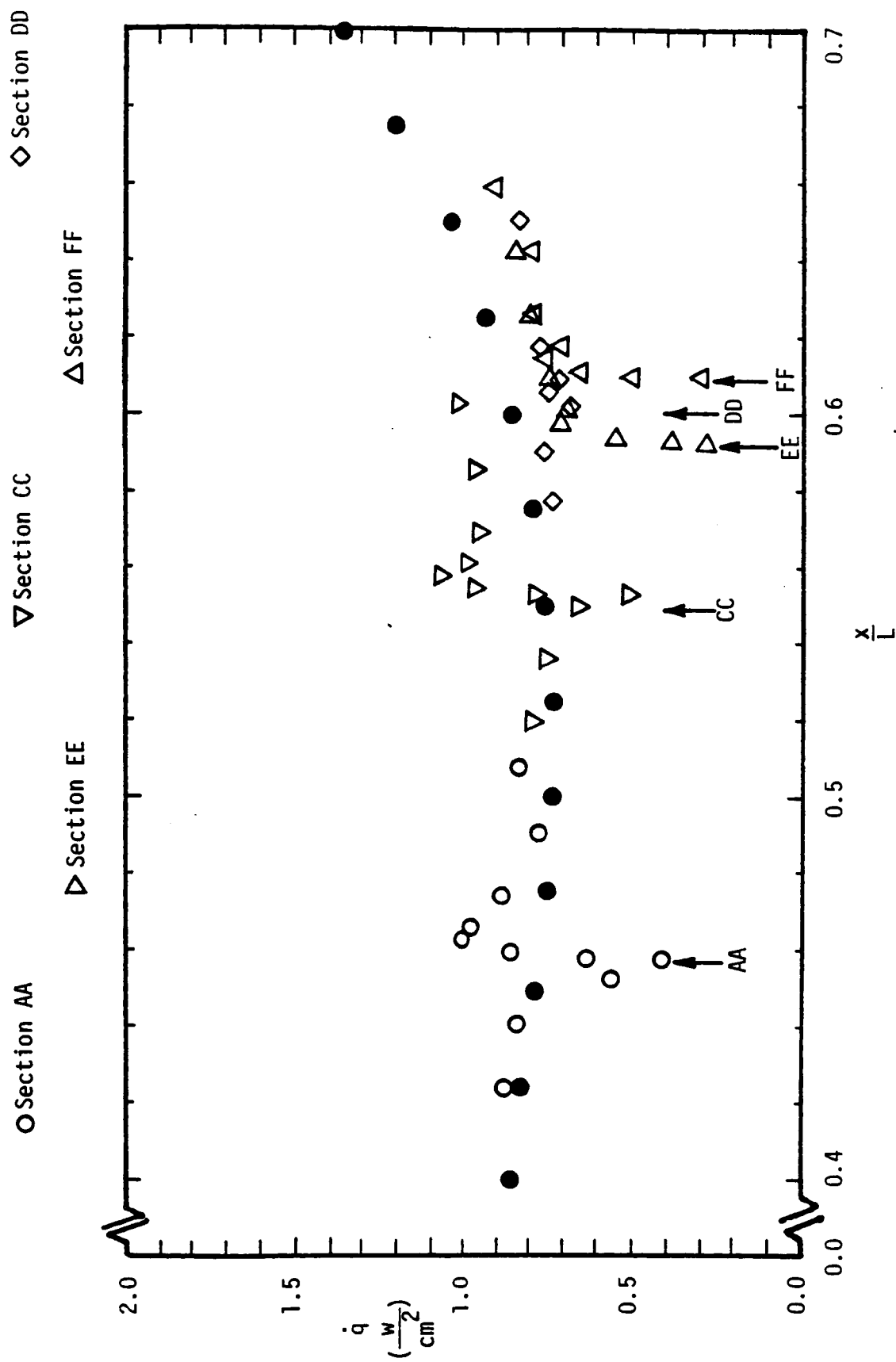
(a) Run 47

Figure 32. - The heat-transfer distribution in the vicinity of the diagonal, intersecting gaps of C5, $Re_{\infty, L} = 4.01 \times 10^6$. Filled symbols are for the flat plate (C1) at the same flow conditions (Run 39).



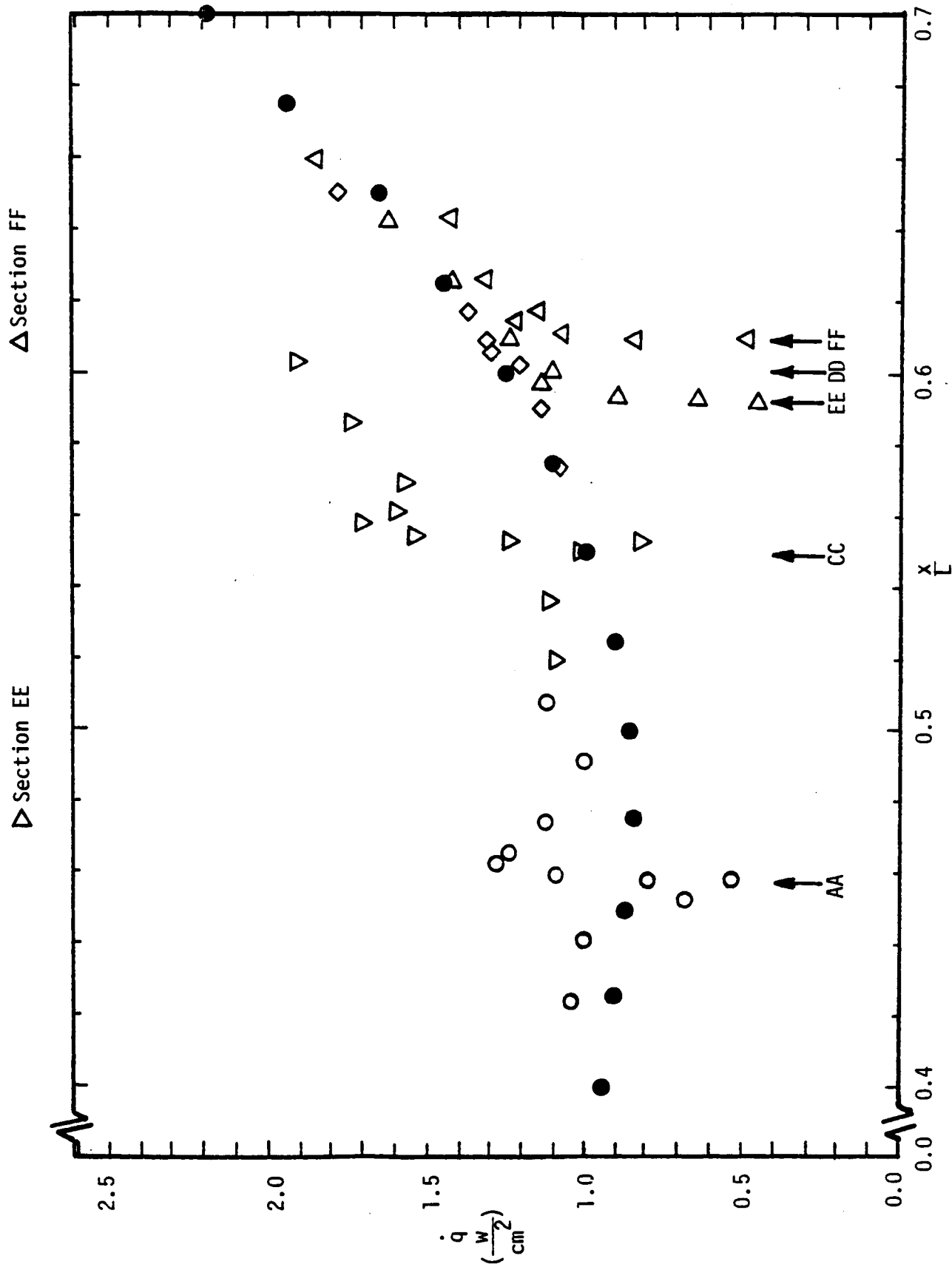
(b) Run 51

Figure 32. - Concluded.



(a) Run 48

Figure 33.- The heat-transfer distribution in the vicinity of the diagonal, intersecting gaps of C5, $Re_{\infty, L} = 5.90 \times 10^6$. Filled symbols are for the flat plate (C1) at the same flow conditions Run (40).



(a) Run 49

Figure 34. - The heat-transfer distribution in the vicinity of the diagonal, intersecting gaps of C5, $Re_{\infty,L} = 8.11 \times 10^6$. Filled symbols are for the flat plate (C1) at the same flow conditions (Run 41).

